1-31-2013

Impact of carbon support chemistry, morphology, and structure on platinum catalyst durability for PEMFC applications

Anant Patel

Anant J. Patel
Candidate

Chemical and Nuclear Engineering
Department

This dissertation is approved, and it is acceptable in quality and form for publication:

Approved by the Dissertation Committee:

Dr. Plamen Atanassov, Chairperson

Dr. Abhaya Datye

Dr. Kateryna Artyushkova

Dr. Rod Borup

Dr. Kunal Karan

IMPACT OF CARBON SUPPORT CHEMISTRY, MORPHOLOGY, AND STRUCTURE ON PLATINUM CATALYST DURABILITY FOR PEMCE APPLICATIONS

by

ANANT J. PATEL

B.S., Chemical Engineering, Georgia Institute of Technology, 2008

DISSERTATION

Submitted in Partial Fulfillment of the
Requirements for the Degree of

Doctor of Philosophy
Engineering

The University of New Mexico
Albuquerque, New Mexico

December 2012

Dedication

I would like to thank my family and friends for their love, support, and willingness to knock me down a peg or two when I start getting a bit egotistical. I would also like to thank the Universe for not suffering a crippling bout of self-doubt, 17th Century chemist Robert Boyle, and the long line of diseases, famines, predators, man-made and natural disasters that spared my predecessors long enough for them to procreate.

Acknowledgements

The work presented in this document was made possible by funding from the Department of Energy EERE Hydrogen and Fuel Cell Technology Program (Project DE-EE0000466).

The work presented in this document is a small part of a much greater whole, and I would like to acknowledge my collaborators at Ballard Power Systems, Inc. for their support. Over the course of the past 3 years, the advice, technical insight, and willingness to collaborate have been invaluable. I would specifically like to acknowledge Drs. Silvia Wessel, Monica Dutta, Vesna Colbow, and Mr. David Harvey for their contributions to this project.

I would also like to acknowledge the members of the Fuel Cell Team at Los Alamos National Laboratories, namely Drs. Rod Borup, Rangachary Mukundan, Dusan Sperjnak, John Davey, and Joe Fairweather. During the CCM durability testing portion of this project, they were instrumental in educating me in how to assemble, condition, test, and age the materials. Without them, it is likely that CCM testing may never have even completed.

I would like to acknowledge my adviser, Dr. Plamen Atanassov, for helping to establish the general form of my research project. Without his assistance, it would have been difficult to find a means of producing a body of work relevant to the field's current level of understanding.

Finally, I would like to acknowledge the contributions of Dr. Kateryna Artyushkova to this project. Dr. Artyushkova was the person I spoke to most about my work, and without her help, I would be hopelessly lost regarding X-ray photoelectron spectroscopy, digital image processing, and principal component analysis. Much of the

work presented in this document was done jointly with Dr. Artyushkova, and I believe she deserves a great deal of credit for its successes.

Impact of Carbon Support Chemistry, Morphology, and Structure on Platinum Catalyst Durability for PEMFC Applications

by

Anant J. Patel

B.S., Chemical Engineering, Georgia Institute of Technology, December 2008

Ph.D. Engineering, University of New Mexico, December 2012

ABSTRACT

Polymer electrolyte membrane fuel cells are a promising alternative energy source, capable of being deployed as successful replacements in many stationary and mobile applications. These devices, however, lack durability, and this has become one of the limiting factors for commercialization. Many projects have focused on finding ways to improve their lifetimes, but few have tried to examine the underlying causes behind their corrosion. The goal of this project was to identify which parameters have a significant impact, both positive and negative, on PEMFC durability. To do this, three series of samples were analyzed using microscopic, spectroscopic, and electrochemical methods. Electron microscope images provided information on the sample morphology and structural composition. Scanning electron microscopy provided information on the samples surface morphology, including roughness and porosity; transmission electron microscopy was used to determine the thickness and continuity of graphite sheet in the samples, and scanning transmission electron microscopy provided information on particle size distribution. Spectroscopic techniques interrogated the surface and bulk of the samples to provide information on their chemical composition. X-ray photoelectron

spectroscopy was used to analyze the surface chemistry of the samples, while electron energy loss spectroscopy was used to quantify the relative graphite content in the bulk. The electrochemical methods used determined how the samples reacted to differing operating conditions, and were used to accelerate the aging process. Rotating disk electrodes were employed to study the catalytic performance of the samples in an ideal setting, while membrane electrode assemblies gauged how well the samples performed in a more realistic application. By comparing the structural and chemical composition throughout a sample's lifetime, correlations relating performance changes to changes in its physical structure were identified. Multivariate analysis provided a means of comparing highly different data sets, and identifying similar patterns between them. Based on the data, we have found that higher surface area cathode catalysts suffer greater performance losses over their lifetime due in large part to changes in their porosity. Higher surface area carbons are also characterized by discontinuous graphite structures, making them more susceptible to oxidation than lower surface area carbon supports. It was also found that samples with higher microporosity (nanometers) were more stable than samples with high mesoporosity (5-20μm), but that porosity increases due to the aging process. The total graphite content was also found to be less important that the surface graphite content. It was determined that the speciation of platinum in the samples had an effect on the durability, and samples with high PtO and Pt-C content at the beginning of life were more stable than those with mostly Pt metal. Furthermore, it was found that samples that experienced the largest losses in performance were associated with the largest increase in Pt metal speciation, and PtO and Pt-C content was reduced overall. Finally, it was determined that it is difficult to directly compare results for

durability testing performed using a rotating disk electrode to those obtained using a membrane electrode assembly. In order to increase the predictive capability of RDE experiments, future work will need to investigate altering many of the experimental conditions, such as the electrolyte and ionomer content.

Table of Contents

Table of Figures

List of Tables

1. Introduction

As the population and economies of developing nations continue to grow, so will the level of demand put on already stressed conventional energy sources, such as coal and petroleum. Increased consumption of coal and petroleum is coupled with an increase pollution in the form of CO_2, exacerbating the problems of global warming and climate change. Because of these facts, there has been a growing push towards reduction in energy consumption across the globe coupled with a desire to develop and deploy cleaner renewable energy resources. Many of these green energies, such as solar, wind, or hydroelectric, are seen as well established in the public view point, but they are currently limited to stationary power generation applications, and are often geographically restricted. For automotive applications, high power density devices are required for acceptable performance, which has led to the development and introduction of battery and fuel cell powered vehicles. Fuel cells, like batteries, are devices which convert energy stored in the form of chemical bonds into electrical currents by separating redox coupled reactions. Unlike batteries, which are considered "closed" because they self-contained, fuel cells are "open" systems, meaning fuel and exhaust flow into and out of the cell during operation. Because fuel cells do not burn fuel, they are capable of achieving higher efficiencies than internal combustion engines as less energy is lost as waste heat. Fuel cells are also characterized by low environmental impact and easily scalable designs.[1-3] Though several types of fuel cells exist, the work described in this and subsequent chapters will focus on proton exchange membrane fuel cells (PEMFC).

1.1 Proton Exchange Membrane Fuel Cell Basics

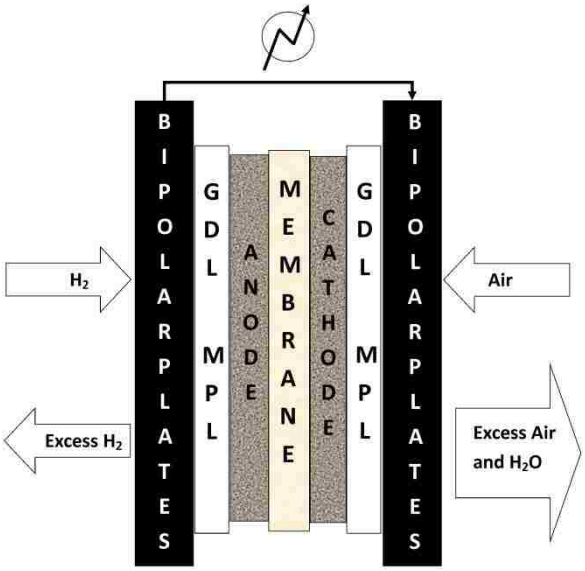

Figure 1. Simplified schematic of a typical PEMFC consisting of 5 major components: the bipolar plates, the gas diffusion layer and microporous layer collectively known as the gas diffusion media, the anode, the cathode, and a selectively permeable membrane.

Figure 1, above, shows a simplified schematic of a single PEMFC. PEMFCs operate by separating the hydrogen oxidation reaction (HOR) from the oxygen reduction reaction (ORR), equations 1.1 and 1.2 respectively.

$$H_{2,g} \rightarrow 2H^+ + 2e^- \quad (1)$$

$$4H^+ + 4e^- + O_{2,g} \rightarrow 2H_2O \quad (2)$$

As seen in Figure 1, hydrogen molecules enter the cell and interact with the anode, where they are separated into protons and electrons. The protons generated by the anode catalyst are transported through a selectively permeable membrane to the cathode portion of the fuel cell, while the electrons travel along an outside circuit where they generate the current used to do work. At the cathode, the electrons and protons are combined with oxygen molecules to form water and complete the circuit. For commercial applications,

individual cells are unlikely to supply sufficient voltage, and therefore PEMFCs are often deployed as stacks containing tens to hundreds of cells.

PEMFCs consist of several components: bipolar plates, gas diffusion and microporous layers (GDL and MPL), and the anode, cathode, and a selectively permeable membrane, collectively known as the membrane electrode assembly (MEA).[3, 4] The bipolar plates serve four primary functions, to act as the major channels for flow of fuel and product gas to and from the cell, and to act as the current collector for the cell stacks, to separate gas flows in the cell, and to act as cooling structures for stack. The GDL and MPL, known as the diffusion media (DM) serve similar functions by providing channels for fluid flow to and from the MEA, reducing liquid water content in the cell due to their hydrophobicity, and to provide structural support to the MEA. Finally, the MEA is the power source of the cell, with HOR occurring at the anode and ORR at the cathode. Theoretically, HOR takes place at 0.0V compared to a reversible hydrogen electrode (RHE), and ORR occurs at 1.23V vs. RHE, meaning that cells should have an open circuit voltage (OCV) of 1.23V. Though this is the theoretical limit, a modern PEMFC is more likely to achieve an OCV of roughly 0.95-0.97V when fully conditioned. The open circuit voltage is the equilibrium potential for a reaction; deviations from this value are called overvoltages, and are due to kinetic losses. Kinetic losses are generally associated with activation energies or energy barriers for reactions, in this case ORR.[5] HOR has a theoretical reversible potential of 0V irrespective of temperature. In the presence of platinum nanoparticles, HOR is assumed to occur rapidly, and at potentials close to the theoretical potential. Because of this, a PEMFC anode is often used as the cell reference

electrode as well. ORR is much more sluggish, and many of the inefficiencies associated with PEMFCs are the result of comparatively poor ORR kinetics.[5-7]

1.2 PEMFC Concerns

Since the 1970s, the Department of Energy has been a major driving force behind much of the PEMFC research conducted in the United States by providing funding and setting targets for lifespan, power density, and cost for varying applications. Through the Office of Energy Efficiency and Renewable Energy (EERE), funded projects are tasked with producing a portable fuel cell system with a power density of 900Wh/L by 2015, and a direct hydrogen fuel cell for automotive applications with a lifetime of 5000 hours by 2017. In addition to expanding PEMFC lifetime, targets have been set to reduce the overall cost of the system. PEMFCs were historically manufactured using high cost materials using platinized platinum, or platinum blacks, as both the anode and cathode. Cells using these materials are still considered the benchmark for overall performance and system stability, but deploying platinum black cells is impossible due to the cost and rarity of platinum and platinum group metals (PGM).[1, 3, 8, 9] Reducing platinum content has become one of the primary goals of current PEMFC research, and these projects can be categorized in two general groups: finding and developing non-PGM catalysts as replacements for platinum, or reducing platinum by dispersing it as a nanoparticle on support materials.[10-12] Non-PGM catalysts potentially offer a major reduction in overall cost, as the platinum catalysts used in a cell stack would account for roughly half of the total cost. These catalysts, however, are often plagued by other issues, such as slow reaction kinetics or low reaction selectivity, and often catalyze the less efficient reduction of oxygen to hydrogen peroxide

$$2H^+ + 2e^- + O_{2,g} \rightarrow H_2O_2 \quad (3)$$

Formation of hydrogen peroxide occurs at 0.695V vs. RHE, well within the range of standard PEMFC operating potentials[13]. Additionally, hydrogen peroxide is a highly active oxidizing agent and is known to rapidly corrode fuel cell components, making its formation reaction very undesirable.

Conversely, the second group, while still using platinum as the primary catalyst, focuses on the using the metal as efficiently as possible. By reducing the platinum from a bulk form to nanoparticles, more of the platinum atoms are exposed at the surface instead of being inaccessible inside the structure.[14, 15] Nanoparticles, however, cannot be used independently as they are unstable in the fuel cell environment (see chapter 1.2.2), making a support material necessary. Because the change in design was instigated as a cost reduction mechanism, the support material would need to be inexpensive and relatively stable in the fuel cell environment. Carbon blacks were shown to fill the role of support material well, as they can have near metallic electrical conductivity, high surface areas, and are considered stable in the fuel cell environment.[16-18] As a result, carbon supported platinum nanoparticles are considered the state-of-the-art PEMFC electrode catalysts, and have been widely adopted for commercial applications. Though these catalysts are currently the most promising for commercial applications, there are still legitimate concerns regarding their viability for widespread use.[8, 9, 18-22]

1.2.1 Durability Issues

As a group, PEMFCs using carbon supported platinum nanoparticles lack the robustness necessary to be viable as commercial alternatives to existing power generating devices. There has been a growing interest in moving toward alternative materials as the support, such as molybdenum oxides or nitrides, but these materials suffer multiple drawbacks, such as cost, conductivity, and surface area, and are currently unfit for widespread use.[23, 24] As a result, carbon has maintained its position as the primary support material for PEMFC applications, and has become the focus of durability testing across the globe.[8, 9, 17-19, 25-34]

Understanding PEMFC degradation has become a high priority research topic in the electrochemical field. It has been well established that several contributors affect the lifetime of a cell, including transient operation, catalyst poisoning and interrupted operation, but understanding the specific processes is equally important. By investigating the various mechanisms, methods to mitigate or eliminate them can be developed. The primary objective is to increase the lifespan of PEMFCs, but the targeted lifespan of these devices makes conventional testing impractical. As a result, accelerated stress tests (ASTs) have become the standard for PEMFC aging protocols.[25, 35] Using ASTs researchers are capable of aging the cells at a more rapid rate than they would typically experience in standard operation. How well ASTs correlate to specific time scales is still a matter of debate, but they have provided profound insight into events that cause drastic cell degradation. A typical fuel can still experience performance losses greater than 50% over their lifetime.[8, 21, 22] These losses have been attributed to changes to the platinum nanoparticles, to the catalyst support material, or a combination of both.[5, 15, 36]

1.2.2 Catalyst Degradation

In general, platinum nanoparticles used in PEMFCs are on the order of 2-5nm in diameter.[1, 5, 34, 37, 38] At such small diameters the surface area-to-volume ratio for the nanoparticles is extremely high, meaning that fuel cells can be made with less platinum overall without suffering a reduction in the electrochemical active surface area (ECSA). Conversely, the surface area is easily lost by changes to the catalyst morphology, greatly affecting the observed activity.[5]

There are several recognized mechanisms for platinum surface area to be lost in PEMFCs: Ostwald ripening, nanoparticle coalescence, detachment, and dissolution and precipitation in the proton exchange membrane. A visual representation of these mechanisms can be seen in Figure 2, below.

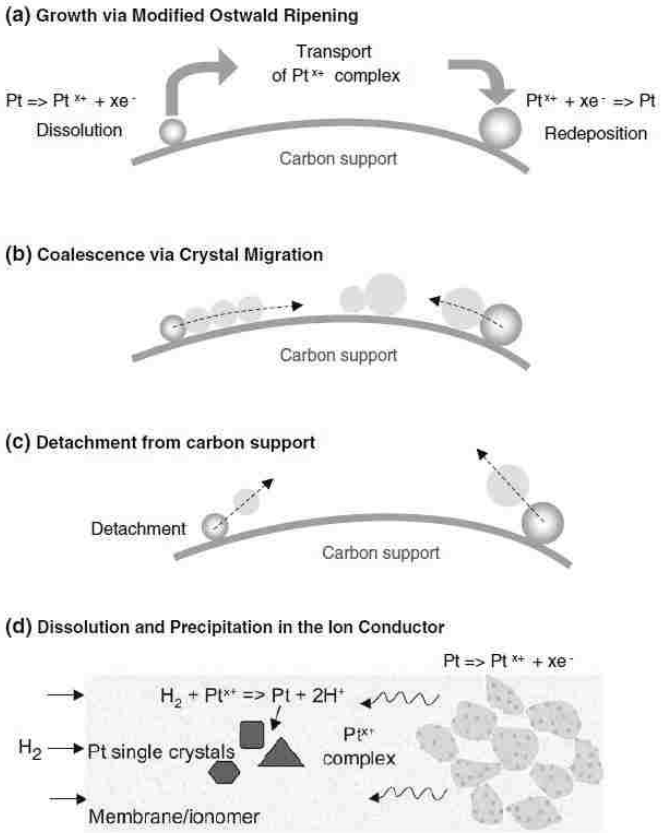

Figure 2. Illustrative difference between (a) Ostwald ripening, (b) sintering coalescence, nanoparticle detachment, and dissolution and precipitation in the membrane layer.[37]

As stated earlier, the nanometer diameter particles are a more efficient use of the precious metal because more of it is available for catalysis. However, nanoparticles in this size range also have high surface energies making them thermodynamically unstable.[39, 40] Because of this, the system will move toward a less energetic state, and this is will lead to a loss of catalytic surface area.[14, 27, 41, 42] Platinum dissolution is the mechanism which facilitates Ostwald ripening and precipitation in the membrane. According to Darling and Meyers, platinum dissolution is controlled by three chemical reactions:

$$Pt \rightarrow Pt^{2+} + 2e^{-} \quad (4)$$

$$Pt + H_2O \rightarrow PtO + 2H^{+} + 2e^{-} \quad (5)$$

$$PtO + 2H^{+} \rightarrow Pt^{2+} + H_2O \quad (6)$$

Equation 5 is the most thermodynamically favorable, but equation 4 is the kinetically favored reaction. They argue that at potentials relevant to PEMFC operation (above 0.6V vs. RHE) the system will be slow to establish an equilibrium between PtO and Pt^{2+} due to the differences in kinetic and thermodynamic stability. Though dissolution would affect all of the nanoparticles, the smaller nanoparticles have been shown to dissolve more quickly than the larger nanoparticles in the fuel cell.[43] The dissolved platinum ions would have greater mobility than nanoparticles, making diffusion through the cell possible, where they could redeposit on to existing nanoparticles, via Ostwald ripening. Conversely, instead of depositing back onto the electrode surface, Pt^{2+} ions could migrate through membrane, where they would be reduced by hydrogen crossover from the anode of the cell creating a platinum rich layer between the membrane and cathode.[15, 18, 34]

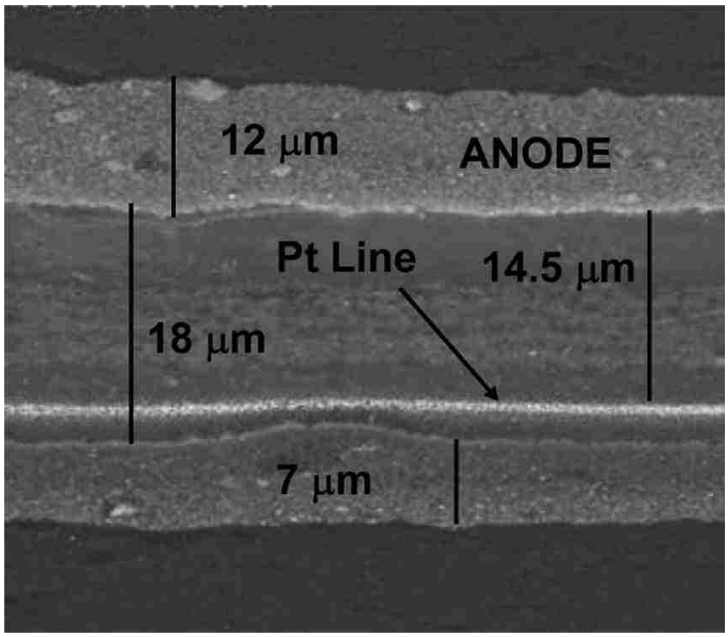

Figure 3. SEM micrograph of a MEA after 2000 hours of testing at 80°C, 100%RH, and 150kPA; platinum is clearly visible inside the membrane layer separating the electrodes.[34]

PEMFCs tested under these conditions do exhibit a significant amount of platinum in the membrane layer, indicating Pt migration throughout the cell is possible, and in cases of fuel starvation, platinum cations will travel from the cathode to the anode before redepositing. Figure 3, taken from the work done by Young et al., clearly shows how the cathode catalyst layer thins over time, as well as the complete removal of the cathode carbon sub-layer.[18] In addition to lowering the performance of the cell, the embedded platinum promoted small perforations in the membrane, known as pinholes, which allow hydrogen to travel to the cathode side of the cell.[34, 44]

Finally, platinum nanoparticle detachment occurs through corrosion of the carbonaceous support material. As will be discussed in section 1.2.3, carbon is susceptible to oxidation in the PEMFC environment. Over time, if the support material degrades enough, platinum nanoparticles can detach, and will lose electrical and catalytic contact with the remainder of the cell. In addition, multiple methods have been used to

deposit platinum nanoparticles onto carbon support materials; if the nanoparticles are poorly attached initially, many of them can be forced out of the system. Also, should the nanoparticles have insufficient contact with the ionomer in the cell, these particles will be detached from the cell due to a lack of conductivity of protons and electrons.

Figure 4. Platinum prices per ounce over the last 10-yr period (image courtesy of Monex.com)

Though ECSA loss is detrimental to PEMFC performance, using larger nanoparticles (>5nm in diameter) while reducing the number of nanoparticles less than 2nm can slow the rate of surface area loss.[37] This approach, however, is discouraged because of the cost required to manufacture a fuel cell stack containing hundreds of individual cells. As Figure 4 shows, the price of platinum has more than tripled over the last 10 years, and is likely to continue to increase for the foreseeable future. Should a fuel cell stack be manufactured using more platinum, the cost of the catalyst would be passed on to the consumer, and become economically untenable. Because of this, the Department of Energy has set standards for reduced platinum loadings in PEMFCs, with the goal of achieving 0.125mg Pt/cm^2 by 2017. Though using smaller nanoparticles would enable manufacturers to achieve these desired loadings, researchers have also

turned to designing platinum alloys as potential catalysts.[45, 46] Strasser et al. have shown that addition of a second or third metal can improve the stability of the catalyst without significantly reducing the activity.[11, 47] The general hypothesis behind this has been attributed to two different factors: physical structure of the catalysts and relative stabilities of the alloyed metals. Researchers have done a significant amount of work in order to design and produce specific compositions and structures of the alloyed materials. Currently many are testing catalysts composed of a non-precious metal core with a platinum shell.

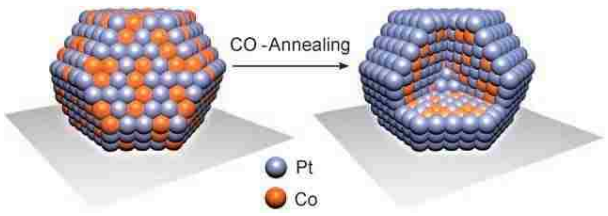

Figure 5. Illustration of a typical designed Pt-alloy catalyst[48]

Some of the catalysts with this structure are produced by sputtering of platinum on to non-PGM nanoparticles, though several groups make use of the differing properties of the metals. One approach, exploited by Mayrhofer, et al., begins by producing a solid solution of platinum and cobalt, and exposing the catalysts to carbon monoxide.[48] Pt-Co complexes are more favorable than Co-Cu, and when a potential is applied to the nanoparticles, the platinum will preferentially segregate toward the surface while cobalt moves toward to the center.

Catalysts with this type of design typically show comparable performance to pure platinum nanoparticles, but they do not exhibit the same durability issues.[11, 39, 40, 47]The argument most groups make to explain this is the difference in particle sizes. The primary

reasoning behind producing smaller diameter nanoparticles is that more of the platinum will be available for catalysis, which is especially important at reduced loadings. The designed nanoparticles, however, will have platinum almost exclusively on the surface, meaning very little will be inaccessible in the bulk.[48] This also allows the alloyed nanoparticles to be significantly larger than the pure nanoparticles without increasing the overall platinum loading. The larger alloyed particles are more stable in the device, and typically do not exhibit the same surface area loss associated with pure platinum. These alloyed materials, however, are still very expensive to produce, and are currently synthesized in small batches. Finding solutions to these problems will greatly improve the prospects for commercial PEMFC applications.

1.2.3 Carbon Support Corrosion

Corrosion of the carbonaceous support materials has a strong influence on PEMFC performance as they provide anchoring sites for the catalyst, and are responsible for ensuring electrical conductivity between the nanoparticles and the diffusion media. The supports, like the diffusion media, are also highly hydrophobic, helping prevent flooding conditions in the cells. Most supports are highly structured carbon blacks, materials with large surface areas and irregular geometries which prevent them from stacking neatly. Carbon blacks are also easily and cheaply produced, making them effective catalyst support materials; however, carbon is thermodynamically unstable in the PEMFC environment, and will oxidize through the following reaction:

$$C + 2H_2O \rightarrow CO_2 + 4H^+ + 4e^- \quad (7)$$

This reaction, known as the carbon oxidation reaction (COR) has a theoretical reversible potential of 0.207V (vs. RHE) meaning that it could occur at standard PEMFC operating

conditions (0.67V, 80^{o}C).[18, 49] Though kinetically unfavorable compared to HOR and ORR, the reaction will still occur during normal operation, and can become competitive during fuel starvation or cell flooding.[19] Degradation of the catalyst support material affects both the performance and the lifetime of fuel cell. Low levels of corrosion have been shown to reduce electrode thickness, limiting fuel flow, while oxidation of the support can decrease the materials hydrophobicity, potentially leading to cell flooding. Finally, corrosion of the carbon supports can cause platinum surface area loss through islanding or nanoparticle migration.

As stated, carbon blacks are highly structured materials, and can be broken down into smaller subsections: primary carbon particles, aggregates and agglomerates. A primary carbon particle is the smallest individual unit for a carbon black and is roughly 20-50nm in diameter, aggregates are conjoined groups of particles and reach sizes of hundreds of nanometers, and agglomerates are connected aggregates, generally on the order of tens-to-hundreds of micrometers. These structures are composed of essentially two types of carbon, graphitic and amorphous, and are differentiated by the degree of crystallinity. Overall, though amorphous carbon will have short-range order, the bulk of the material is not considered to have a crystal structure, while graphitic carbon does. This crystallinity of graphitic carbon has been shown to have a significant stabilizing effect on the material, making it less susceptible to oxidation, as seen in Figure 6 below.

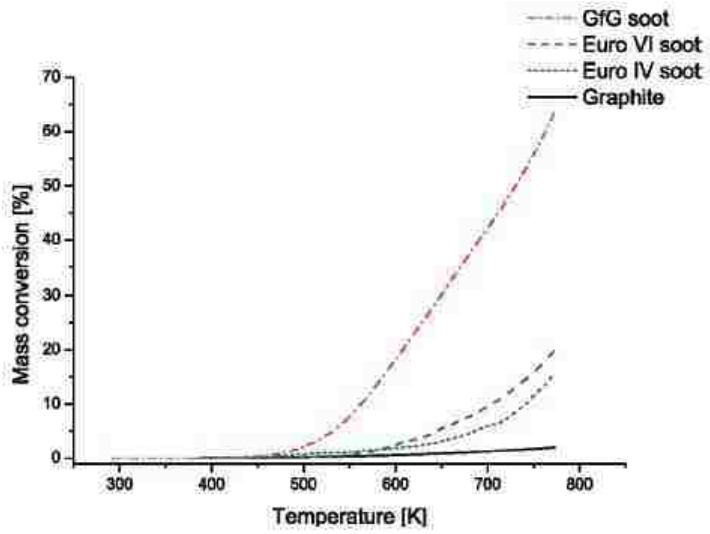

Figure 6. Mass conversion versus temperature of 4 carbon samples obtained using thermogravimetric analysis. Graphite showed very little loss while highly amorphous carbons showed significant loss of mass.[26]

Using thermogravimetric analysis Knauer et al showed that highly ordered pyrolytic graphite (HOPG) lost 2% of its mass to oxidation while an amorphous sample lost 65%. This has important implications for carbon supports because it has also been shown that samples containing more graphitic carbon show reduced rates of corrosion. Corrosion rates, however, are not explicitly defined by graphite content; because carbon blacks are composed of both amorphous and graphitic carbon, how the particle is organized would also have a significant effect.

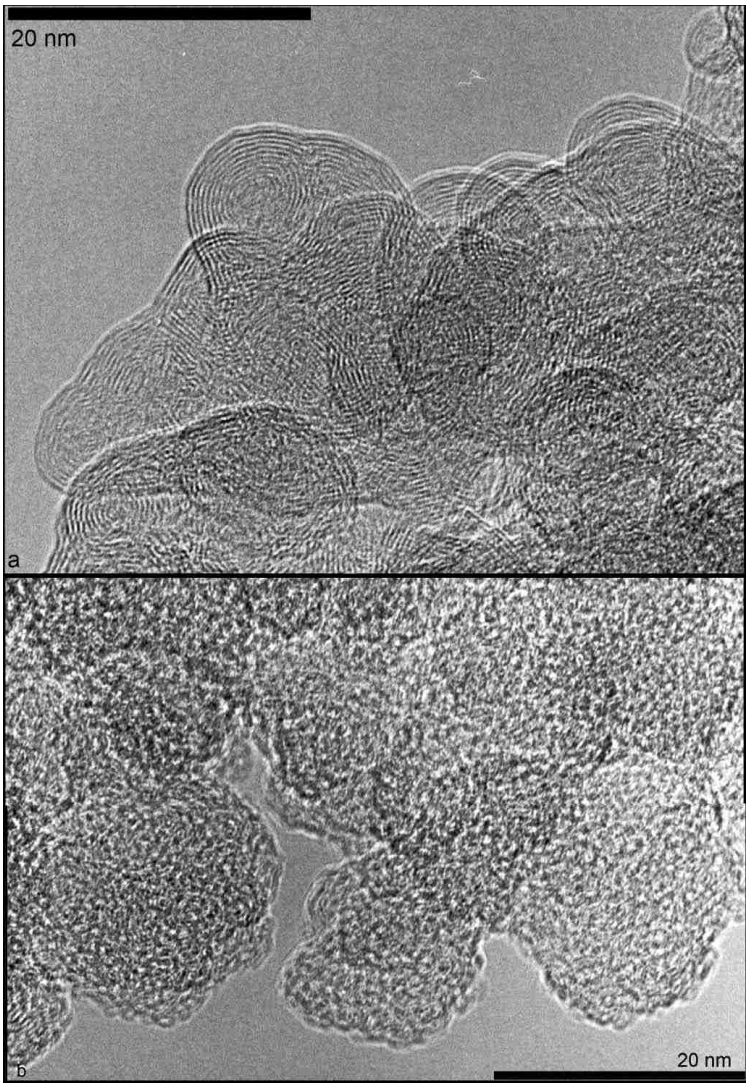

Figure 7. The internal structures of carbon blacks produced in different enviroments; above, 10% H2 and 90% Argon, below 100% H2. The top exhibits more long-range order, while the bottom has short-range graphene sheets. Taken from Jäger et al.[50]

As seen in Figure 7, the surface of carbon particles can be dominated by amorphous or graphitic carbon, or it could be a mixture of both. Because they lack the stabilizing crystal structure, amorphous carbon would exhibit a higher corrosion rate, especially in the presence of platinum, a known COR catalyst.[26] If Pt nanoparticles are largely being supported by amorphous carbon, COR will become competitive with the HOR, and over time, the Pt nanoparticle will completely oxidize the amorphous carbon supporting it, resulting in islanding, an unsupported nanoparticle. These nanoparticles

will lose electrical contact with the remainder of the support, and will either exit the system through the effluent stream, or migrate toward the cathode side of the cell. Conversely, a sample with a graphite shell and amorphous core would likely exhibit a far lower corrosion rate, while a sample with a mixed amorphous-graphite phase would be somewhere between the two.

The spaces between the structures provide pathways for water and gas diffusion throughout the electrode, enabling the PEMFC to run efficiently. When the carbon blacks corrode, the aggregate structure breaks down. As a result, the macropore volume of the electrode layer (30-60μm diameter) begins to decrease, while the micropore volume increases.[30] Because of the shrinking macropore volume diffusion through the electrode becomes restricted, lowering the overall rate of reaction.[3] As the corrosion of the cell continues the electrode layer will thin and compress, slowing diffusion processes throughout the cell.[18] These effects are often restricted to the cathode, and if the carbon support has large amorphous content, diffusion can be restricted with as little as an 8% loss in carbon mass.

As stated previously, though carbon oxidation will occur during normal operation, the oxidation rate will be quite low. In comparison, start-up/shutdown or fuel starvation events have a much more significant impact on support stability, and can both lead to cell failure. Though they share some characteristics, these events are very different.[8, 25, 29]

All stacks will have start-up/shutdown events, but they are more common for automotive use because of the nature of the application. Unlike stationary fuel cell stacks, which are always on and carry a constant power load, automotive cells will be used intermittently and have to supply a variable levels of power based on the vehicle's

demand. Because of this, automotive fuel cells experience a higher level of support corrosion than stationary devices. It has been shown in several studies that start-up/shutdown events subject PEMFCs to potentials as high as 1.5V for brief periods of time.[25] What causes the potential spike is still being debated, but the most accepted hypothesis is that it is the result of a hydrogen/air front on the anode side of the cell.[8] Between uses, air can be present on both the anode and cathode side of the cell, but while running, hydrogen is present on the anode side. As a result, when the cell is started or shut down, there is a short period of time in which both air and hydrogen will be present on the anode side.

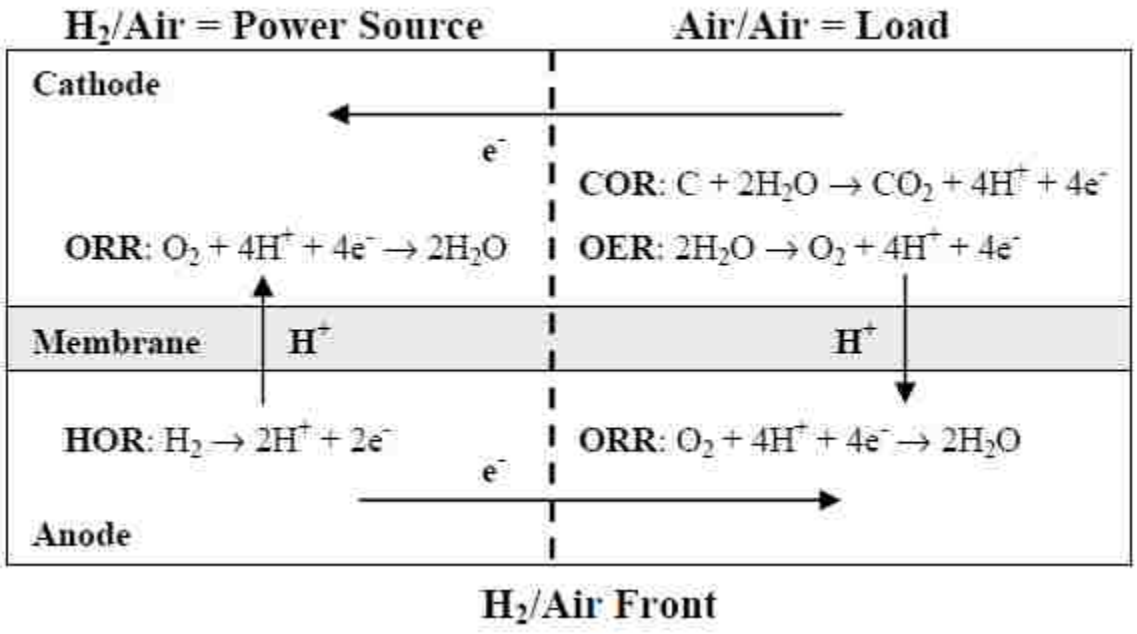

Figure 8. Proposed mechanism for carbon support oxidation during start-up shutdown events[8]

In the presence of platinum, hydrogen will be oxidized to protons and electrons as defined by HOR. Because the cell is just starting or shutting off, power is not being drawn from it. As such, electrons produced by oxidizing hydrogen move across anode to reduce oxygen instead of following the outside circuit. Not all the protons will move

down the anode, and some will cross over to the cathode side. This leaves a deficiency of electrons for the reduced oxygen, but this is compensated by splitting water and evolving oxygen. As stated previously COR is catalyzed by Pt, but in this case C is oxidized by water not O_2. This releases 4 protons and 4 electrons, a requirement to balance the anode reactions. In the end, electrons travel along the cathode, and combine with the protons from the anode and the oxygen to form water. Next, by assuming the charge in the cell must be conserved, Yu et al. were able to write the following equations:

$$i_{HOR} = i_{ORR-H2/Air} \tag{8}$$

$$i_{ORR-Air/Air} = i_{COR} + i_{OER} \tag{9}$$

$$i_{HOR} = i_{ORR-Air/Air} \tag{10}$$

where i is the current density, and subscripts the various reactions occurring in the cell. When the equations are solved for i_{COR}, we are left with:

$$i_{COR} = i_{ORR-H2/Air} - i_{OER} \tag{11}$$

$i_{ORR-H2/Air}$ is the driving force behind the reaction, indicating that the current derived from COR will be dependent on the current from OER. As a result, it has been theorized that embedding oxygen evolving catalysts into PEMFCs could be a means of mitigating carbon corrosion. These catalysts, however, would create a short in the cell by providing protons and electrons to the cathode side of the cell without capturing them for usable work. Instead, Yu et al. showed that different chemical compositions of the carbon supports affect the rate of corrosion. By graphitizing a 50cm^2 MEA, a 5 fold decrease in the corrosion rate versus an unaltered MEA.[8] Other groups have shown similar results, though performance data from these same experiments is generally derived from inferred methods rather than direct measurement. Because these events have been shown to contribute heavily to cell corrosion, mimicking these conditions has become common

practice for testing new carbon supports and catalysts. Sample MEAs or catalysts inks are subjected to recurrent potentiostatic pulses of 1.5V or higher in order to understand how they would react to start/stop conditions.

Like start/stop events, fuel starvation can have significant implications for the carbon support structure.[3, 19, 25, 38, 51] Again, these events begin on the anode side of the cell, but are caused by the absence of hydrogen instead of a mixed gas front. Fuel starvation varies by degrees; in some instances it is restricted to segments of a single cell while in others it can affect portions of an entire cell stack.[3] For short periods of time the effects are similar to start/stop events: accelerated support corrosion and reduced power production. Extended periods of starvation, however, could lead to cell reversal which can lead to a rapid failure for the entire cell stack.

Unlike start/stop events, fuel starvation can occur for multiple reasons; these include insufficient fuel flow, poor stack design, or obstructions in the cell. Insufficient fuel flow is the simplest cause, and is generally characterized by low flow at the cell outlet or at the last cells in a stack where the fuel is more likely to have been consumed. Some flow channel designs exacerbate this problem, but these issues are generally identified by post-mortem analysis or computer modeling of the cell.[25] Obstructions, such as condensed water or corroded flow channels, can also impede fuel flow.[52] Fuel cells and stacks are designed to minimize the presence of liquid water, and operate at elevated temperatures (80-120^{o}C) in order to prevent condensation. Because the membrane must be hydrated in order to conduct protons, fuel cells currently operate with humidified feeds, but as water is the product of the PEMFC reaction, running at high current densities can lead to excess water being retained in the cell. As a result, fuel cells are

being tested to operate using gas feeds with varying degrees of relative humidities, with targets for less than 20%RH at 120^{o}C by 2017. By lowering the relative humidity of the gases fed to the cell, cell flooding can be prevented, but maintaining proton conductivity through the membrane remains a challenge.[53]

Cell flooding can impede fuel flow; instead of passing through pores as gas, hydrogen must pass through a condensed water phase before reaching the catalysts. Under normal conditions, water will not condense in the system because of the reduced humidity, elevated temperature, and hydrophobic carbon supports.[38, 51, 54] Over time, however, the carbon supports oxidize, becoming increasingly hydrophilic, and allowing water to condense. In most instances, this process will occur on the cathode portion of the cell due to the inherently higher humidity caused by the reaction, while anode flooding is restricted to highly humidified fuel flow. In either case, flooding results in a three-phase interface: gaseous fuel, water, and the platinum catalysts. This in turn reduces the mobility of the fuel, and can lead to starvation conditions.[55, 56]

Fuel starvation can affect both sides of a cell, but only hydrogen starvation has an effect on the cell's condition.[51] Hydrogen starvation cuts off the cell's proton and electron supply requiring the cell to find an alternative source. As a result, the COR reaction will become the favored reaction on the anode side as it provides a source for both.[38, 51] This process is similar to start-up/shutdown, but they differ in time scales. Because start/stop events last less than a second, experiments have shown that most cells take several hundred to fail completely. Depending on how the cell is operated, failure could occur quickly or after long periods of extended use. In comparison, hydrogen starved cells are

running while the carbonaceous supports are being oxidized. As such, failure from starvation occurs in less than a minute, and is largely undetectable as it is occurring.

1.2.4 Ionomer and Membrane Concerns

Though was not a component that was investigated in this work, understanding issues with the ionomer layer is important.[3] The ionomer and membrane materials used in PEMFCs are generally fluorinated polysulphonic acid polymers. These polymers are selectively permeable, and transport protons preferentially over other chemical species, but as mentioned in Section 1.2.3, these materials need to be well hydrated in order to conduct protons. Because of this, the ionomer content in the catalyst layers can affect the layers' hydrophobicity, potentially making them hydrophilic. Understanding how the ionomer content in the catalyst layers affects performance and durability is unknown, but it is likely significant.[3, 44, 57, 58]

2. Research Problem

As stated previously, preventing or reducing PEMFC corrosion has become one of the primary areas of research for the field, and this has led to significant advancements in many areas over the last 20 years. Currently many factors are known to affect the lifetime of a cell: platinum nanoparticle size and loading, graphite content and operating conditions as discussed in Chapter 1. By identifying these factors, fuel cell researchers and manufacturers have been able to produce more stable and powerful systems, but it is unlikely that these parameters are solely responsible for the tested performance and lifespan, making further testing highly important.

Fuel cell testing, in general, can be divided into the following groupings: component versus device testing, and performance versus durability testing. Component testing looks at how individual parts of a fuel cell perform under set conditions, while device testing investigates a cell or stack as a whole. Performance testing focuses on improving how well components or devices work at the beginning of their life, while durability testing monitors how components or devices change over their lifetime. These categories are not completely independent, and can be visually represented as a biplot, as shown in Figure 9, below.

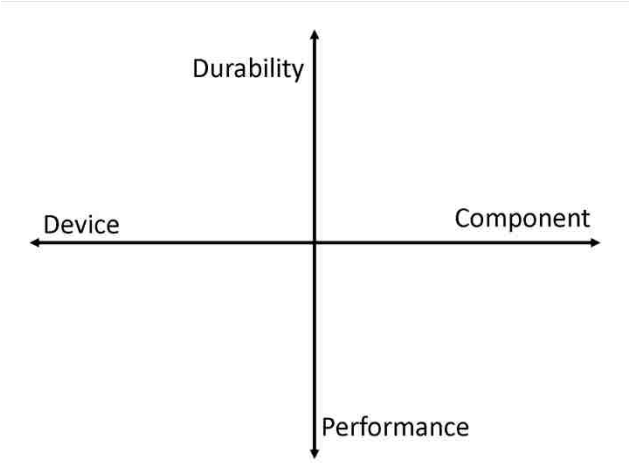

Figure 9. Visual representation of how the field of fuel cell testing can be broken down based on the types of experiments conducted.

In general, component testing is less expensive and can be done more rapidly and is used as a screening method to exclude materials from being tested in fuel cells devices. While useful, results from component testing have not been proven to be directly comparable to those obtained from a fuel cell as the experiments themselves are very different. A prime example of this is using accelerated stress test (AST) protocols while testing a catalyst using a rotating disk electrode (RDE). RDE experiments are used as a way to quantify ORR performance at the beginning of life (BOL) for PEMFC catalysts, as they have been established as a rapid and relatively inexpensive way of determining a catalyst's activity. Durability tests, however, generally focus on quantifying performance losses and physical or chemical changes that occur in fuel cell setup. While establishing a RDE experiment protocol is relatively simple and easily searchable in the literature, finding the optimal operating conditions for a fuel cell is an iterative process, and is dependent on numerous factors, including the flow channel design, total active area, or the level of compression on the cell to prevent hydrogen cross-over or leakage. Fuel cell testing also requires a larger investment in both materials and equipment than RDEs,

raising the cost per experiment. Because they are comparatively inexpensive, research groups are performing stress testing using RDEs as means of estimating losses over cells lifetime, and many have reported minimal changes to the open circuit potential or limiting current. [59-61]The issue, however, is that it is unclear as to how reliable results obtained from durability studies using a RDE actually are as have been no published articles comparing the results to those obtained from a fuel cell.

Fuel cell durability testing is done using two different methods, long-term durability testing or ASTs. Long-term durability tests can be described as monitoring a fuel cell or fuel cell stack at standard operating conditions for several hundreds or thousands of hours. ASTs, however, subject fuel cells to atypical conditions and promote the degradation of the constituent components and have been instrumental in finding new factors which inhibit or promote degradation. Conversely, though they are short by comparison, AST protocols generally last days or weeks, which still presents an issue when investigating larger sample sets. Like long-term durability tests, ASTs are better suited for investigating corrosion processes or for validating cell or cell stack designs than screening out inferior materials.

The other predominant issue with published results from this field has to do with the lack of characterization data for catalysts and support materials. As many of the projects are funded by companies actively developing commercial PEMFCs, much of the data that is acquired regarding the catalyst or support materials physical or chemical properties are not published in order to prevent competitors from mimicking them. While this is beneficial to the individual, it means that there is little published data that can be used to correlate sample characteristics to its behavior as an individual component or as

part of a fuel cell. It is highly likely there are factors in addition to particle size distribution, ECSA, and graphite content which affect how a catalyst perform at the beginning of life and throughout its lifetime.

Overall, there is a need to change how the durability of fuel cell catalysts and support materials are tested. Existing methods, while informative, can be time consuming or overly expensive and are prohibitive for testing large sample sets. Additionally, much of the work has focused on the chemical composition of the carbon support, but it has not investigated differences between how the carbon supports are organized, i.e. do differences in between bulk and surface composition of carbon supports matter, and if so by how much? As a whole, there is little published work in the literature focusing on how to predict a catalysts lifetime based upon early characterization and experimental results, making durability testing of promising catalysts necessary.

3. Objectives

The primary objective for this project was to develop predictive capabilities for the behavior of carbon-supported platinum nanoparticles after extended use in PEMFC applications based on preliminary characterization techniques and experimental results. Current techniques are costly and time consuming, making it logical to find a viable alternative solution. By building a database filled with information detailing the chemical, morphological, and structural characteristics along with performance data for a large Pt/C sample set, it should be possible to predict the how an outside sample would behave based on preliminary results, essentially connecting initial component performance statistics to device durability.

As stated previously, it has already been determined that highly graphitic carbon supports are oxidized by the PEMFC environment more slowly than less graphitic samples, thus displaying smaller performance losses over their lifetime. It is unlikely, however, that graphite content alone controls the corrosion rate, and that other factors are involved, namely sample chemistry, morphology (physical factors on the carbon particle or aggregate scale), and structure (physical factors on the agglomerate to bulk scale). Secondly, while monitoring how these factors affect the lifetime of a cell is important, understanding what impact they have on the initial performance is equally important, with the general idea being that the initial characteristics of a sample are directly correlated to the performance after prolonged use. In order to determine what affects degradation processes positively and negatively, a large set of carbon supported platinum nanoparticles were investigated in order to determine how they changed chemically, morphologically, and structurally from the beginning to end of life. These changes were

correlated to performance losses to determine what factors were associated with high and low corrosion rates, and which were found to have little impact overall. These correlations were found by using a mixture of established characterization and experimental techniques and non-traditional approaches, namely digital image processing (DIP) and principal component analysis (PCA). While it was not the main objective, validating DIP and PCA as data analysis tools was necessary in order to validate the methodology described in this work.

The other objective of this project was to determine if RDEs are suitable to run durability testing protocols. Because RDE setups are less expensive and require less material in order to conduct an experiment, they are attractive for testing how novel catalyst designs behave over long periods of time. However, because no published work connecting RDE durability testing results to those obtained by using a fuel cell exists, the accuracy of the data remains questionable. By performing similar experiments using both a RDE and a fuel cell, it was possible to determine if RDE experiments are a reasonable means of predicting long term performance losses without running an additional fuel cell.

In order to achieve these objectives, the project was divided into three sections: investigation of carbon support materials and catalysts at the beginning of life, performing pre- and post-mortem analysis on tested fuel cells, and actively corroding catalysts using RDEs and fuel cells in order to compare differences and similarities between the two processes. The underlying idea is to use long-term testing as a means of comparing fewer catalysts which will likely perform well instead of multiple catalyst of unknown quality. By comparing the results obtained through each section, it is possible to draw connections relating specific characteristics to identifiable behavior, thus making

preliminary or BOL examinations of a catalyst material a viable method for predicting device lifetime.

4. Research Methods

Because this project was focused on building a model capable of predicting a catalyst's lifetime based on preliminary results, multiple techniques were used to acquire the data necessary to build a robust data set. The data gathered from these techniques, however, were heterogeneous, making it necessary to use multivariate analysis in order to identify trends between them, and this can be seen visually in Figure 10, below.

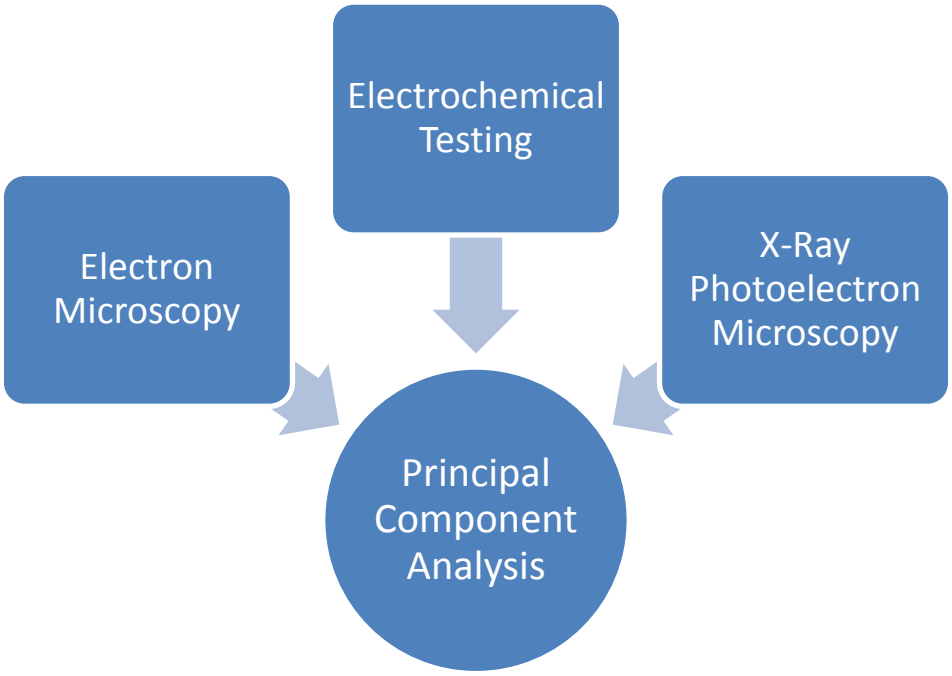

Figure 10. Visual description of data sets acquired during the project. Because of the diversity in the types of data, principal component analysis was required to identify trends in the data.

The goal of this project was to identify chemical and morphological parameters that have a significant impact on either the performance or corrosion resistance of the cell. This project investigated undecorated carbon supports and Pt-C catalysts. Each catalyst or carbon black was subjected to a variety of electrochemical and characterization techniques in order to fully characterize it. The catalysts were tested using electrochemical experiments and various characterization techniques in order to find previously undetected trends and relationships between a wide assortment of variables.

4.1 Carbon Supports and Catalysts

The carbon support materials and catalysts that were tested during this project are identified by their relative surface areas and the loading of platinum, designated as a weight percent. There were 5 carbon black supports: low surface area carbon (LSAC), mid-range surface area carbon (MSAC), high surface area carbon 1 (HSAC1), high surface area carbon 2 (HSAC2), and Vulcan XC72R (Vulcan). There were two sets of catalysts: one with constant 50wt%Pt loading on each carbon black, identified as Pt50XXXX, and the other with variable platinum loading on LSAC, identified as PtXXLSAC. In addition, there were two heat-treated forms of the high surface area catalysts, Pt50HSAC1-HT and Pt50HSAC2-HT. Though beginning of life performance and characterization data were acquired for all the samples, the electrochemical data acquired for this project primarily focused on the 50wt% Pt-C catalysts. The type of proton exchange membrane used for these experiments was Nafion® NR-211.

These catalysts were not produced at UNM; this project was part of an international collaboration with multiple partners looking to improve PEMFC design. The carbon blacks and catalysts were produced by an unidentified third-party, and details regarding the synthesis, decorating, and initial heat-treating processes are unknown. Additionally the manufacturer of the gas diffusion layer, and the method of producing the catalyst coated membranes were not disclosed to UNM.

4.2 Electrochemical Testing

In order to be commercially viable, PEMFCs must employ catalysts that maintain high levels of activity over prolonged periods of time, generally in the tens of thousands of hours. An active, but quickly degrading, catalyst would lead to frequent replacement,

while an inactive but stable one would require large loadings. Because of this, quantifying how the performance of each catalyst changes over time is the single most important data set in this project. Though it sounds simple, quantifying performance loss in meaningful terms is quite difficult. We focused on changes to open circuit voltages and limiting current densities for RDEs and changes to the polarization curve for the membrane studies. Electrochemical impedance spectroscopy (EIS) measurements were performed at Ballard Power Systems, Inc. in order to monitor changes to the cells resistivity and capacitance. For the RDE experiments, the Tafel slopes were originally tabulated because they were considered to be unambiguous, but it was quickly determined that there is no clearly defined convention on how these values are calculated. Some of the calculated Tafel slope results can be seen in Chapter 5.

4.2.1 Rotating Disk Electrode

Rotating disk electrodes were used as a means of gauging the BOL performance of the catalyst samples for ORR, and to age the catalysts for durability studies. While single cell testing is preferable, RDEs offer a means of investigating a sample's activity for a specific reaction in physically simplified system. Unlike a fuel cell, where individual components play a role in the delivered currents or voltages, RDEs allow researchers to examine one component separately, in this case the cathode electrode catalyst. Many of the performance losses seen in PEMFC behavior can be attributed to the cathode portion of the cell, meaning testing the cathode catalyst independently gives researchers a general idea of how they would perform in a fuel cell. Because of this, rotating disk electrodes are employed in order to filter out inactive catalysts. Compared to a traditional cell setup, RDEs are highly simplified and require only a small quantity (100µg or less) of an experimental sample to test, making it ideal for this type of work.

The experimental setups will be discussed in greater detail in subsequent chapters, but general information about the experiments is presented here. The surface area of the RDE used in these experiments is 0.196cm^2, and the catalysts are tested as 4mg/ml inks. The inks are pipetted on to the electrode to achieve a 0.1mg Pt/cm^2 loading for the BOL experiments and 0.4mgPt/cm^2 for the durability studies. The difference in loadings is related to differences in the experiments; conditions for the BOL experiments were optimized in order to obtain the best performance while the durability studies used identical loadings for both the RDE and fuel cell cathode. The experimental conditions used for the RDE experiments greatly affect the results with some electrolytes will improve the performance, while the positioning of the electrodes can adversely affect them. The rotation speed, however, has the most significant impact, as can be seen in Figure 11, below.

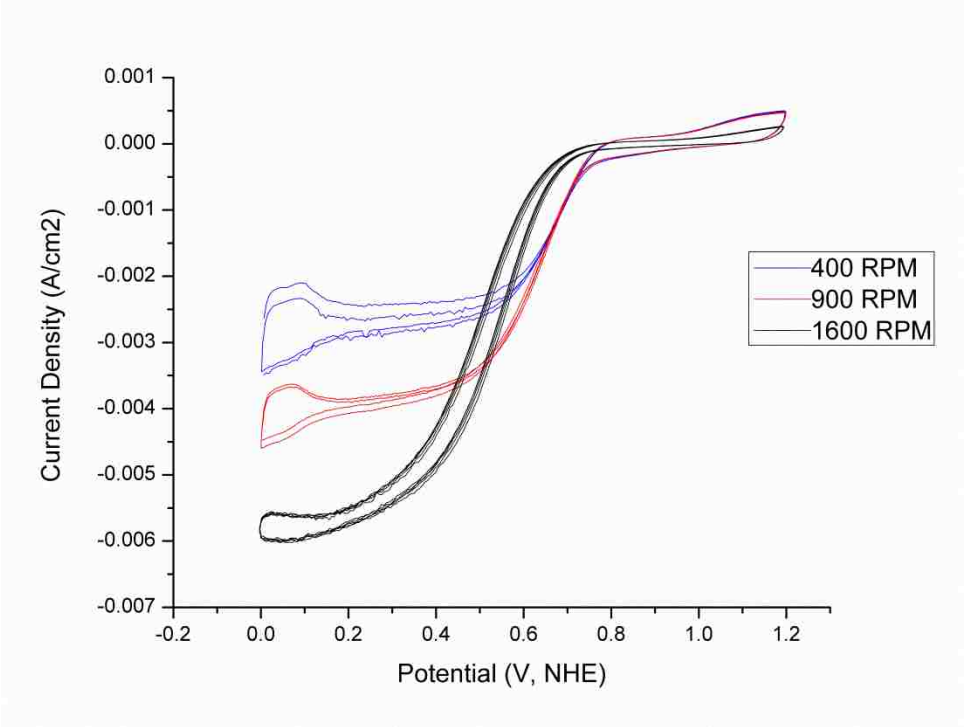

Figure 11. ORR cyclic voltammograms for Pt50LSAC at varying rotational speeds

Carbon blacks are characterized by high microporosity, and nano-scale platinum particles will often be dispersed in them. Because of tortuous path and hydrophobic nature of these supports, polar analytes have difficulty diffusing through them. For a properly functioning fuel cell, this is not a serious issue because of the reduced humidity prevents liquid water from condensing, as discussed in Chapter 2, but for a RDE in aqueous media, this could prevent the dissolved gases from reaching the nanoparticle surface. As a result, researchers often run these experiments at various rotation speeds; increasing the rotational speed of the electrode will force the analyte into the smaller channels, allowing access to the majority of the nanoparticles.

The CV of an ORR catalyst is typically "S" shaped, and is divided into three regions—kinetic, ohmic, and transport—which are named for the effects which are predominately responsible for the observed current or voltage. An example is shown in Figure 11.

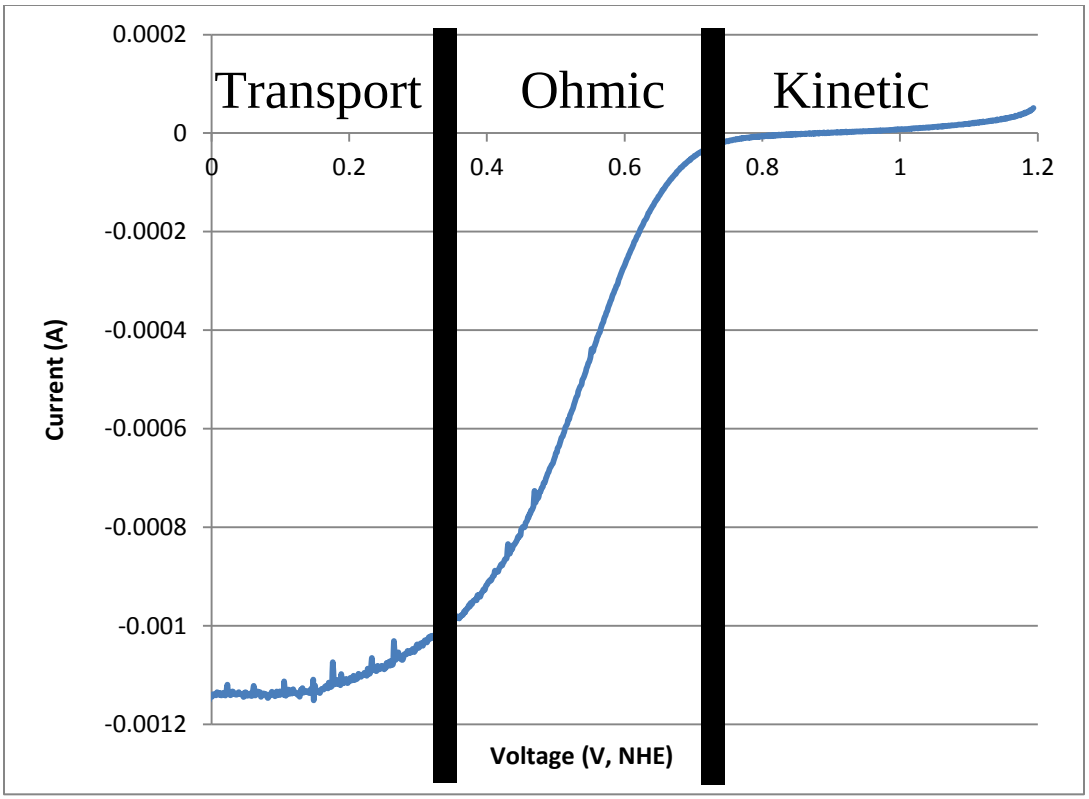

Figure 12. Capacitance corrected CV of Pt50LSAC obtained at the beginning of life. The CV is divided into three regions--kinetic, ohmic, and transport--named after the effects which dominate at those potentials.

The rates of reaction or diffusion to the electrode are what define each region. In the kinetically controlled region, the rate of reaction is very- slow meaning little current - is produced by the electrode, while the rate of diffusion is assumed to be infinitely fast by comparison. In the transport limited region, the rate of reaction far exceeds the rate of diffusion and the current plateaus to the limiting current. At the limiting current the concentration of the reactants near the electrode is effectively zero as the reactant species are consumed immediately after interacting with the electrode. Finally, in the ohmic region neither the reaction kinetics nor diffusion dominate, and the current and potential are related through an independent resistance, and the system obeys Ohm's Law. Because of this, fuel cells operate near the edge between the ohmic and mass transport regions

where they typically produce sufficient power to meet the system requirements without additional losses.

Though the shape of the BOL voltammograms are similar, differences in them can point to differences between catalysts. Figure 13, below, shows the BOL cyclic voltammograms (CV) for Pt50LSAC and Pt50MSAC for ORR.

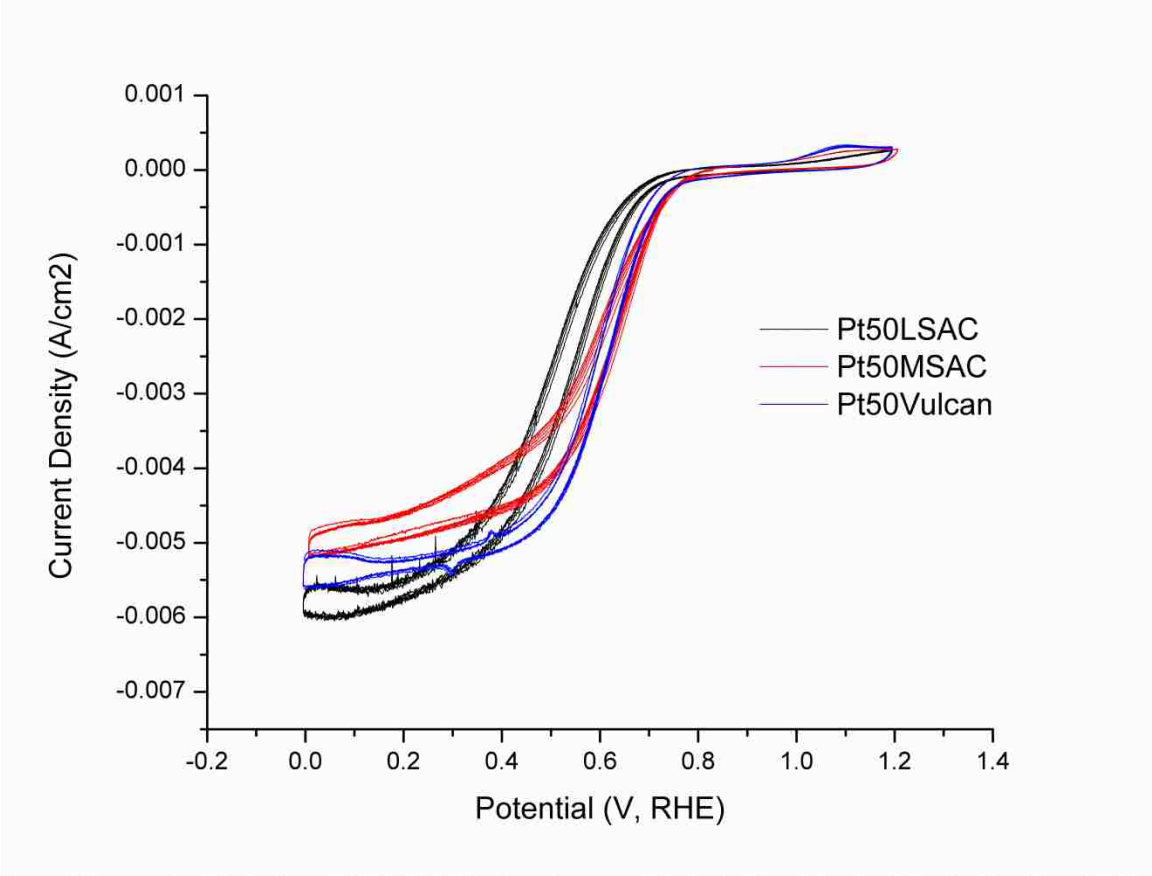

Figure 13. ORR Cyclic voltammograms for Pt50LSAC (black), Pt50MSAC (red), and Pt50Vulcan (blue) taken at the beginning of life.

The main factors that can be pulled from the voltammograms are the open circuit potential and limiting current. The open circuit potential (OCP) represents the equilibrium point between the forward and reverse reactions, in this case the reduction of oxygen or the electrolysis of water. For ideal systems, the reaction's OCP would be identical to the theoretical potential (1.23V vs. RHE for ORR), but due to energy barriers,

these values differ by tens to hundreds of millivolts. Deviations from the theoretical potential are called overpotentials, and represent unavoidable energy losses, and therefore catalysts with smaller overpotentials are preferred. The open circuit potential also partially dictates the usable voltage range for a system because operating a fuel cell at potentials greater than their open circuit would mean the system is consuming power as opposed to producing it. During the course of its lifetime, a sample's OCP will shift to greater overpotentials, consequently shifting the ohmic region and the maximum deliverable power of an electrode or cell. Because of this samples that exhibit little change in the open circuit potential can be considered more durable than those with larger shifts.

The limiting current is the maximum current obtainable by the electrode, and provides a means of comparing the influence of the carbon support on the system, as can be seen in Figure 13 where Pt50LSAC has a limiting current of -6mA/cm^2 and Pt50MSAC has a limiting current of -5.2mA/cm^2. Changes to the limiting current over the course of a testing protocol can be used as a means of comparison to the CCM tests, with both tests showing a percentage of maximum current obtained at the end of life compared to the beginning. The limiting current is also called the Levich current, and can be used to find the diffusion coefficient using the Levich equation (Equation 12), below

$$i_L = (0.620)nFAD^{\frac{2}{3}}w^{\frac{1}{2}}v^{\frac{-1}{6}}C \tag{12}$$

i_L is the Levich current, n is the number of electrons in the half reaction, F is the Faraday constant, D is the diffusion coefficient, w is the angular momentum, v is the kinematic viscosity, and C is the analyte concentration. Changes to the diffusion coefficient could

be indicative of changes in sample porosity; a reduction in the diffusion coefficient could be correlated to a restriction in porosity.

4.2.2 Small-Scale PEMFC Durability Testing

The catalyst samples from this project were aged in a single 1.1cm^2 fuel cell in order to determine how the catalysts performance changed over the course of the experiment. Unlike RDEs, which are unproven for durability studies, fuel cell testing provides an accurate means of judging how the catalysts would perform if deployed. RDE experiments differ from MEA testing in many ways, and these differences are likely to influence the performance and lifetime of a cell. Because RDEs focus solely on the catalyst material, the performance data they provide is predictive not indicative of behavior in a fuel cell. The environment the catalysts operate in can be extremely different. RDEs function by immersing the electrode surface into a liquid electrolyte and oxidize or reduce dissolved species, and are operated at temperatures between 25-40^{o}C due to the limitations of the electrodes. PEMFCs, however, are generally gas fed and are designed inhibit water condensation by operating at higher temperatures (80-120^{o}C), reduced relative humidities, and using hydrophobic materials. PEMFC testing also requires larger masses of the catalyst because of their larger surface areas in addition to the other components necessary to run a fully functioning device. Each of these components has an effect on the cell's performance, but by using identical materials, excluding the cathode catalyst, their individual influences on the results can be minimized.

For structural stability, the catalyst layers are directly deposited onto either the diffusion media to make gas diffusion electrodes (GDEs) or on to the membrane to make

catalyst coated membranes (CCMs). Though GDEs are more robust, the diffusion media can become clogged by the catalyst ink penetrating the pores in the material. CCMs are the preferred dispersion method because the catalyst loading used can be strictly controlled and large membrane surface areas (>50cm^2) can be coated uniformly at one time, and were the method used for this project.

Polarization curves were used to gauge performance losses during the cells' lifetimes. The BOL polarization curve for Pt50LSAC is shown in Figure 14. Polarization curves are similar to voltammograms in that they both show the relationship between the voltage and current over a specific window. The voltage window used for polarization curves generally covers the kinetic and ohmic regions of a voltammograms. The low voltages associated with the transport region and limiting current density are avoided during PEMFC testing in order to mitigate the risk of cell reversal.

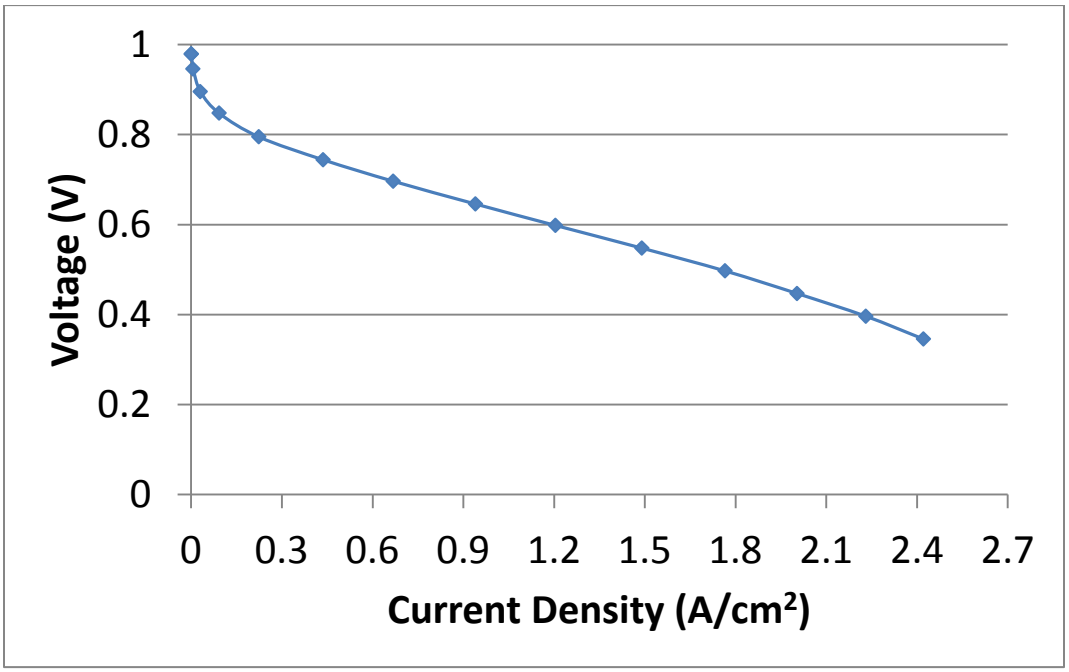

Figure 14. Polarization curved obtained at the beginning of life for Pt50LSAC using the 1.1cm^2.

The data obtained during the beginning of life experiments provide is useful, the main purpose for doing fuel cell testing was to monitor changes to the a cell's performance and characteristics over the course of the testing cycle. The Department of Energy has set targets for power densities and acceptable losses over set timespans for different commercial PEMFC uses, meaning that a cell is considered inoperable before it fails completely. Because many of the inefficiencies and degradation processes occur on the cathode, investigating how multiple cathode catalysts physically change from the beginning to end of life in a fuel cell to their performance losses, it was possible to determine what BOL characteristics lead to longer lasting, more stable PEMFCs.

Figure 15. Image of the 1.1cm2 PEMFC used for the CCM durability testing experiments in the foreground, and the FCT test stand is in the background. The PTFE gaskets and GDL are visible in the image.

Like the RDE experiments, the materials used for the fuel cell tests were provided by Ballard Power Systems, though the original manufacturer is unknown. The anode sides of the CCMs were coated with 0.1mgPt/cm^2, and the cathode side had a loading of 0.4mgPt/cm^2. As stated in Chapter 1, the rate of HOR is much higher than ORR making it possible to use lower loadings of Pt on the anode without reducing the overall rate of reaction. The anode of a PEMFC can also be used as the reference electrode for the system because of the high stability and rapid reaction kinetics. Catalysts are dispersed on to a Nafion® NR-211 membrane. The anode and cathode gas diffusion layer materials were also provided by Ballard Power Systems, and the membrane and GDLs were compressed between 0.005" PTFE sheeting. The physical hardware of the cell was provided by Los Alamos National Laboratories, and has an active surface area of 1.1cm^2, and the assembled cell was conditioned and tested using a Fuel Cell Technologies University Model test stand, shown in Figure 15 above. This fuel cell was initially used by Los Alamos National Laboratories as a part of a neutron imaging study. The cell is considered a differential cell whose flowfield can be used to mimic the activity of much larger cells. For this project, the operating conditions and protocols were established at LANL in order to mimic results obtained at Ballard Power Systems using a larger 50cm^2 cell design. Before the durability testing could begin at UNM, these results had to be reproduced on site, as shown below.

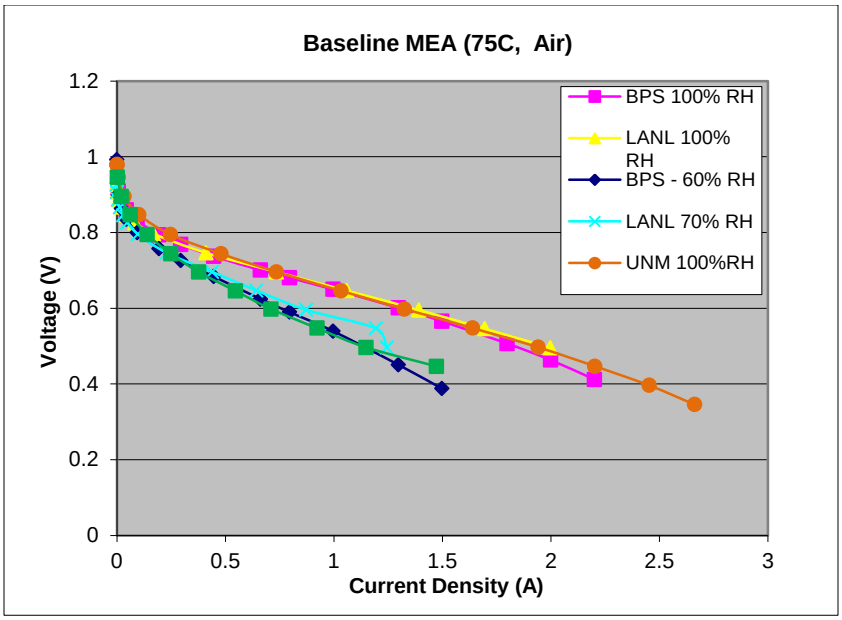

Figure 16. Comparison of baseline testing of Pt50LSAC performed at BPS (50cm^2), and LANL and UNM (1.1cm^2). The results were obtained to show that despite using a much smaller active area, functionally identical polarization data could be collected.

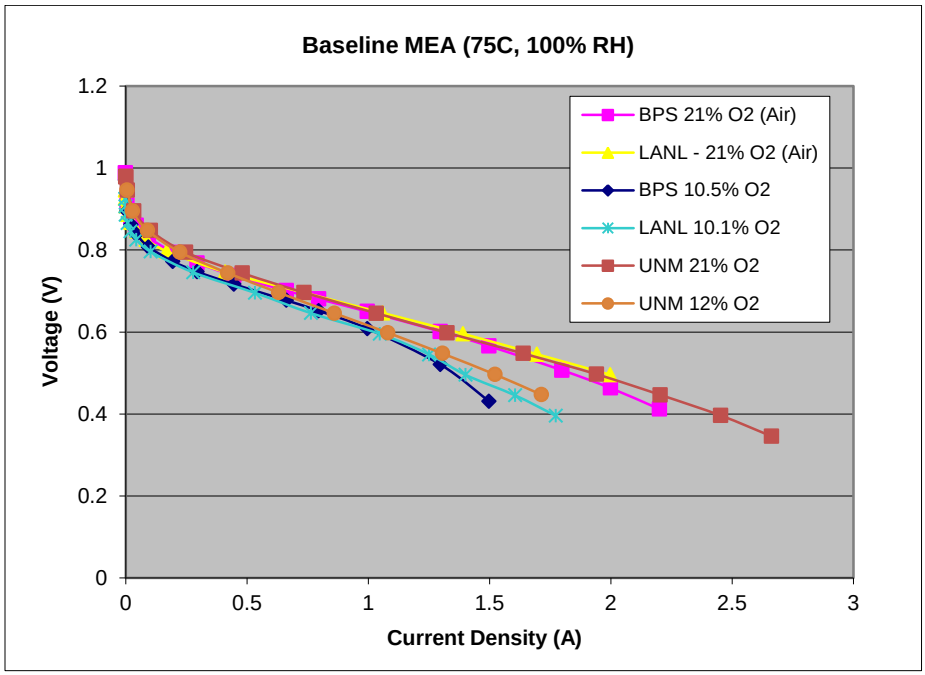

Figure 17. Secondary confirmation of the results obtained at BPS, LANL, and UNM for the 1.1cm2 cell. Small differences in the curves exist, but the variance falls within expected error.

The data shown in Figures 16 and 17 were obtained independently at each institution, and show that the beginning of life results are functionally identical for the

$50cm^2$ and the $1.1cm^2$ used in the project. Based on these results, it was decided that changes to a cell tested in the small-scale cell would correlate well with those obtained with the full-sized scale cell, and the durability testing was started.

The durability testing is done using an accelerated stress test (AST) protocol of cycling the cell between two holding potentials--0.6V for 30s and 1.2V for 60s—and is considered the standard protocol for this project. This protocol is continued 100, 500, 750, 1500, 2000, 3000, or 4700 times. 4700 cycles was chosen as the maximum number of cycles based on time constraints; from the initial conditioning to final polarization after 4700 cycles should take roughly one week. The potentials were chosen specifically as it was believed that while corrosion occurs at 1.2V, the rate would be sufficiently slow that the system would not fail after 4700 cycles. The cell is held at 0.6V in order to remove platinum oxide from the catalyst surface, and 30 seconds was believed to be sufficient. 4700 cycles was chosen as a maximum as it would allow for a full protocol to be conducted within a week.

4.2.3 Electrochemical Impedance Spectroscopy

Impedance measures a systems opposition to the flow of alternating current, and EIS uses this property to characterize reaction kinetics and electric properties of a system.[62-66] In the simplest terms, a fuel cell is held at a constant potential while an alternating and direct current are pass through it. The alternating current works as a perturbation; by changing the frequency of the alternating current, changes to the systems impedance can be determined. Different frequencies also relate to different processes, such as the capacitance of the system or proton conduction through the membrane. EIS data presented in this work was collected and interpreted at Ballard Power Systems.

4.3 Characterization Techniques

Correlating performance losses to physical changes in the catalyst layer requires extensive sample characterization. Again because the main objective of this work is to identify additional factors that promote or inhibit catalyst degradation, having information detailing the changes that occur when going from undecorated support to a catalyst to an untested catalyst coated membrane, and finally to an aged cathode layer provides insight into what characteristics should be selectively designed for, and which should be avoided. As a result, multiple techniques were used in order to thoroughly characterize the catalyst samples.

4.3.1 Scanning Electron Microscopy (SEM)

Scanning electron microscopy (SEM) has been an important technique in sample characterization for decades. Similar to light microscopes, SEMs show the surface of a sample as is, or how it would appear if it could be seen by the eye at high magnification. Using a SEM, we are able to acquire images of the catalysts surface, in turn allowing us to interpret the sample morphology. Figure 18, below, shows representative images of Pt50MSAC and Pt50HSAC1 acquired using a SEM.

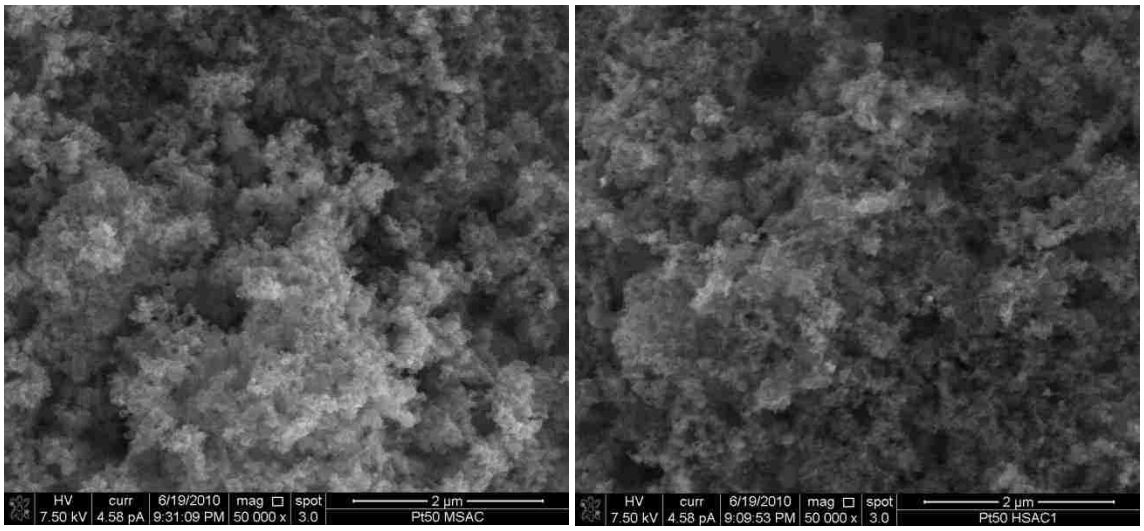

Figure 18. SEM Pt50MSAC (left) and Pt50HSAC1 (right) taken at 50,000x magnification and 7.50kV

All of the SEM images were acquired using a Hitachi S-5200 at the same magnification and voltage, in addition to keeping the contrast and brightness of the images as consistent as possible. Changes to these parameters was minimized because the images were analyzed using Digital Image Processing (DIP), a means of generating morphology statistics based on the gray-scale distribution of the sample. SEM images provide a great deal of information regarding the morphology of a sample, but discerning differences between these two images is somewhat difficult. DIP, which will be discussed in more detail in Section 4.4, requires near identical image resolution and gray-scale values in order generate useful statistics about the samples. Using DIP, statistics describing the morphological characteristics such as sample roughness, porosity, and homogeneity can be derived with a sufficient number of images. In order to generate a robust data set, multiple images were acquired per sample, and using DIP, data on the morphology of the catalyst powders and membranes were acquired.

4.3.2 Transmission Electron Microscopy (TEM)

Like SEM, TEM uses a highly focused electron beam in order to investigate sample morphology, but these techniques differ in how the electrons are detected. The key difference between the two techniques is that SEM will analyze electrons ejected from the sample through elastic scattering, TEMs use detectors that generate micrographs based on electrons that pass through a sample instead. Where SEM micrographs show the surface of the sample, TEM shows the structural components instead.

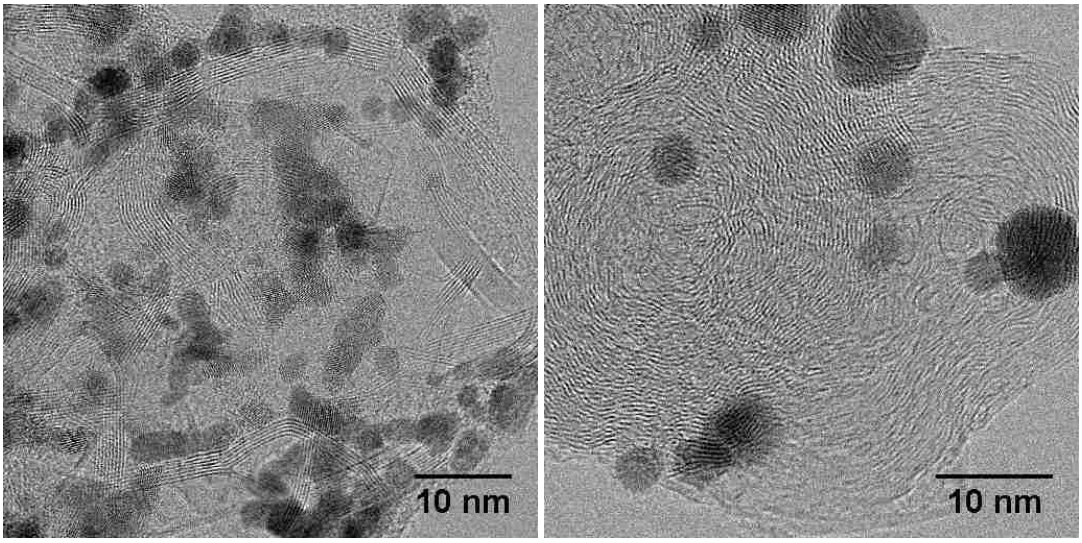

Figure 19. TEM micrographs of Pt50LSAC and Pt50HSAC1-HT taken at 2.5M magnification.

Figure 19 shows TEM images of two different catalysts. The contrast in the image is generated by either thickness or relative atomic number, where thinner, lighter portions are lighter than thicker, heavier elements. Using bright field micrographs, we are able to discern the overall structure of the carbon support, such as graphitic versus amorphous composition and the general shape of the carbon particles. As seen in Figure 19, each of the samples has differing physical structures which likely affect their corrosion resistance and performance. Pt50LSAC, for example, is composed of agglomerated particles, each with a well-defined graphitic shell. Conversely, Pt50HSAC1-HT shows no clear

demarcation between amorphous and graphitic content as both appear to be dispersed evenly throughout the sample, but is characterized by much larger Pt nanoparticles than Pt50LSAC. Bright field micrographs, however, are unable to detect the smallest nanoparticles, including mono-dispersed Pt atoms. In order to determine the particle size distribution, dark field images were needed.

Because the contrast for bright field images is based on partially on thickness as well as atomic number, small particles will be roughly the same color as the support, and essentially be invisible. Dark field detectors on scanning transmission electron microscopes (STEM) operate by capturing only electrons that have been scattered by the sample. As a result, contrast in dark field is largely a function of atomic number; denser elements will scatter more electrons than lighter ones. This in turn minimizes the effect thickness has on the image, and allows for imaging of smaller particles. Using dark field detectors, individual atoms and crystal planes are clearly visible at high magnifications. Figure 20 shows dark field images for two catalyst samples, Pt50LSAC and Pt50MSAC. The figure shows that many of the nanoparticles appear to overlap or are partially outside the frame. These obscured particles were excluded from the particle size distributions in order not to skew the results toward larger particle sizes.

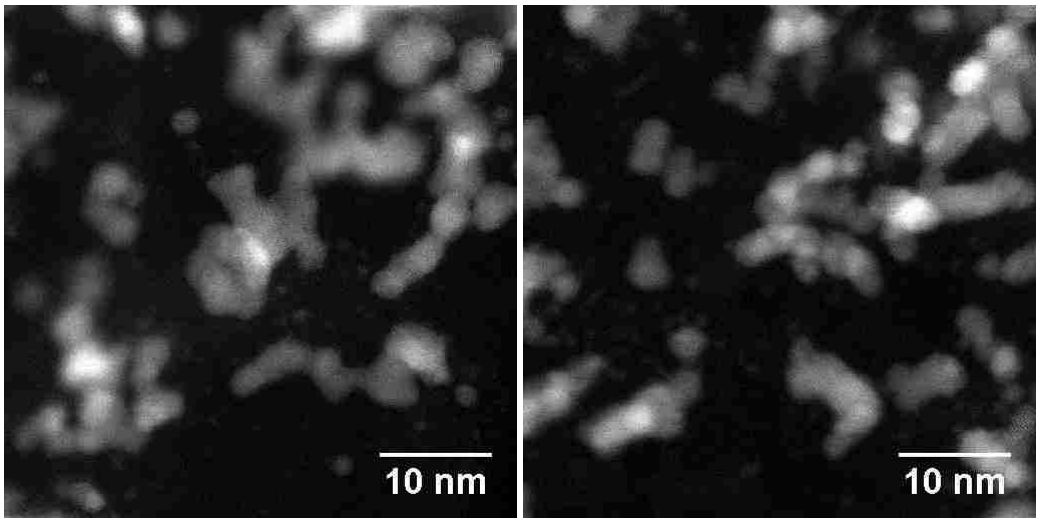

Figure 20. Dark field STEM images of Pt50LSAC and Pt50MSAC taken at 3Mx magnification.

4.3.3 Electron Energy Loss Spectroscopy (EELS)

From the higher energy in the EELS spectrum, excitations arising from transitions of inner-shell electrons to unoccupied states above the Fermi level can be obtained. For carbon, K-edge spectrum represents the transition from the 1s core level to the unoccupied anti-bonding state in the 2p energy level, σ* and π*. Direct measure of σ* and π* states of carbonaceous materials allows accurate measurement of sp^2 and sp^3 states provided a suitable reference material with 100% sp^2-hybridization. For both unknown and reference materials, HRELLS K-edge spectra can be used to calculate respective integrated areas under each of energy loss peak at K-edge, from which the sp^2 fraction can be calculated:

[redacted] (13)

where A – sample, and R- 100% sp^2 bonded reference material, the subscripts π* and (σ*+ π*) represent integrated areas under each energy loss peak at K edge determined by curve fitting procedure as described below. [26, 32]

HOPG was used as a standard for 100% sp^2 hybridized reference material. The spectra were curve fitted with three Gaussian curves to determine areas under the peaks used for quantifying the ratio of sp^2 to sp^3 bonds. Figure 21 shows EELS spectra for HOPG and LSAC sample with three peaks used for curve fitting. The π^* feature is present at energy loss of ~285eV which represents transition of C 1s electrons to unoccupied π^* state, while the σ^* feature at 291eV reflects transition to unoccupied σ^* state. The π^* feature is typical for a sp^2-hybridized carbon. The % of sp^2-bonded carbon then can be calculated using Equation 13.

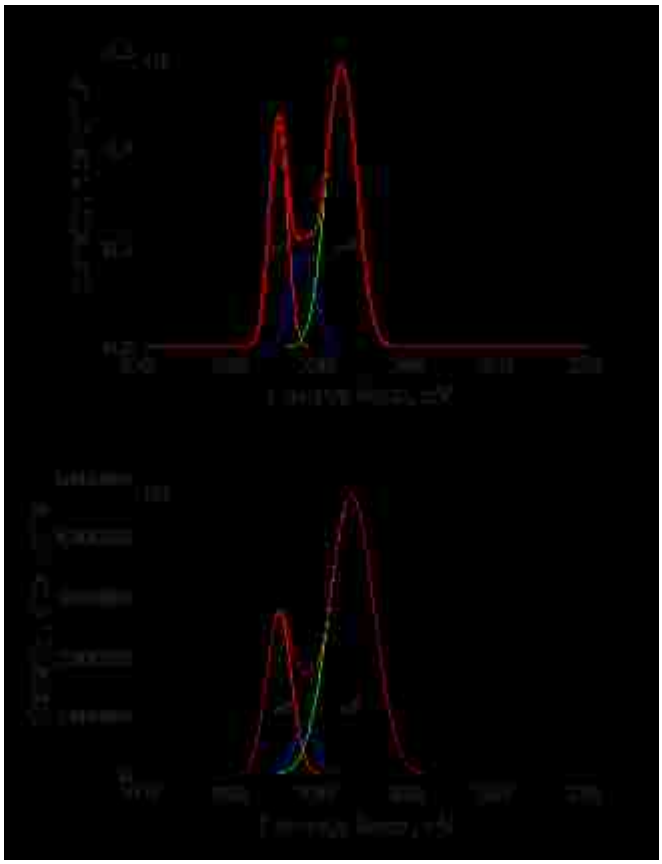

Figure 21.EELS spectra for a) HPOG and b) Pt50LSAC catalyst shown with curve fits used to deconvolute σ^*+ π^* contributions

It is important to note that this method does not specify where the graphite is located in the support material, but simply how much of the sample is graphite. Examining samples after aging allowed us to accurately pinpoint changes in the type of carbon-carbon bonding in the bulk phase.

4.3.4 X-ray Photoelectron Spectroscopy (XPS)

X-ray photoelectron spectroscopy (XPS) is a technique in which x-rays of a known energy bombard the surface of a sample, ejecting electrons. The electrons are then directed to a detector where their kinetic energies are measured. The kinetic energies of the ejected electrons are inversely related to the energy of the bond it was ejected from, and this data can then be used to characterize a sample's composition.

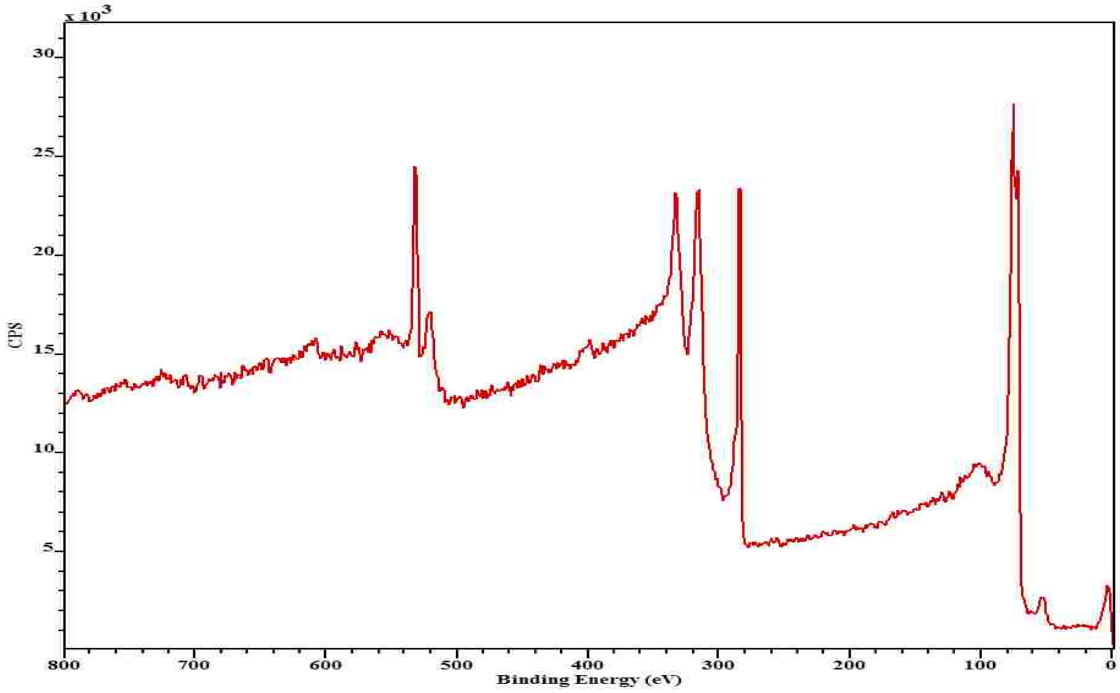

Figure 22. The XPS spectra of Pt50Vulcan as an undispersed black powder. Carbon shows a peak at 285.4eV while Pt 4f electrons appear at 70eV, though other Pt electron peaks are also visible at 330eV.

As shown in Figure 22, above, some bond energies contain large peaks; each peak correlates to a specific electron orbital such as carbon's 1s or platinum's 4f orbital. These

large peaks can be further deconvoluted in to smaller ones, each representing a specific type of bond, such as sp^2 hybridized carbon-carbon bonds or platinum-oxygen bonds.

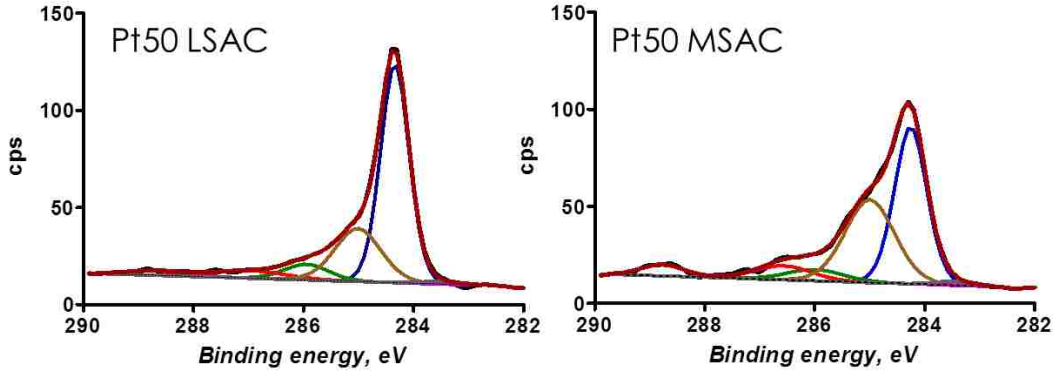

Figure 23. Deconvolutions of high resolution carbon 1s peaks for Pt50LSAC and Pt50MSAC obtained using XPS.

The spectra obtained from XPS were used to identify what elements are present in a sample along with the types of bonds present. In a sense XPS is similar to EELS, but the two differ in that XPS is a surface technique; where EELS penetrates throughout a sample, electrons excited by XPS will only be ejected from the sample if they are within a few nanometers of the surface. Any electrons deeper than that lose too much energy to escape, and are reintegrated. The maximum sampling depth for XPS is 10nm for soft materials; hard materials, like Pt, the sampling depth is only a 2-3nm. For this project, XPS analysis can be considered semi-bulk—the platinum nanoparticles are roughly the length of the sampling depth at the beginning of life, and electrons from the carbon support can be ejected from carbon particle bulk. Figure 23 shows differences between the spectra for Pt50LSAC and Pt50MSAC. From the figure it clearly visible that the samples have different surface chemistries, with Pt50LSAC having more graphite content (284.4eV) while Pt50MSAC has more aliphatic carbon (285.4eV).

For the samples used in this study, XPS provided data on changes to surface chemistry. Though the carbon oxidation reaction proceeds slowly in the presence of hydrogen, over time the supports become more oxidized by the chemical environment. Additionally, platinum-carbides and platinum oxides are also form, each potentially affecting the performance and corrosion resistance of the system. Apart from graphite and surface oxides, it has not been well established if certain chemical species promote or inhibit catalyst corrosion, but by comparing these results the performance data obtained through MEA testing, correlations can be found relating certain species to enhanced stability.

4.4 Data Analysis Techniques

The techniques described in Sections 4.2 and 4.3 are well established methods used by many research groups to investigate materials for use in PEMFCs. The data acquired using these techniques were instrumental in furthering our understanding of the corrosion process, but two additional techniques were needed to complete the study: digital image processing and principal component analysis. Digital image processing was used to generate statistics regarding the morphology of the samples based on the acquired SEM images. Principal component analysis was used to find trends between variables throughout the entire data set.

4.4.1 Digital Image Processing

Digital image processing is a method of using algorithms to extract information from an image. For this project, the processing method used individual pixels' colors and locations to derive information about sample morphology from SEM images.

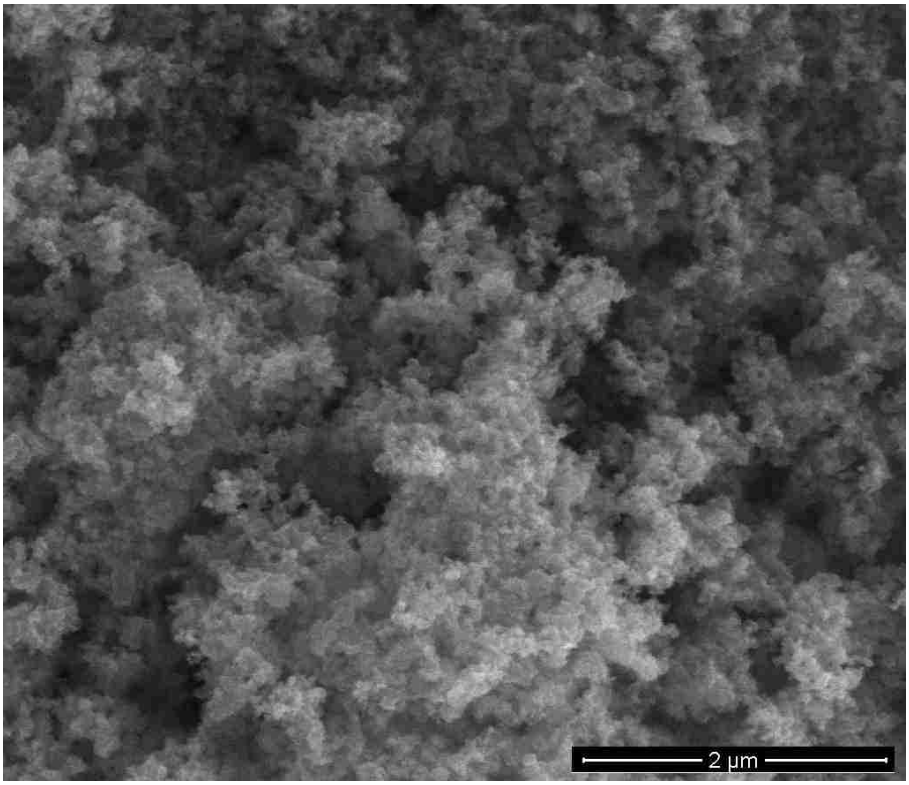

Figure 24. A representative SEM image of Pt50MSAC taken at 50K magnification and 7.50V.

Figure 24 shows a typical SEM image of Pt50MSAC. By scoring each pixel between 0 and 200 (representing its color gradient), a distribution can be generated showing what the average pixel gradient is. The mean gradient would be equal to the average height of the sample in the image, with lighter pixels being higher up, and darker pixels being further down. Furthermore, by comparing how neighboring pixels were scored compared to the mean, information about the morphology of the sample can be determined. These statistics are divided into 1^{st} and 2^{nd} order. The 1^{st} order statistics are roughness and skewness, which further separated into high and low frequency components, and are calculated using individual pixels.

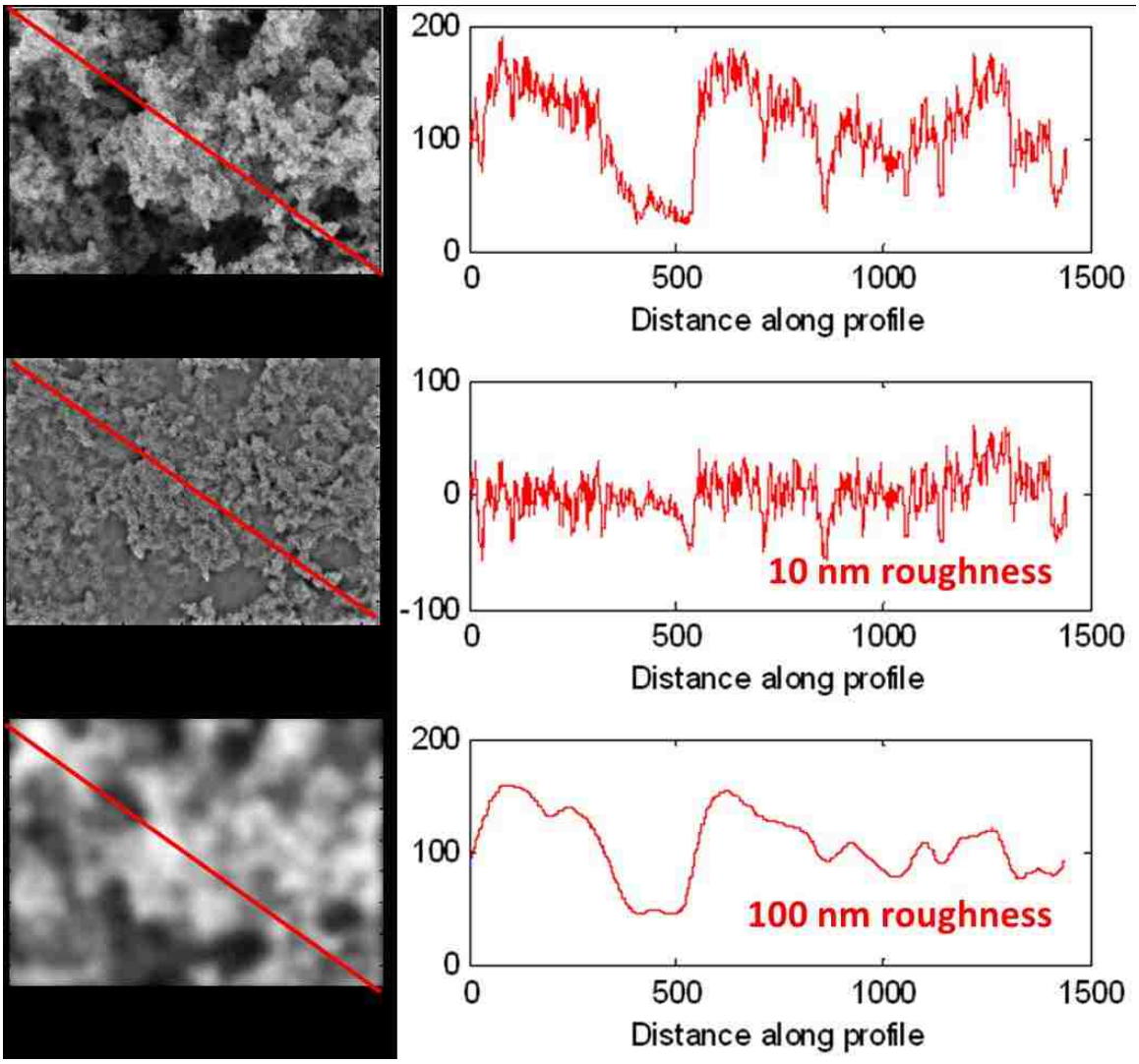

Figure 25. Line profiles of HSAC1 which show the total roughness (above), the high frequency roughness (middle), and the low frequency roughness (below).

Roughness determines how far individual pixels are from the mean value, or average height, and is considered a measure of porosity. By separating the roughness into high and low frequency components, it is possible to determine to what extent microporosity (10s of nm) or mesoporosity (micrometers) dominate the surface. Skewness is also essential to these calculations because it provides information about the pixel distribution, and therefore the roughness.

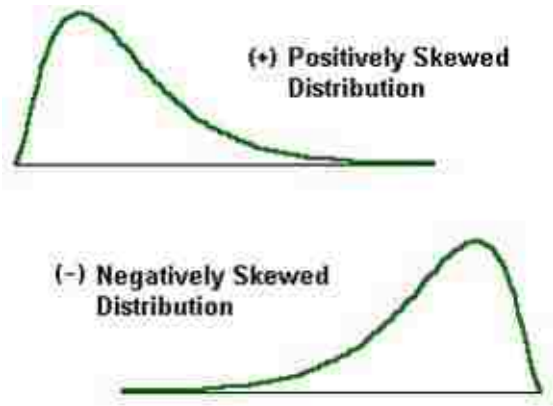

Figure 26. Illustration representing skewness

Because the images were taken at the same conditions, some of the samples appear brighter or darker based on the average height of the sample, but by measuring the skewness, it was possible to determine roughness statistics even if the image was dominated by valleys or peaks. Calculating the skewness of an image allowed for roughness statistics to be calculated accurately for all the images because they are dependent on deviations from the mean.

The second order statistics that were calculated from the images are contrast, correlation, energy/uniformity, and homogeneity. These statistics are texture parameters, and they derived by comparing a pixel pairs gradient scores or the image as a whole, as can be seen in Figure 27.

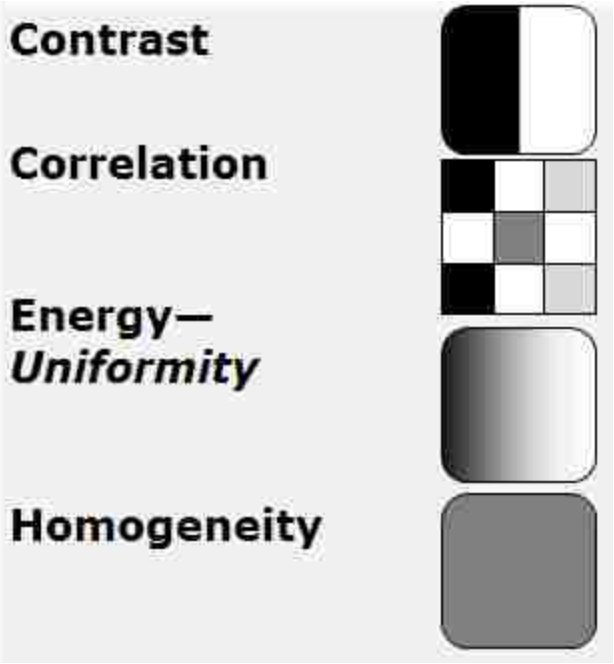

Figure 27. Visual representation of the 2nd order statistics that can be calculated using DIP. Contrast and Correlation measure local variation, while energy and homogeneity look at trends in the entire image.

Contrast determines local variation between neighboring pixels; samples with high contrast would be indicative of high microporosity. Correlation determines how probable it is for pixels with specific gradient scores to be near one another. Samples with high correlation scores are more associated with waviness and mesoporosity. Energy is similar to correlation, but determines if the image trends towards higher or lower scores in one direction. Homogeneity determines how similar an image is overall; an image with high homogeneity would be at roughly constant height, and variations in the pixel scores is likely due to variations in the carbon particle scale rather than the sample as a whole.

Finally, though DIP provided a means of characterizing the morphology of the samples in this project, it is important to note that this method has strict limitations. In order to calculate accurate statistics, it was necessary to capture images of the samples essentially identical conditions using a single microscope. Differences in the

magnification or microscope resolution would have changed the length scale associated with each pixel; changes to the voltage, brightness, or contrast would have led to differences gray-scale distribution of the pixels, altering the results as well. The statistics generated by DIP can only be considered reliable if all of the images for a study are processed at one time, and statistics from independently processed image sets are not comparable. Data derived from DIP are self-referential, meaning that outside the data set, an individual datum has no inherent context, and must be taken as part of a greater whole. As a result, any data analysis involving DIP generated statistics must use the entire data set in order to be consistent.

4.4.2 Principal Component Analysis

The electrochemical, microscopic, spectroscopic, and data processing techniques described in this chapter generated a large data set of highly diverse statistics. Mapping how the characteristics of individual samples change throughout the experiment would have been relatively simple, but drawing general trends applicable to the entire sample set was a far greater challenge. To do this, a multivariate analysis method is used to quantify the results, in this case principal component analysis (PCA). As a technique, PCA allows us to take a large data set, and to separate samples based on experimentally derived descriptors. For example, Figure 28, below, shows how some morphological factors, like homogeneity and skewness, are related to some chemical ones, in this case PtO content.

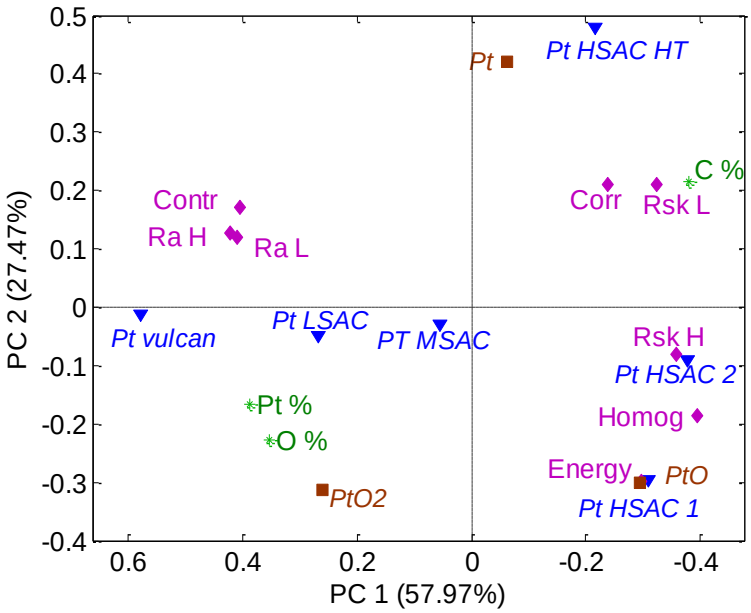

Figure 28. PCA biplot relating morphological descriptors, determined by SEM, to chemical speciation, determined by XPS, for a preliminary study

From I.T. Jolliffe's *Principal Component Analysis* "the central idea of principal component analysis (PCA) is to reduce the dimensionality of a data set consisting of a large number of interrelated variables, while retaining as much as possible of the variation present in the data set. This is achieved by transforming to a new set of variables, the principal components (PCs), which are uncorrelated, and which are ordered so that the first *few* retain most of the variation present in *all* of the original variables."[67] By using PCA, it is possible to visualize the differences between samples using biplots similar to Figure 28. Samples in the same quadrant are statistically similar to one another, and factors in those quadrants can be considered related to those samples. The axes in the plot separate the factors based on variability in the data set; the x-axis denotes principal component 1, which has the largest variation, while the y-axis represents principal component 2, which has the second largest variation. Variables or samples near the extremes of an axis are highly correlated with that principal component, and are

responsible for much of the variance. Conversely, variables or samples near the origin of the biplot contribute little to the overall variance, and are considered to be the "average." Depending on the sample set and the complexity of the data set, additional principal components may also capture a significant portion of the variance in the data.

5. Structural and Morphological Properties of Carbon Supports: Effect on Catalyst Degradation

In this study, carbon support materials and Pt-C catalysts were investigated. The electrocatalysts were subjected to accelerated stress testing (AST) to monitor performance losses. Electrode impedance spectroscopy (EIS) and cyclic voltammetry were used to examine cathode catalyst layer changes. The materials were also characterized using X-Ray photoelectron spectroscopy (XPS) and scanning electron microscopy (SEM), with the resulting data being processed using principal component analysis (PCA), a multivariate analysis method. Finally relationships were drawn between morphological and chemical parameters with various corrosive behaviors.

5.1 Materials and Methods

5.1.1 Materials

This study investigated the undecorated and 50wt% catalyst forms of the low surface area, mid-range surface area, and high surface area 1 carbons, in addition to the heat-treated form of HSAC1. The carbon materials were characterized in their powder form, while performance data was collected using a 50cm^2 fuel cell.

5.1.2 Performance Measurements

The performance data present in this work was obtained at Ballard Power Systems. In order to evaluate the performance and degradation losses of the Pt electrocatalysts, accelerated stress testing (AST) using an upper potential of 1.2V was used to study the effect of the carbon support on cathode degradation with respect to changes in cathode thickness, effective platinum surface area (EPSA), and kinetic performance. Capacitance

measurements were also taken using Electrode Impedance Spectroscopy (EIS). Capacitance is believed to be an indirect measure of carbon corrosion; small changes indicate low levels of corrosion while large changes significant corrosion levels.

5.1.3 Characterization

X-ray Photoelectron Spectroscopy (XPS) was chosen to obtain information on surface chemistry of the samples. The catalysts were investigated with a Kratos Axis Ultra spectrometer using an Al Ka X-ray source, with emission voltage of 12 kV and emission current of 20 mA. Both low resolution survey spectra and high resolution C 1s and Pt 4f spectra were acquired. Au powder was placed on each sample and Au 4f spectra were acquired. All XPS spectra from each sample were charge-referenced to Au 4f at 84eV.

SEM images were acquired using a Hitachi S-5200 at 2K and 50K magnification, and 7.5kV. 5 images were acquired per sample at each magnification, with the resulting images being analyzed using digital image processing software created at UNM. The images were analyzed for morphological parameters for roughness and texture parameters described in Chapter 4.4.1.

The ability to discriminate between different carbon chemical environments, not just elemental compositions, is one of the primary advantages of XPS in the characterization of carbon corrosion. Morphological properties such as size of particles, size of particles agglomerates, surface area, roughness, and porosity contribute equally to the corrosion process. Digital Image Processing (DIP) was applied to SEM and TEM images to extract statistical parameters, such as roughness, particle size distributions, shape parameters, and texture parameters, which all are related to morphology of carbon blacks.

5.1.4 Analysis

This multi-analytical approach provides a large set of variables (structural, physical and microscopic properties) which are related to the corrosion behavior of carbon blacks. Dealing with the large number of variables and finding correlations between them, coupled with classifying the samples, was an important challenge. Principal component analysis (PCA) was used as a tool to find samples which parameters are globally correlated or anti-correlated, and to facilitate visualization of the variables responsible for the correlations.

5.2 Results and Discussion

5.2.1 Electrochemical Data

The effect of the carbon support on cathode degradation with respect to changes in cathode thickness, and EPSA and kinetic performance is presented in Figure 29. The cathode layer thickness, EPSA loss, and subsequently the kinetic loss are least affected for low surface area carbon supports and show substantially higher degradation for high surface area carbons. As expected, catalyst degradation with Pt catalyst supported on high to low surface area carbons follows the trend: Pt50LSAC<Pt50MSAC<Pt50 HSAC1-HT<Pt50HSAC

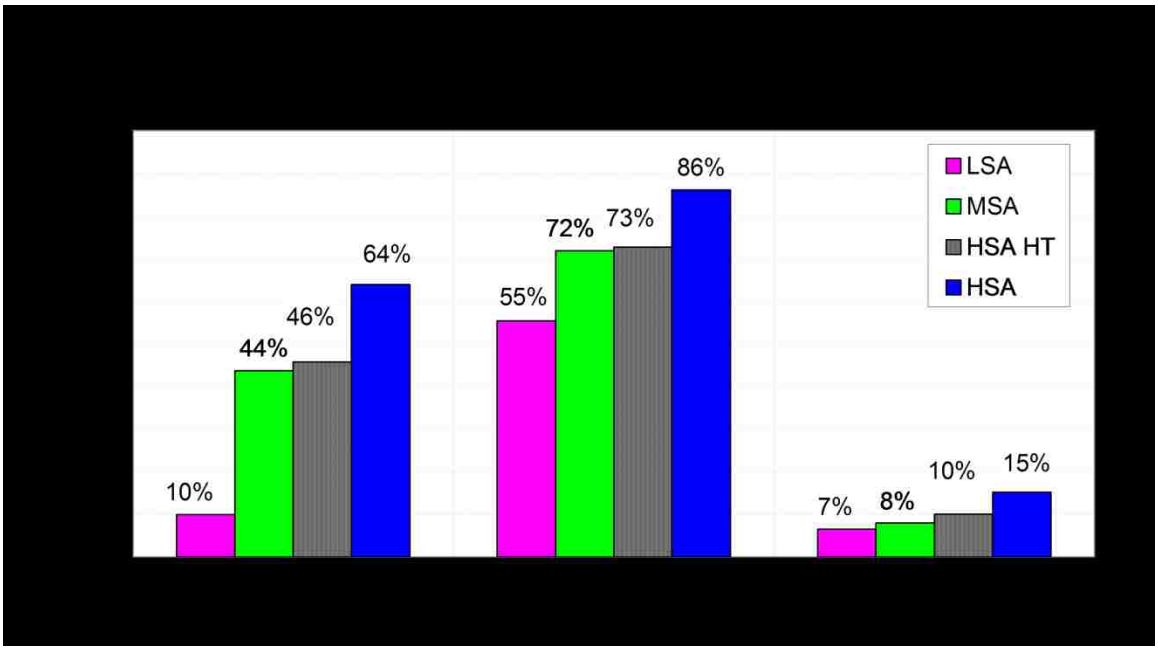

Figure 29. Comparison of Pt supported on various carbon supports subjected to the Pt dissolution AST (UPL-1.2V). Changes in catalyst layer thickness, EPSA, and kinetic performance.

As the Pt particle size and also Pt in the membrane (PITM) was found to be similar for all the tested carbon supported catalysts, the decrease in catalyst layer thickness and EPSA are thus mainly due to carbon oxidation rather than Pt dissolution.

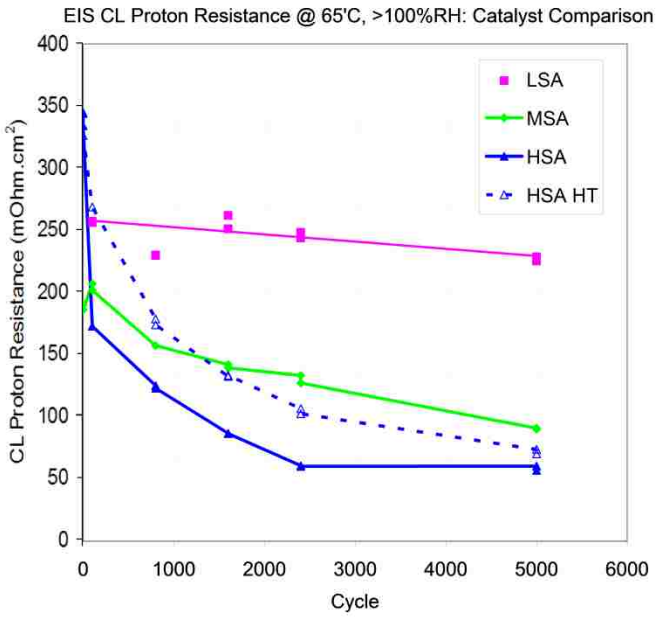

Figure 30. Changes to the proton resistance over 5000 cycles as determined by EIS for the catalyst materials. Pt50LSAC shows the smallest change while Pt50HSAC1 shows the largest.

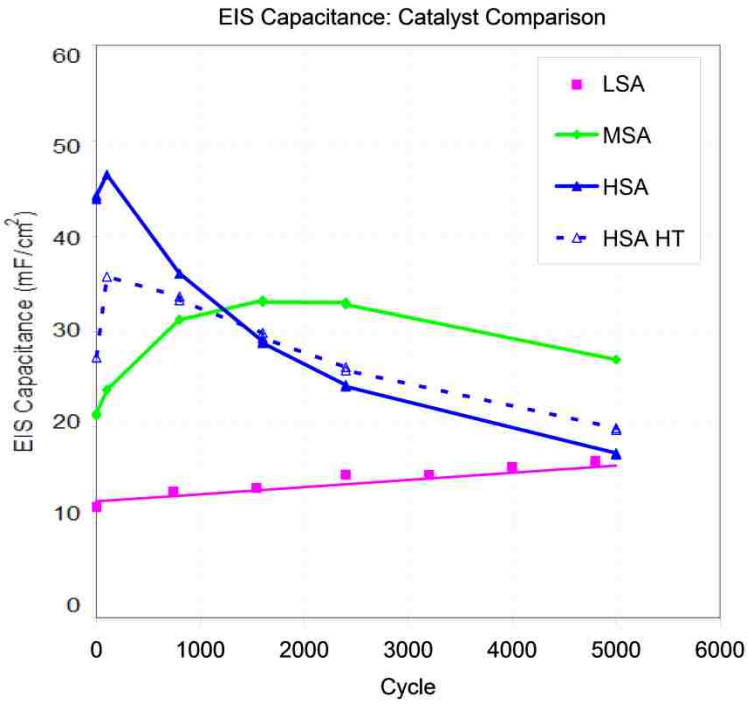

Figure 31. Changes to the capacitance for catalyst materials over 5000 cycles as determined by EIS. Pt50LSAC shows slight improvement while Pt50HSAC1 the largest drop.

Figures 30 and 31 show high frequency ionic resistance and the effect of capacitance of the catalyst layer and with progressive AST cycling. The EIS capacitance is believed to be an indirect measure of carbon corrosion, thus, as expected the low surface area supports show only a small change in capacitance while the medium and high surface area carbons reveal substantial change. The initial increase in capacitance is believed to be due to oxidation of the support surface, such that the surface states are becoming functionalized before the carbon is corroded and results in CO_2 evolution. Carbon oxidation changes the carbon surface to become more hydrophilic which would result in an increase in bulk proton conduction and/or water movement.[3] The functionalized carbon surface groups may also lead to a secondary proton path in the vicinity of the catalyst particles. Figure 31 illustrates how each carbon's proton resistance changes over time.

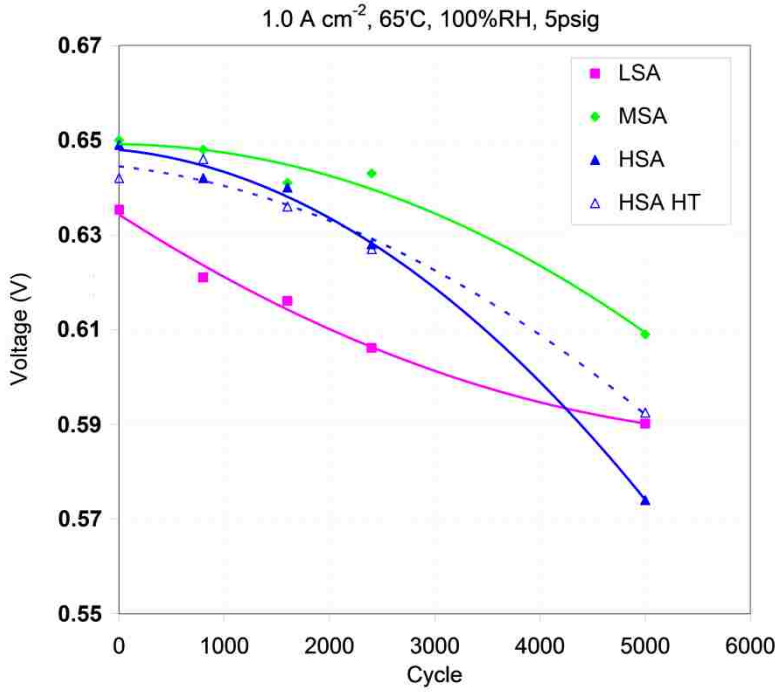

Figure 32: Performance of Pt-C catalysts at 1A/cm^2 over the course of the AST cycling protocol.

A comparison of voltage degradation for Pt catalysts on different carbon supports is shown in Figure 32. Consistent with the above discussion, the degradation rates are greater for catalysts with larger carbon support surface areas due to its susceptibility to carbon oxidation and corrosion. The performance degradation will depend on both, current density and initial performance, and number of AST cycles, thus at current densities < 1A/cm^2 the degradation rate could be substantially lower than those presented in Fig 32.The performance was found to follow the trend:

EOL = 2400 cycles: MSAC> HSAC1-HT~HSAC> LSAC
EOL = 5000 cycles: MSAC>HSAC1-HT~LSAC>HSA

After collecting the corrosion and performance data, the results needed to be correlated with the physical parameters of the support materials.

5.2.2 XPS results

Table I show XPS results for 6 types of carbon blacks and the same carbons decorated with 50% Pt.

Table I. Elemental Composition of Catalyst Supports With and Without Catalyst Along with Content of Pt Species

Sample	Carbon Blacks		Pt on Carbon Blacks			Pt	Pt-C	PtO
	C%	*O%*	*C%*	*O%*	*Pt%*	*71.4*	*72.3*	*73.2*
LSAC	99	1	80.5	11.1	8.4	39.1	22.9	38
MSAC	98	2	81.9	9	9.1	41.4	22.5	36.1
HSAC1	94.7	5.3	85.2	9.1	5.8	37.6	35.4	27.1
HSAC2	96.2	3.8	85.9	8.6	5.5	35.4	34.9	29.7
HSAC1-HT	--	--	93.1	3	3.9	70.3	20.5	9.2
Vulcan	93.7	6.3	72.4	17.6	10.1	41.6	22	36.4

Low and Medium surface area carbons have the lowest amount of oxygen and, therefore, surface oxides. High surface area carbons, except for HSAC1-HT, consist of approximately 4-5% oxygen, similar to the control carbon black, Vulcan. The heat treatment of HSAC1 took place following the decoration of platinum, meaning that HSAC1-HT does not exist. Decoration of these carbon blacks with Pt causes significant increase in oxygen for all samples. Of the decorated carbon blacks, Pt50LSAC and Pt50MSAC have the highest amount of Pt detected with 8-9%, close to that observed for Vulcan carbon. Pt50HSAC1 had the highest percentage of carbon and smallest percentage of Pt, but Pt50HSAC1-HT had significantly less O and Pt content.

Three types of Pt are detected for these samples, metallic Pt, Pt-C and PtO. Figure 33 shows the Pt 4f spectra for 2 samples, Pt50HSAC2 and Pt50HSAC1-HT. Platinum composition for Pt50LSAC and Pt50MSAC is nearly identical to that of Vulcan. The high surface area carbons result in catalysts with smallest relative amounts of metallic Pt and largest amounts of Pt monoxide, but Pt50HSAC1-HT showed double the relative metallic Pt content as the base form.

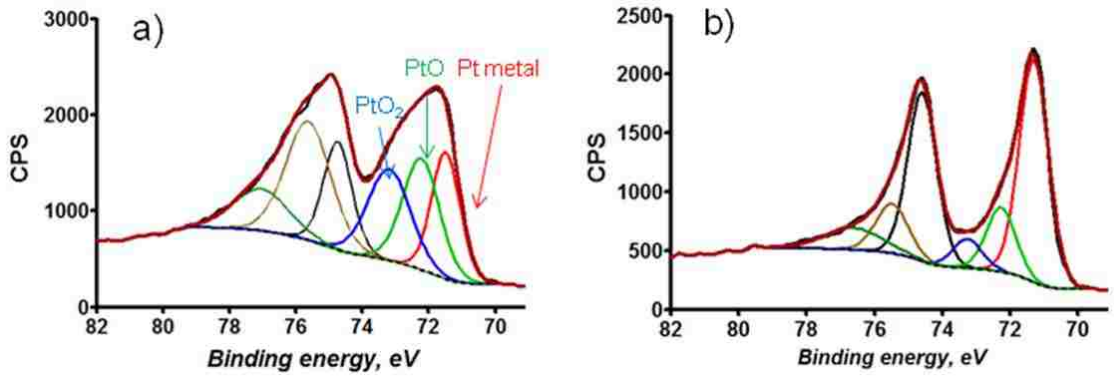

Figure 33: High resolution Pt 4f spectra for a) HSA2 and b) HSA HT samples. Increase in metallic content upon heat treatment is detected.

5.2.3 Scanning Electron Microscopy and Digital Image Processing

Scanning Electron Microscopy (SEM) images were acquired to obtain morphological information for carbon black and Pt-decorated samples. Figure 34 shows representative SEM images for low, medium and high surface area carbons along with SEM images from Pt-decorated samples.

Changes in morphology and porosity are, to some extent, obvious from visual inspection of the images, but quantitative information is required for a clear understanding of the differences between samples and correlating microscopy with performance and surface chemistry. Digital image processing (DIP) was applied to find a

representation of the intensity distribution of an image and to convert 2-D images into descriptors that are useful for morphology representation.

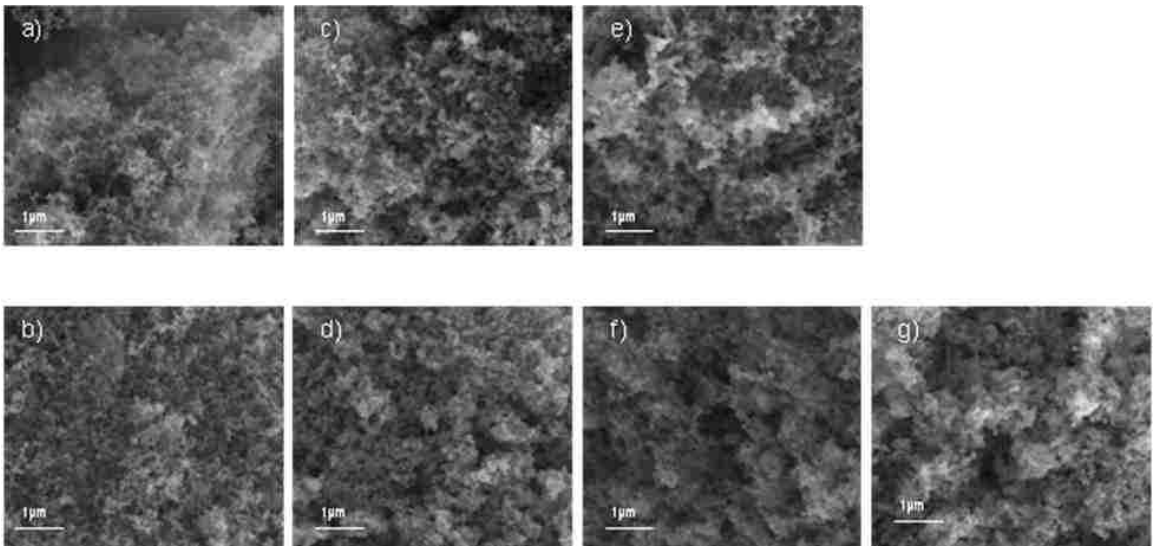

Figure 34. SEM images for carbon blacks a) LSAC, c) MSAC and e) HSAC1 and Pt-decorated samples b) Pt50LSAC, d) Pt50MSAC, f) Pt50HASC1 and g) Pt50HSAC1-HT samples.

Surface roughness is one of the most important statistical parameters which can be extracted by DIP.[68] The average roughness (*Ra*) is the arithmetic mean of the absolute values of the surface departure from the mean plane. Skewness, *Rsk*, of the roughness profile is also very important as it describes asymmetry of the roughness, indicating the image is being dominated by valleys (pores) or peaks. *Rsk* increases as relative amount of pores (dark values of intensity within images) increases.

A typical surface exhibits roughness superimposed over waviness. Waviness is due to the more widely spaced repetitive deviations (low-frequency component of SEM images) and roughness is due to the finer, random irregularities of surface texture (high-frequency component of SEM images). Waviness and roughness are responsible for different phenomena and processes in the electrocatalyst performance. Roughness is due to microporosity (high-frequency roughness) and roughness due to mesoporosity (low-

frequency waviness) are responsible for configurational and Knudsen diffusion regimes, respectively. Therefore it is important to evaluate waviness and roughness parameters individually. For this purpose, we have applied a high-pass filter to remove low-frequency component to produce a roughness image. Conversely, by applying a low-pass filter to remove high-frequency components from images, waviness image components can be obtained.

Texture arising from the repetition of local patterns is another very important feature used in DIP. Textural features such as ones based on grey scale co-occurrence matrices provide measures of such notions as contrast, randomness or directionality. Homogeneity, contrast (amount of local variation), correlation (linear dependency of grey levels of neighboring pixels) and energy (uniformity) were evaluated for images.

5.2.4 Principal component Analysis

Dealing with the large number of variables and finding correlations between them for the purpose of classification of samples by performance is an important challenge. Multivariate statistical methods of data analysis (MVA) are of critical importance in structure-to-property relationship modeling.[68] Principal Component Analysis (PCA) is used herein as a visualization tool to find samples which are globally correlated or anti-correlated, and to facilitate visualization of the variables responsible for the correlations. Figure 35 shows PCA biplot for roughness and texture parameters for carbon black samples only.

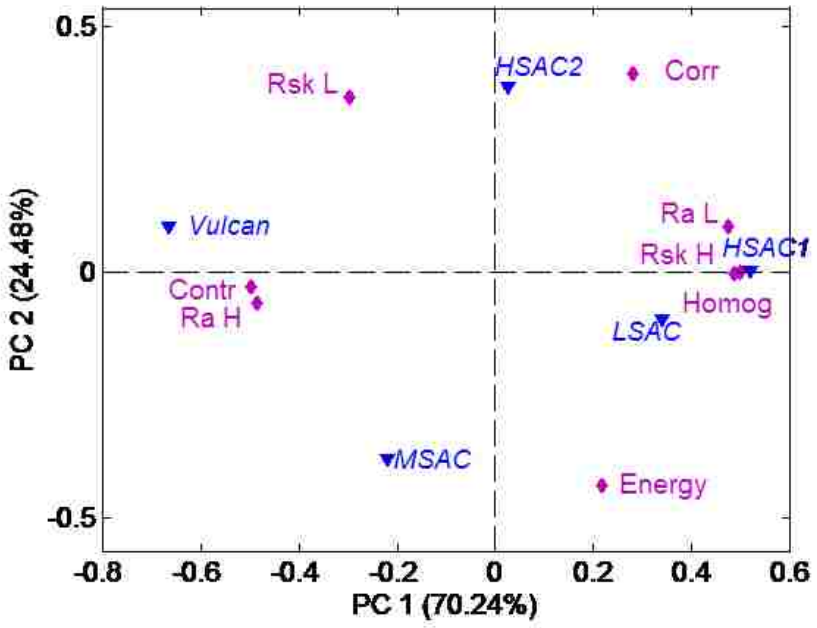

Figure 35. PCA biplot for roughness parameters for undecorated carbon black samples

Principal component (PC) 1 captures 70% of variance in the data and separates samples by heterogeneity. HSA and LSAC carbons have the largest mesoroughness and number of small pores and are less heterogeneous than the other supports. Vulcan and MSAC samples are the most heterogeneous and have the highest contrast, microroughness and number of large pores. Interestingly, SEM images from carbon blacks cannot directly describe surface areas due to signals limited by the sample-air interface.

Figure 36 shows PCA biplot for roughness and texture parameters for Pt-decorated carbon black samples. PC1 is plotted in reverse scale for comparison with classification of carbon black samples in Figure 35. PC1 also captures 70% of the variance in the data and according to classification of variables, separates samples by morphological criteria similar to the ones for undecorated carbon black samples. Pt deposited on Vulcan and Pt deposited on LSAC carbon have the highest roughness on both micro- and meso-regimes and the highest contrast. Both HSA carbons have high

homogeneity (order) and high porosity due to smaller and larger pores, resulting in higher surface area. The MSAC and HSAC1-HT samples lie on the zero x-axis for PC1, indicating that their morphologies are somewhere in the middle between the two categories discussed.

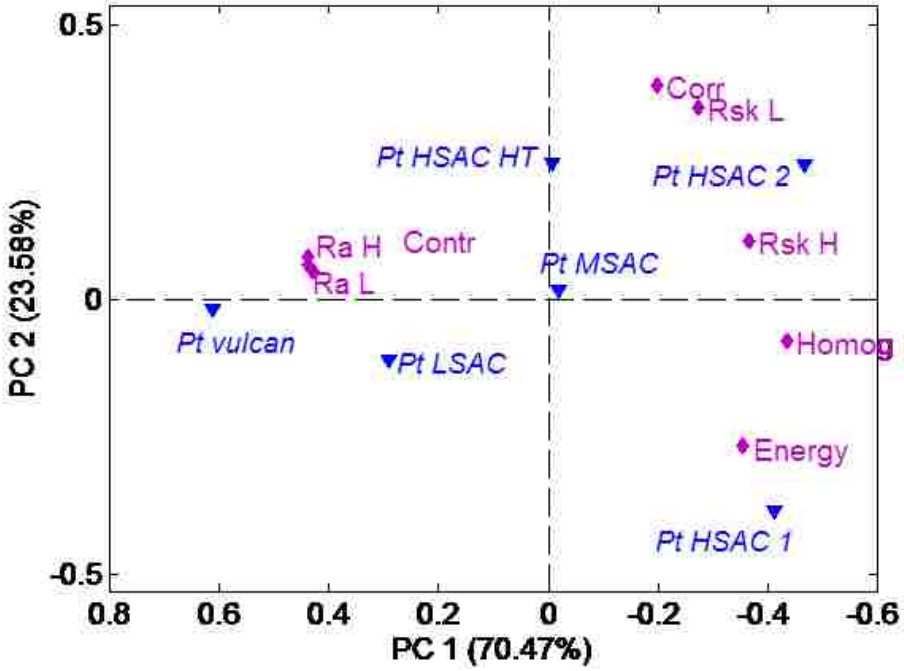

Figure 36. PCA biplot for morphology parameters for Pt decorated carbon black samples

In this case PC1 is directly proportional to surface area with the contributions in the order of Pt50HSAC2> Pt50MSAC= Pt50HSAC1-HT> Pt50LSAC=Pt50HSAC1> Pt50Vulcan. According to this PCA model, high surface area is related to high porosity in both meso and micro-regimes (Rsk), high energy and homogeneity, and inversely related to high roughness and contrast.

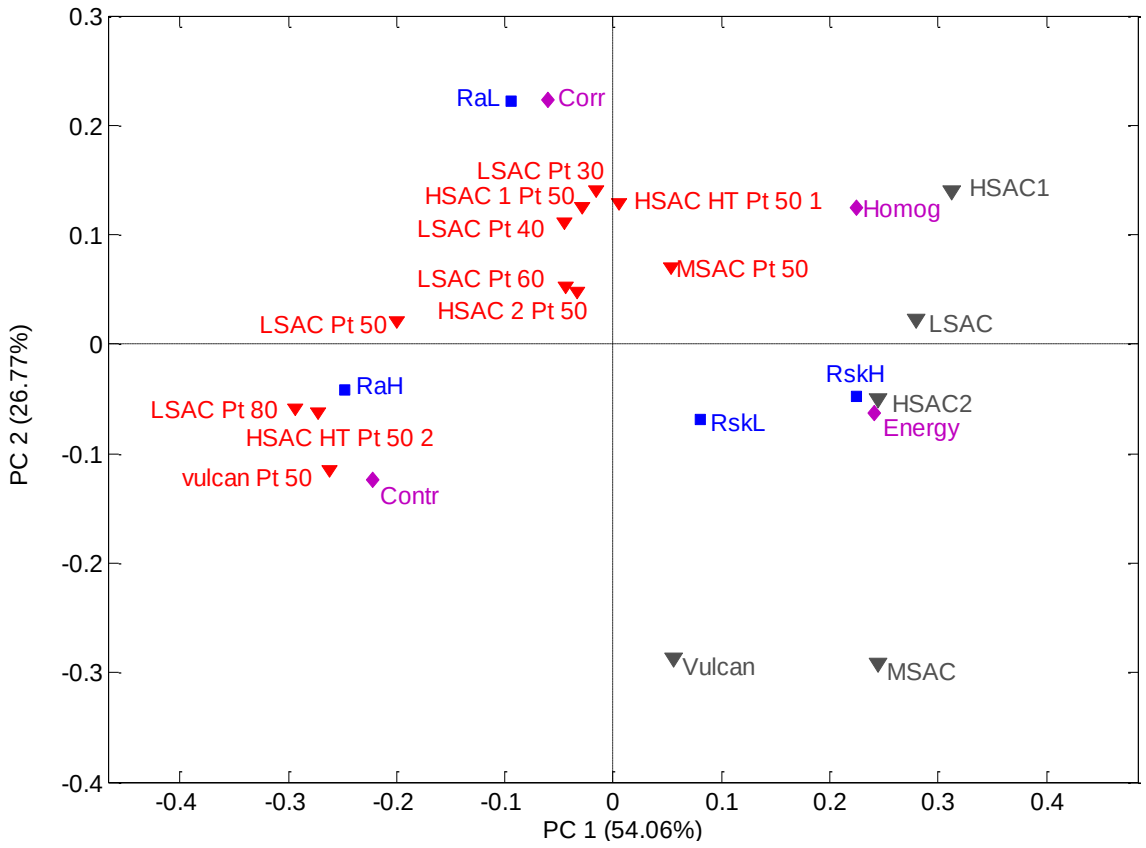

Figure 37. PCA Biplot showing SEM data for all samples; carbon supports are in grey, while catalysts are in red.

Figure 37 shows the combined data where roughness and texture parameters from both pure carbon blacks and Pt-decorated samples. Overall the undecorated carbons all contribute positively to PC1, and they also have the highest porosity on both the micro- and meso-scale. The catalysts, however, are more correlated with roughness and contrast, and it appears that the deposition process leads to a reduction in porosity for almost all catalyst samples.

Next, XPS data in Table I were combined with roughness and texture parameters extracted from SEM images for Pt-decorated samples and PCA model was applied.

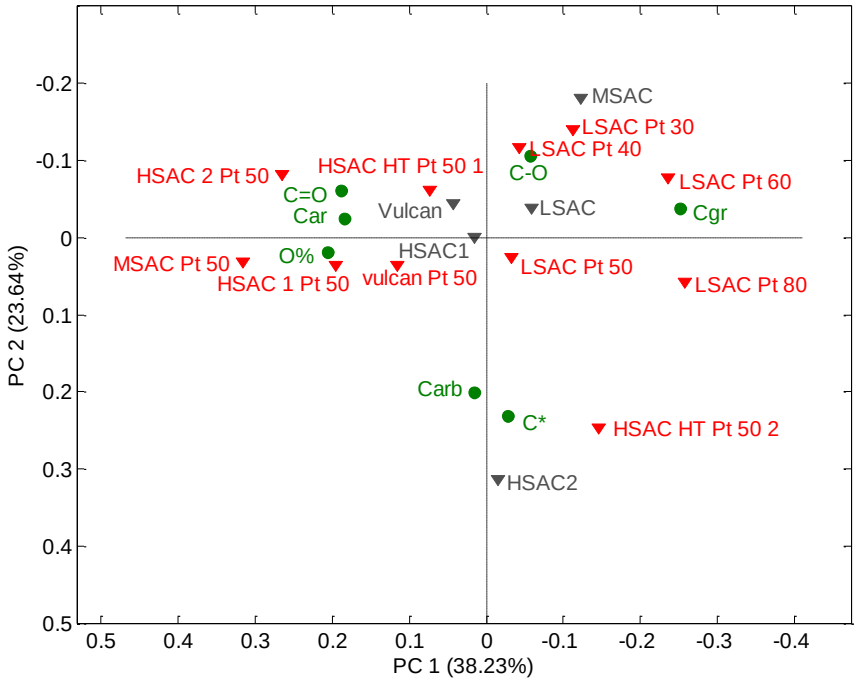

Figure 38. PCA biplot showing the C1s speciation for all sample materials; carbon supports in grey, catalysts in red.

Figure 38 shows the PCA plot for all of the samples and the carbon speciation data from XPS. It was found that the LSAC, HSAC1, and Vulcan supports were relatively unchanged following the Pt deposition process, but MSAC and HSAC2 showed drastic changes. It was also shown that for both the undecorated and catalyst forms, HSAC1 and Vulcan are chemically very similar. MSAC and HSAC2 showed large increases in their oxygen contents after Pt deposition, but post heat-treatment, Pt50HSAC2-HT was most similar to the undecorated form of HSAC2 than any of the other catalysts.

The SEM and XPS data were combined into one data set, and were processed using PCA. The results are shown in Figure 39.

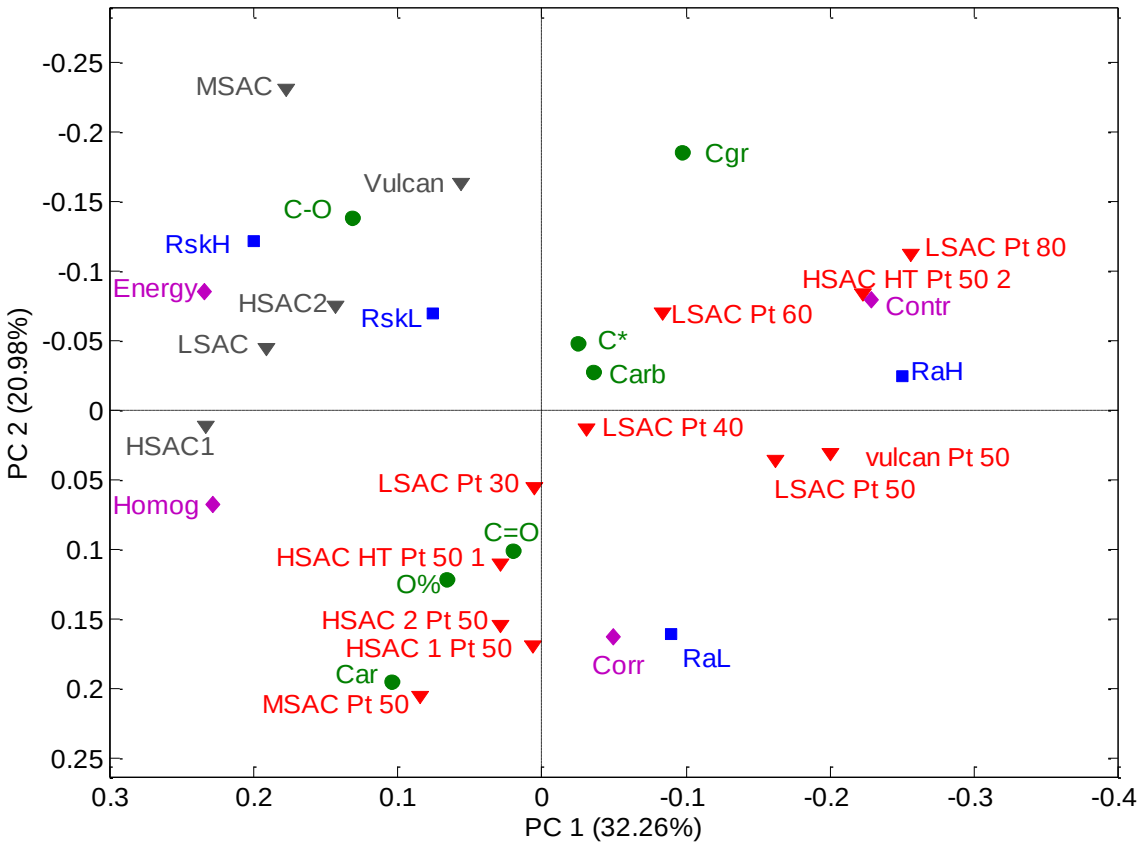

Figure 39. PCA biplot for combined XPS and morphological parameters for Pt-decorated carbon blacks.

PC1 separates components based on physical factors; samples with higher roughness on the right, and those with higher porosity on the left. PC2 separates the samples based on C1s speciation: more graphitic samples above, and samples with higher oxygen content below. Like the results shown in Figure 37, undecorated carbon supports were more correlated with porosity while catalysts were associated with surface roughness.

Finally, when we correlate XPS or SEM data with durability results, we see that the most durable sample (Pt50LSAC) is most correlated with graphite and platinum-carbide content, while the least durable samples are associated with carbon-oxygen species and platinum metal. These results can be seen in Figure 40.

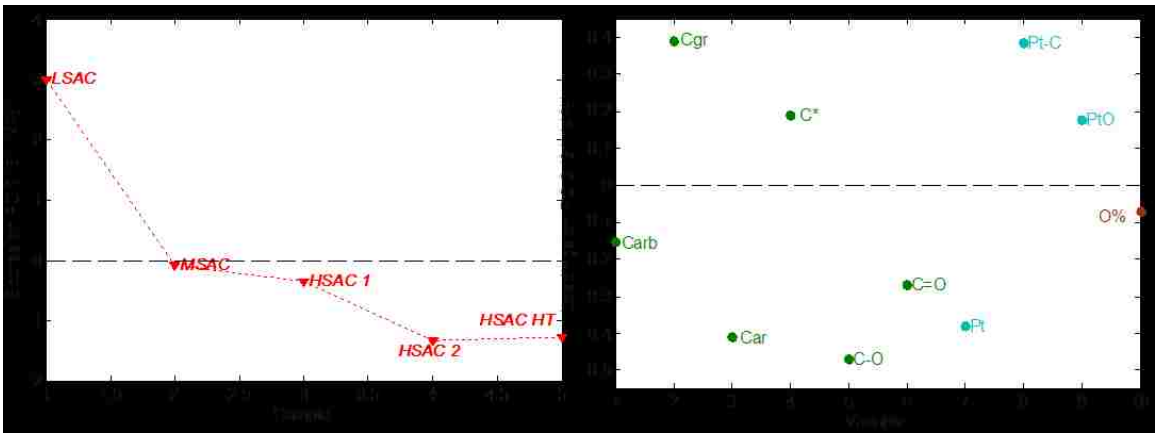

Figure 40. PCA comparing XPS results to durability results in order to determine what chemical species are most correlated with each carbon support.

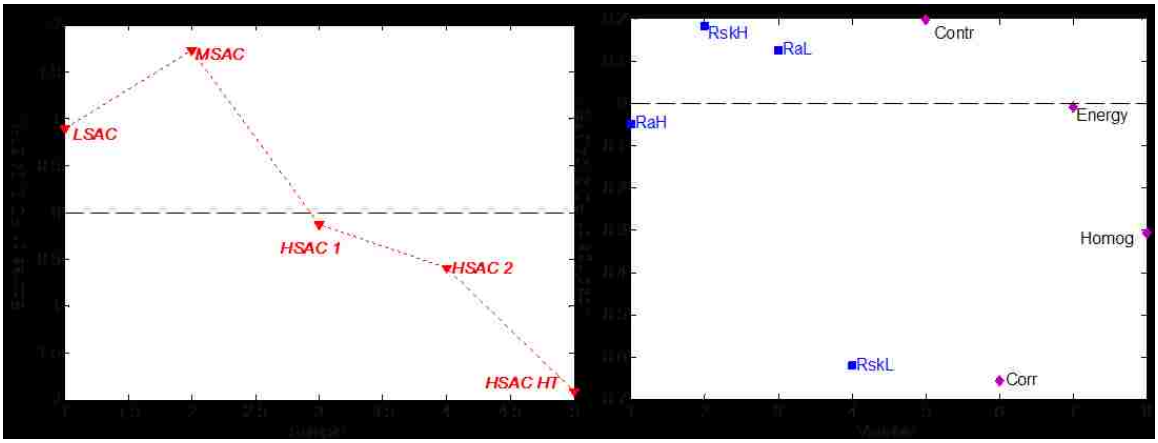

Figure 41. PCA comparing SEM results to durability results in order to determine what physical factors are most correlated with each carbon support.

Plotting SEM data against durability data gives results shown in Figure 41. The least corroded samples, LSAC and MSAC, are associated with high contrast, microporosity, and waviness, while the least durable materials are associated with high mesoporosity and are more homogeneous overall.

5.3 Conclusions

It was found that lower surface area catalysts suffered lower performance losses than higher surface area catalysts, as is consistent with the literature. In addition it was determined that catalysts with high roughness and high microporosity were more stable

than more homogenous and mesoporous samples. Microporosity was also found to be associated with surface oxygen content while roughness was found to be correlated with surface graphite. Finally, it was shown that undispersed catalysts that had high platinum carbon species and platinum oxide content were more stable than those with predominately platinum metal.

6. Effects of High Temperature and Relative Humidity to Pt-C Catalyst Composition and Performance

The object of this work was to identify which properties of carbon blacks change when Pt-based electrocatalysts supported on these carbon blacks are exposed to the abnormally high temperature and relative humidity. Platinum electrocatalysts prepared on several types of carbon black supports were subjected to high temperatures and relative humidity, and were characterized before and after aging. Electron energy loss spectroscopy (EELS) and X-ray photoelectron spectroscopy (XPS) were chosen to obtain information on graphitic content (degree of crystallinity) and the surface chemistry of the samples. Aberration corrected scanning transmission electron microscopy was used to gauge changes to the particle size distribution. Finally, rotating disk electrode (RDE) experiments were done to test the catalytic performance of materials before and after the *ex situ* aging process.[69]

6.1 Materials and Methods

6.1.1 Materials

In order to understand the effect of the type of carbon support on catalyst degradation, Pt catalysts on distinctly different carbon supports, Pt50LSAC, Pt50MSAC, Pt50HSAC1, and Pt50HSAC1-HT were investigated. The catalysts were characterized "as received" and after *ex situ* aging processes. The aging process was established in collaboration with Ballard Power Systems Inc.; the powder samples were aged for two hours at 150^{o}C and 100%RH. As received and aged samples were analyzed by XPS, STEM, EELS, and RDE experiments.

6.1.2 Characterization

X-ray photoelectron spectroscopy (XPS) was performed using Kratos Axis Ultra spectrometer using an Al Ka X-ray source, with emission voltage of 12 kV and emission current of 20 mA. Both low resolution survey spectra and high resolution C 1s and Pt 4f spectra were acquired. Au powder was placed on each sample and Au 4f spectra were acquired. All XPS spectra from each sample were charge-referenced to Au 4f at 84eV.

Electron energy loss spectroscopy (EELS) was used done using a JEOL 2010F TEM using a field emission gun as the source with a voltage of 200 kV, and beam energy of 0.1 kV. The as received and aged catalysts powders were investigated using this method. To ensure that the results were accurate, the spectra were acquired at 15 random locations per sample. Finally, highly ordered pyrolytic graphite (HOPG) was used as a reference sample because of its 100% sp2 bonding nature.

Aberration Corrected STEM images were acquired at JOEL 2200FS microscope at SHaRE user facility at Oakridge National laboratory. ACSTEM imaging was done in order to generate particle size distribution statistics to determine if the aging process had any significant effect on platinum nanoparticle stability over short time spans.

6.1.3 Performance Measurements

A portion of the as received and aged samples were weighed and added to a solution of 80/20 DI water/isopropyl alcohol and a 0.5% Nafion in DI water. The mixture was then sonicated to form a homogenous 4 mg/ml ink with 30 µl of the Nafion solution per milliliter of total solution. To test the samples, 10 µl of the catalyst ink were pipetted on to a rotating disk electrode, and was then dried for 30 minutes at 65^{o}C.

Using a rotation speed of 1600 RPM and 0.1M perchloric acid as the electrolyte, the electrode was cycled between 0 and 1.2 V (vs. RHE) 30 times at a rate of 100mV/s while

nitrogen bubbled through the electrolyte. This step was done to ensure a clean, uncontaminated surface. After the cleaning sweeps, oxygen gas was bubbled through the cell, and the electrode was cycled between 0 and 1.2 V (vs. RHE) at a rate of 5mV/s. The exchange current densities and Tafel slopes for ORR were then extracted from these curves to quantify performance losses due to aging. To calculate the exchange current density and Tafel slopes the influence of capacitance in the voltammograms caused by charge build up in the electrical double layer, followed by correcting the current for transport limitations. The Butler-Volmer equation was applied to calculate the exchange current density, which was then used to find the Tafel slope.

6.2 Results and Discussion

6.2.1 AC STEM

Figure 42 shows representative high resolution dark field AC STEM images from as-received electrocatalyst powders on four types of carbon support. Significant agglomeration of particles is evident for Pt50LSAC catalyst sample. Similar size and dispersion of particles are present for Pt50MSAC and HSAC1 catalysts. However, the large number of surface sites means these carbons will be more susceptible to corrosion, thus altering their performance and level of degradation. In order to stabilize the high surface area carbon catalyst, it was heat treated to cause some degree of graphitization. Larger Pt particles are evident from AC STEM micrographs for Pt50HSAC1-HT sample.

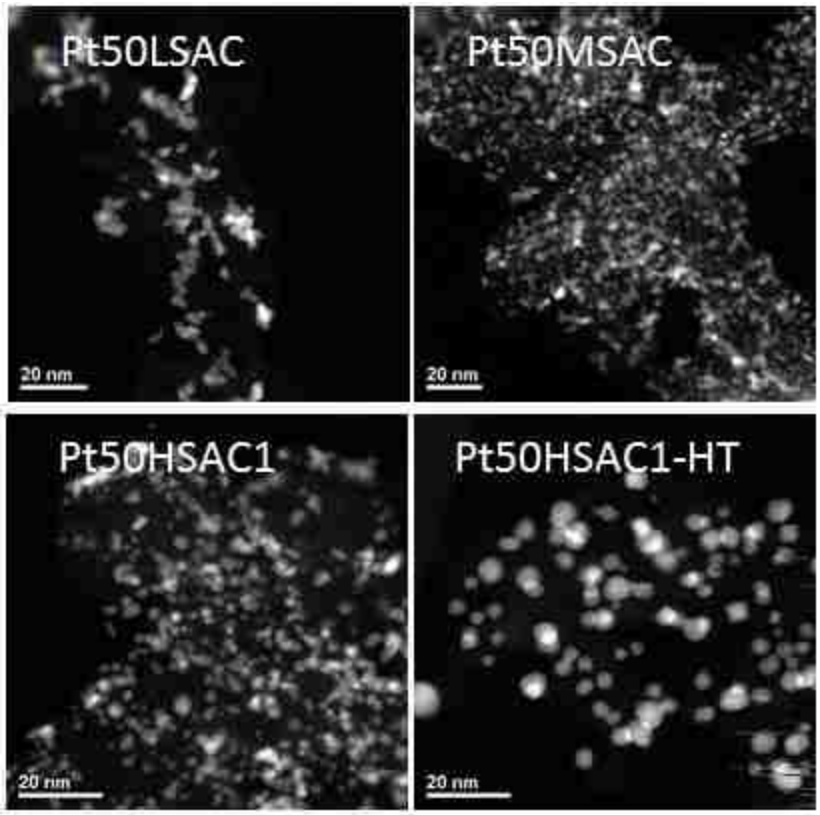

Figure 42.ACSTEM images of electrocatalysts

The particle size distributions of the catalysts were calculated before and after the aging process, and the results can be seen in Table II.

Table II. Average Particle Diameters for "As Received" and Aged Catalysts

Sample	As Received (nm)	Aged (nm)	% Increase
Pt50LSAC	2.3	3.3	41%
Pt50MSAC	2.1	2.9	36%
Pt50HSAC1	2.1	2.6	24%
Pt50HSAC1-HT	3.5	3.7	5%

All of the catalyst showed some growth, though Pt50HSAC1-HT showed the least; this is likely due to the initial heat treatment process Pt50HSAC1-HT underwent that the other catalysts did not. In addition, the particle growth came at the expense of the smaller catalyst nanoparticles, as shown in Figures 43 and 44.

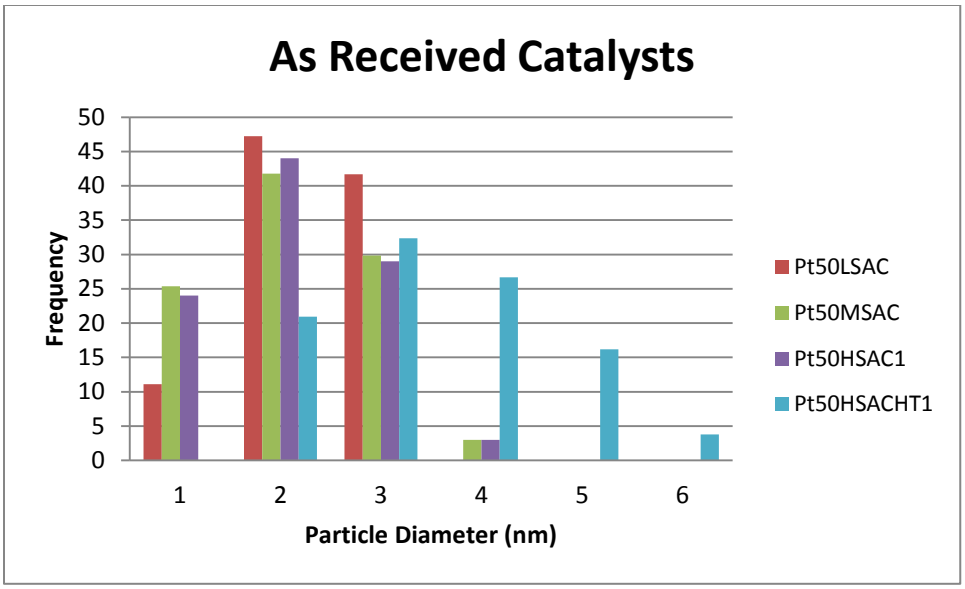

Figure 43. Particle size distribution of the "As Received" catalysts obtained by TEM imaging. For non-heat treated samples, most nanoparticles are between 2-3nm in diameter.

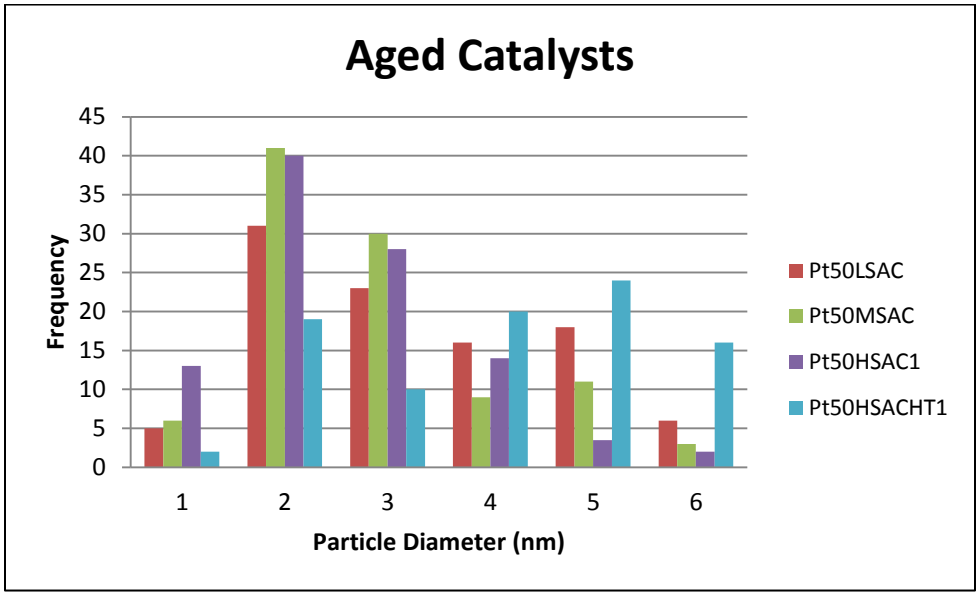

Figure 44. Particle size distribution for the aged catalysts obtained by TEM imaging. Larger nanoparticles (≥4nm) appear in significant quantities for all of the catalysts, though smaller nanoparticles still dominate.

Before the aging process, the non-heat treated catalysts were typically composed of nanoparticles between 2-3nm in diameter; following the aging step, nanoparticles larger than 3nm appear in greater frequency, while smaller nanoparticles become less prevalent.

6.2.2 XPS results

Figure 45 shows C 1s XPS spectra for Pt50LSAC and Pt50MSAC samples along with curve fit. A different ratio of graphitic peak at 284.5eV to the rest of the peak is obvious. Table III shows results of curve fit of XPS spectra for as-received and aged samples. The values shown are the average of 3 areas.

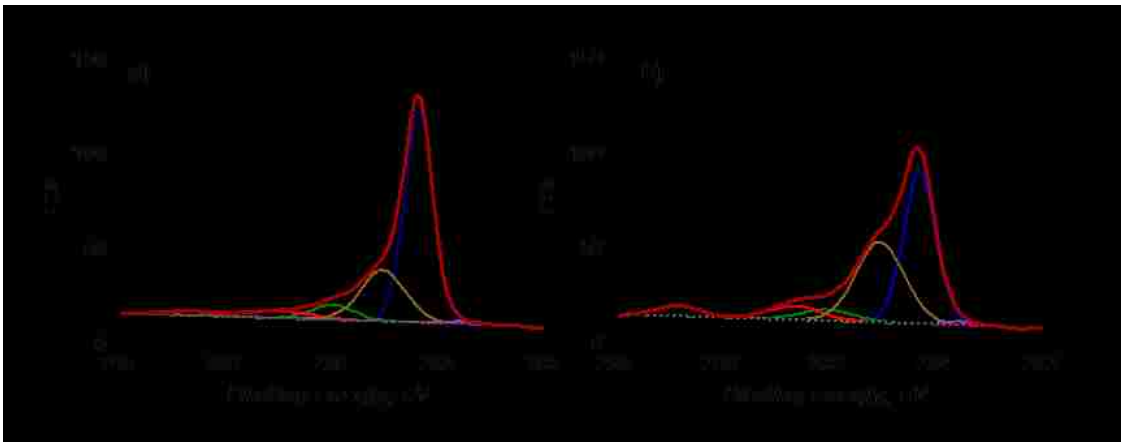

Figure 45. XPS High resolution C 1s spectra for a) Pt50LSAC and b) Pt50MSAC samples shown with curve fits used to deconvolute species as identified in Table II.

Table III. C speciation as determined from XPS spectra.

Sample	C gr	C-C	C*-C-X	C-OH/ C-OC	C=O
Binding Energy (eV)	*284.5*	*285.1*	*285.7*	*286.7*	*289.1*
		As-received			
Pt50LSAC	59.8	25.4	6.1	5.7	2.9
Pt50MSAC	40.2	41.0	8.6	5.9	4.4
Pt50HSAC1	45.6	35.8	6.9	7.0	4.7
Pt50HSAC1-HT	57.7	26.4	3.8	8.6	3.5
		Aged			
Pt50LSAC	59.7	21.4	6.1	9.4	3.4
Pt50MSAC	56.6	23.0	8.1	8.7	3.6
Pt50HSAC1	56.4	23.5	5.6	11.8	2.8
Pt50HSAC1-HT	53.4	25.8	6.9	9.4	4.6

For as-received samples, the graphite content is mixed and shows no clear trend based on surface area; however the samples with lowest graphitic content also have the highest amounts of aliphatic carbons. After the aging process, the surface chemistry of the samples show is more homogeneous, and they become more likePt50HSAC1-HT which showed little change due to the aging process.

Aging of Pt50LSAC and Pt50HSAC1-HT catalyst powders cause insignificant changes in the amount of graphitic carbon. The largest changes are detected for Pt50MSAC catalyst where an approximately 30% increase of graphitic content is observed and Pt50HSAC1 sample with an approximately 25% increase. For both of these samples, decrease is amorphous aliphatic carbon is detected. Additionally, the relative

amount of surface oxides increases with aging even though the total amount of oxygen is decreased by ~50% for all samples.

The total platinum content detected by XPS, as detailed in Table IV, increased for all four samples with aging. Due to surface sensitivity of XPS sampling depth, this result might point towards significant segregation of Pt towards top layers upon heat treatment. Similar amounts of platinum were found for all samples after aging.

Table IV. Platinum Surface Content Comparison as Calculated from XPS.

Sample	Pt % as-received	Pt % aged
Pt50LSAC	4.3	6.6
Pt50MSAC	2.8	7.5
Pt50HSAC1	2.5	6.1
Pt50HSAC1-HT	1.9	4.7

Figure 46 and Table V show results of curve fitting Pt 4f spectra for as-received and aged samples.

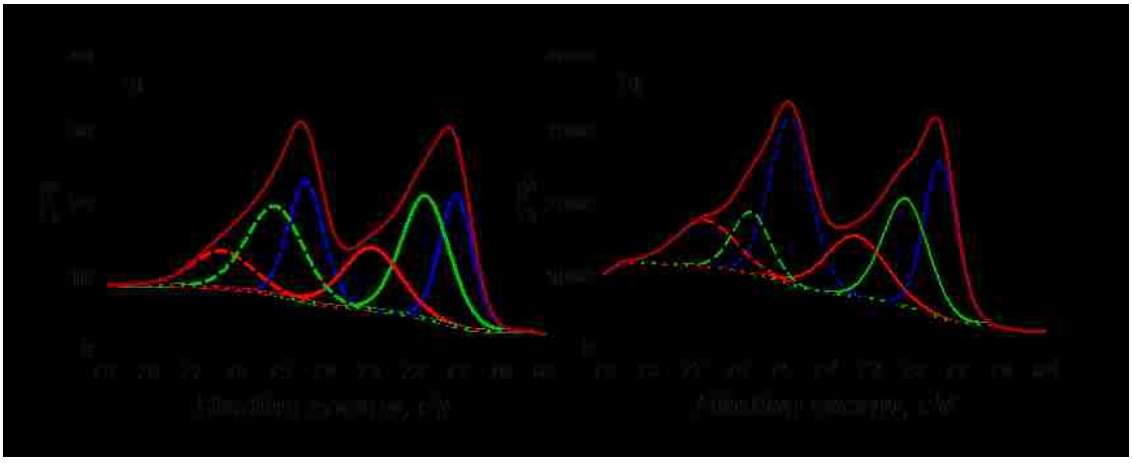

Figure 46.Platinum speciation for Pt50LSAC before (a) and after ex situ aging (b)

Table V. Pt speciation as determined from XPS spectra.

Sample	Pt	Pt/Pt-CxHy	PtO/ Pt(OH)2
Binding energy (eV)	*71.1*	*71.7*	*72.8*
	As-received		
Pt50LSAC	30.4	45.7	23.9
Pt50MSAC	33.5	36.2	30.2
Pt50HSAC1	40.9	34.0	25.1
Pt50HSAC1-HT	59.1	32.8	8.1
	Aged		
Pt50LSAC	40.0	26.8	33.2
Pt50MSAC	42.0	26.8	31.2
Pt50HSAC1	41.3	22.0	36.6
Pt50HSAC1-HT	47.4	23.7	29.0

In as-received catalyst samples, increase of surface area causes an increase in relative amount of metallic Pt. The heat treated Pt50HSAC1-HT catalyst sample has even larger degree of Pt reduction. After aging, all catalyst samples result in very similar composition with approximately 40% of metallic Pt and 30% of oxides. An increase in metallic Pt is observed with decreasing surface area of the catalyst supports. Pt50LSAC and Pt50HSAC1 showed large increases in oxides while Pt50MSAC was unchanged. Pt50HSAC1-HT showed the largest formation of oxides. Finally a 30-40% loss of Pt bound to carbon is observed for all samples, correlating well with the loss of amorphous carbon detected by C 1s spectra.

To summarize, XPS shows that for Pt50LSAC catalyst, heat treatment introduces no changes in carbon speciation, but significantly increases relative metallic and platinum oxide content with accompanying loss of Pt-C. Pt50MSAC catalyst displays large changes in both carbon and Pt compositions. Pt50HSAC1 catalyst shows no changes in metallic Pt percentage, but very significant loss of amorphous carbon and Pt bound to C. Pt50HSAC1-HT catalyst has the smallest changes detected in carbon but significant loss of metallic Pt and increase in PtO. Thus, the major results of aging of electrocatalysts is a loss of amorphous carbon, accompanied by a loss of Pt bound to it and simultaneous segregation at the very top surface of metallic Pt particles covered by Pt oxide.

The ability to discriminate between different carbon chemical environments, not just elemental compositions, is one of the primary advantages of XPS in the characterization of carbon corrosion; however, EELS is the preferred method to quantitatively extract the sp^2 fraction of carbon-based materials from carbon K-edge spectrum.

6.2.3 EELS results

Table VI shows the percent of sp^2 carbon determined from EELS spectra for 4 samples as received and after *ex situ* aging treatment at 150^{o}C in air 100% humidity. Similar to the XPS results, Pt50HSAC1-HT is more similar to Pt50LSAC in terms of graphite content (~80%), than it is to Pt50HSAC1, which is approximately 60% graphite, while Pt50MSAC is composed of roughly 70% graphite. Aging samples at 150^{o}C in 100% relative humidity results in the samples becoming quite similar with graphite contents ranging from 77 to 85%. The trend in relative graphitic content for aged samples is the same as for as-received samples, but the range of it is smaller.

The trend in change of graphitic content determined by EELS is very similar to that detected by XPS. This might be due to surface sensitivity of XPS in comparison with EELS, which points towards larger relative amounts of surface carbon oxides.

Table VI. sp^2 percentage determined from EELS spectra

Sample	As-received	HT	% Increase
LSAC50	78.7%	85.0%	*8.0%*
MSAC50	69.7%	79.2%	*13.6%*
HSAC50	59.4%	77.3%	*30.0%*
Pt50HSAC1-HT	80.2%	83.6%	*4.2%*

Figure 47 plots percent of graphitic content determined by XPS vs. that determined by EELS for both as-received and aged samples. A good correlation is observed for both sets of samples. For as-received samples, smaller spread of values detected by XPS indicates that surface is different from the bulk and surfaces of all catalysts are more similar to each other than the bulk of catalysts. Aged samples are very similar to each other as detected by both methods, but again similarity is larger at the very top 10 nm as seen by XPS. The graphitic carbon content of all samples after aging is similar to that of untreated Pt50LSAC and Pt50HSAC1-HT catalyst samples.

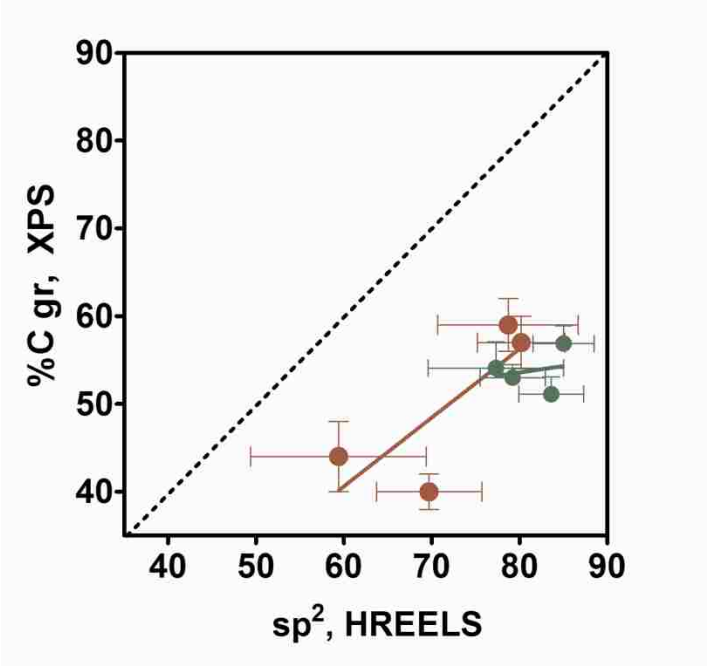

Figure 47. Percent graphitic carbon as determined by XPS vs. %sp2 content as determined by EELS

6.2.4 RDE results

Catalyst performance losses were quantified using rotating disk electrode experiments. Two sets of catalysts were tested for this study: as received catalysts and ex-situ aged catalysts. The open circuit voltages, limiting current densities, and voltage region exhibiting a Tafel slope of 60mV/dec were calculated for the catalysts, and the results are shown Tables VII, VIII, and IX.

Table VII. Open Circuit Voltages for "As Received" and "Aged" Catalysts

Sample	As-received	After Aging	Change (mV)
Pt50LSAC	879.5	926.4	46.9
Pt50MSAC 50	864.9	871.9	7.0
Pt50HSAC1	858.9	894.4	40.3
Pt50HSAC1-HT	849.2	873.9	24.7

Table VIII. Limiting Current Densities (mA/cm^2)

Sample	As-received	After Aging	% Change
Pt50LSAC 50	-5.91	-5.26	-11.1%
Pt50MSAC 50	-6.11	-6.17	0.9%
Pt50HSAC1	-5.15	-4.90	-11.0%
Pt50HSAC1-HT	-4.08	-5.32	30.2%

Table IX. Center of the 60mV/dec Tafel Region for "As Received" and Aged Catalysts

Sample	As-received	After Aging
Pt50LSAC 50	1.128-1.132	1.133-1.138
Pt50MSAC 50	1.136-1.141	1.133-1.139
Pt50HSAC1	1.132-1.136	1.126-1.132
Pt50HSAC1-HT	1.137-1.142	1.130-1.137

The data shows that through the *ex situ* aging, the performance statistics for the catalysts were mixed. While XPS and EELS data showed that relative graphitic content and amount of metallic Pt increase with aging, the performance of the catalysts were unchanged. All the catalysts achieved higher open circuit voltages after the aging process, but only Pt50HSAC1-HT showed an improvement in the limiting current. As shown in Table VII, the center of the 60mV/dec Tafel slope region was essentially unchanged, but because they are well above OCV, these regions are also unattainable for practical applications.

Correlation of surface carbon and Pt speciation as determined by XPS with electrochemical performance indicates that absolute amount of graphitic content is not the only parameter responsible for better stability. Relative distribution of Pt particles on

graphitic and amorphous carbon is as responsible for the losses of catalytic activity. After aging, the largest losses that resulted in the degraded performance are associated with losses of amorphous carbon and associated dispersed Pt.

While decreased performance due to aging is a well-documented phenomenon, seeing an increase in the Tafel slope and exchange current density of HSAC1-HT catalyst is unexpected. [9, 20, 49] Aging of this sample caused smallest changes to carbon chemistry and caused loss of metallic Pt with accompanying significant growth of PtO.

6.3 Conclusions

Ex situ heat treatment at 150^{o}C and 100%RH of four carbon supported platinum catalysts was performed in order to determine the effect graphitic content has on catalyst performance. The samples were analyzed using XPS, EELS, and RDE experiments. Both XPS and EELS results showed that graphite and metallic platinum content increased due to the heat treatment, and that the surface of the samples differed from the bulk. In addition, it was shown that after aging catalysts displayed decreased performance. After aging, the largest losses that resulted in the degrading performance are associated with losses of amorphous carbon and associated Pt-C species. Relative distribution of Pt particles on graphitic and amorphous carbon is thus critical parameter responsible for the catalytic activity and stability.

7. *Ex situ* Characterization of AST Cycled MEAs

The objective of this study was to characterize physical and chemical changes of degraded MEAs, and to correlate these changes to perceived performance losses. Multiple carbon support materials and catalysts of different loadings were tested as cathode catalysts for MEAs. These MEAs were cycling using AST protocols in order to rapidly degrade the cathode catalyst portion of the cell. Conditioned and degraded materials were then analyzed using XPS, to quantify chemical changes, and SEM, to quantify physical changes. These data sets were then processed using PCA in order to draw correlations between the chemical, physical, and performance changes observed.

7.1 Materials and Methods

7.1.1 Samples

This study investigated 6 catalysts: Pt50LSAC, Pt80LSAC, Pt50HSAC1, Pt50HSAC1-HT, Pt50HSAC2, and Pt50HSAC2-HT. These samples were used as the cathode catalyst for the MEAs, and were tested at loadings of 0.4mgPt/cm^2. The anode portion of the membrane used Pt50LSAC at a loading of 0.1mgPt/cm^2, and membrane was Nafion® NR-211.

7.1.2 MEA Testing

MEAs were operated at 75^{o}C, 100%RH with 5 psig back pressure of hydrogen and air on the anode and cathode sides, respectively. The cells were run at high stoichiometric ratios. The MEAs were conditioned overnight by being held at a current density of 1.3A/cm^2 at the standard operating conditions. Following the conditioning step, the BOL polarization curves for the membranes were obtained. The fuel cells using one of the six cathode catalyst were then cycled from 0.6V for 30s to 1.2V for 60s. MEAs using Pt50LSAC as the cathode, however, were subjected to additional cycling protocols which

changed the upper potential limit (UPL) to 1, 1.3, or 1.4V (vs. RHE). The purpose was to determine how the catalyst reacts to different potentials; Pt50LSAC was chosen based on previous experiments that proved it was the most stable catalyst in the sample set. Irrespective of which AST protocol was used, the cells were cycled 4700 times or until they were unable to achieve a current density of $0.6A/cm^2$ (considered the end of life) when the final polarization curves were obtained.

7.1.3 XPS Analysis

Non-run, conditioned and degraded CCMs were analyzed at UNM using a Kratos Axis Ultra spectrometer using an Al Ka X-ray source, with emission voltage of 12 kV and emission current of 20 mA. Both low resolution survey spectra and high resolution C 1s and Pt 4f spectra were acquired. Au powder was placed on each sample and Au 4f spectra were acquired. All XPS spectra from each sample were charge-referenced to carbon-carbon single bonds at 285.4eV. High resolution spectra for carbon, fluorine, oxygen, and platinum were acquired to determine to what extent chemical shifts had altered the carbon support, platinum nanoparticles, or Nafion® ionomer.

7.1.4 Digital Image Processing

SEM images were acquired for non-run, conditioned, and degraded CCMs. The images were taken at 2.5K and 50K magnification at a voltage of 1kV. Multiple locations were chosen per sample, and the locations were chosen randomly in order to prevent user bias from influencing the results. The images were analyzed through Digital Image Processing software to quantify changes to sample morphology due to conditioning and accelerated stress testing.

7.2 Results and Discussion

7.2.1 MEA Results

The beginning of life polarization curves are shown below in Figure 48 and the polarization curves obtained after 4700 cycles is shown in Figure 49. The beginning of life performance for all of the catalysts is fairly similar with regards to the surface area and platinum loading.

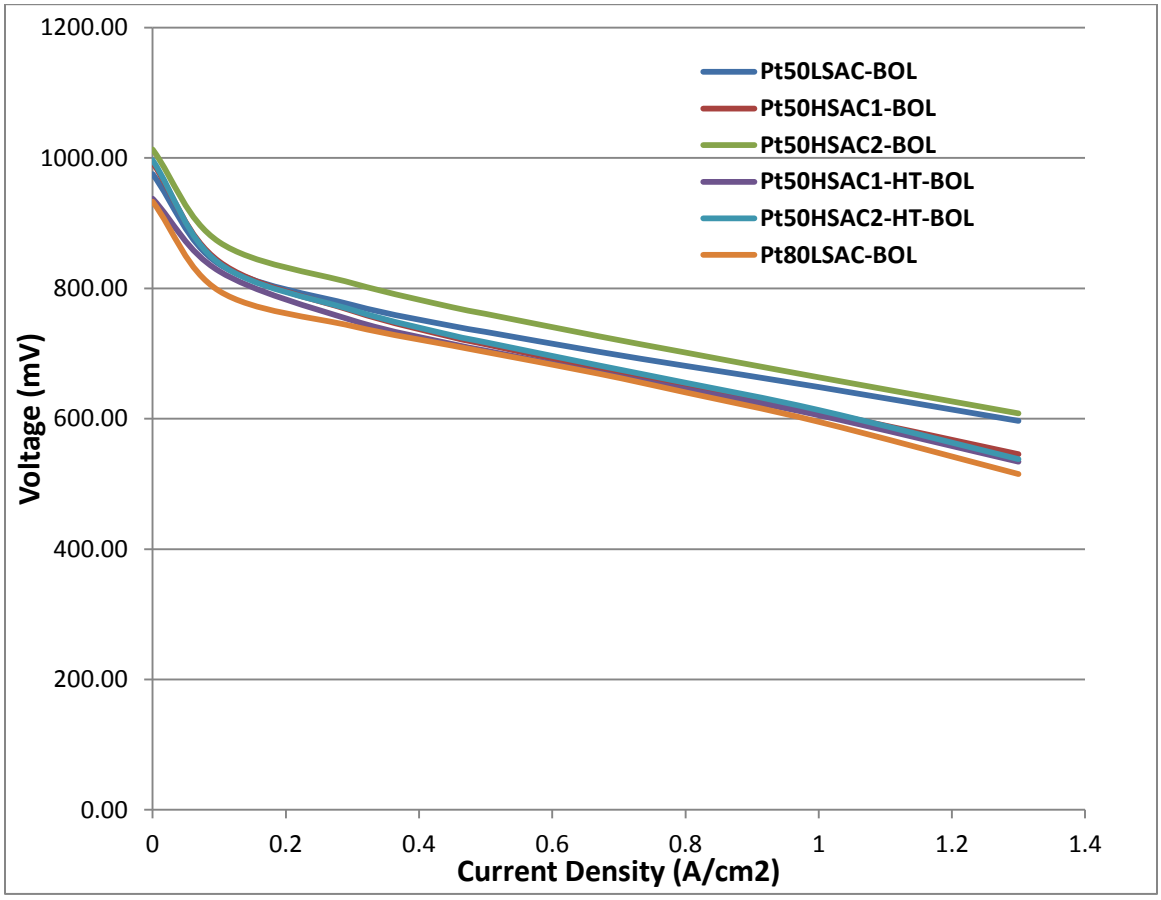

Figure 48. BOL polarization curves for the 6 cathode catalysts investigated in this study. The performance of the catalysts is fairly similar irrespective of surface area or loading. Data obtained at Ballard Power Systems, Inc.

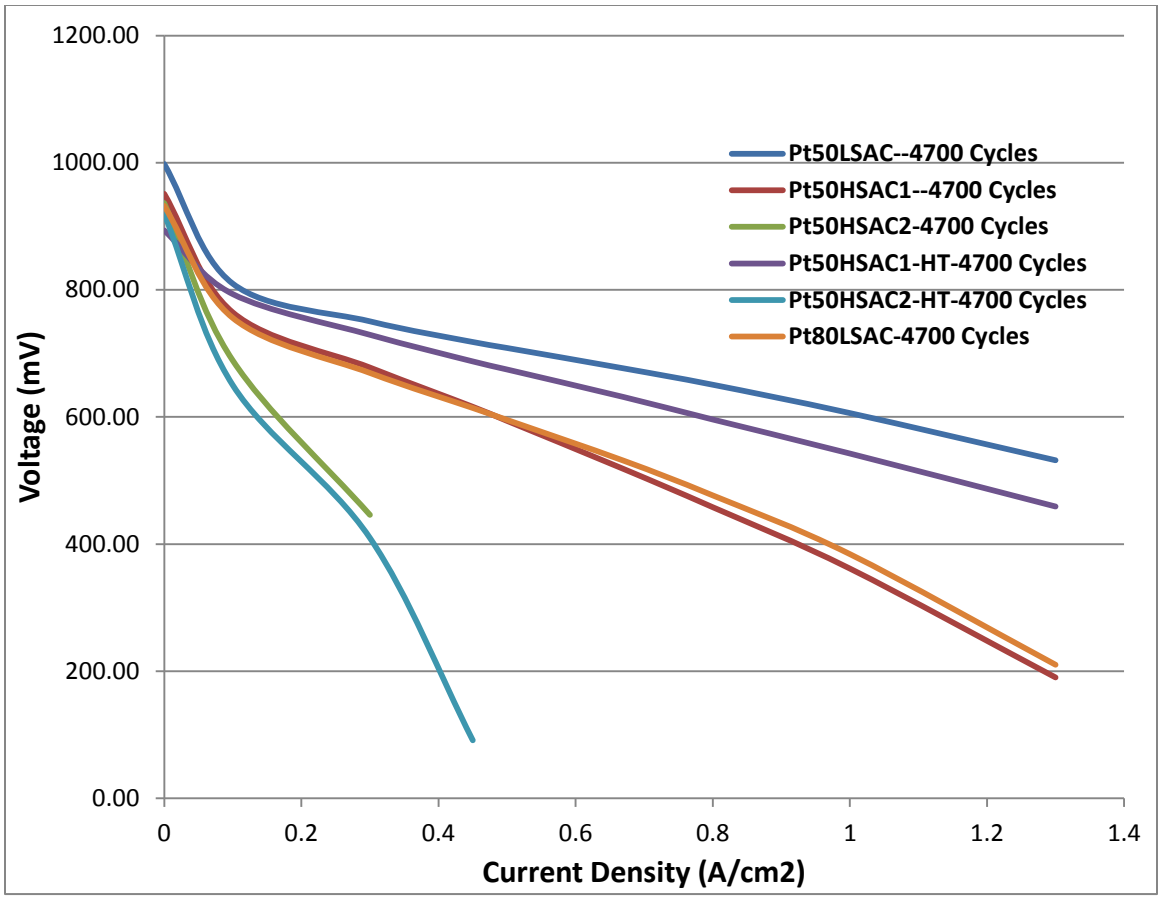

Figure 49. Polarization data for the MEAs after 4700 cycles. Pt50HSAC2 and Pt50HSAC2-HT are considered to have failed as they were unable to achieve a current density of 0.6A/cm^2. Data obtained at Ballard Power Systems, Inc.

After 4700 cycles, the performance attained by the different MEAs is very distinct. Pt50HSAC2 and Pt50HSAC2-HT could not produce a current density of 0.6A/cm2 after 4700 cycles and were said to have failed. Of the functioning cells, Pt50LSAC had the highest performance, followed closely by Pt50HSAC1-HT. These results are in good agreement with the data presented in Chapter 5. Pt50HSAC1 and Pt80LSAC showed very similar performance after the cycling protocol, but were significantly lower than the Pt50LSAC and Pt50HSAC1-HT. While the reduced performance of Pt50HSAC1 was expected, the poor results shown for Pt80LSAC were not. Pt80LSAC showed inferior performance to Pt50LSAC at both the beginning of life and after 4700 cycles, with the gap between them being significantly larger at the end of the experiment. This would

indicate that increased Pt loadings are not necessarily beneficial for fuel cell performance.

The effect of changing the UPL of the AST protocol can be seen in Figure 50. As can be seen in the figure, very little difference is seen by changing the UPL from 1.2V to 1V; both of these potentials are lower than the theoretical potential of ORR. Though the polarization curve for the 1V UPL AST is slightly below that of 1.2V UPL AST, these results are within expected error, and should be considered equal.

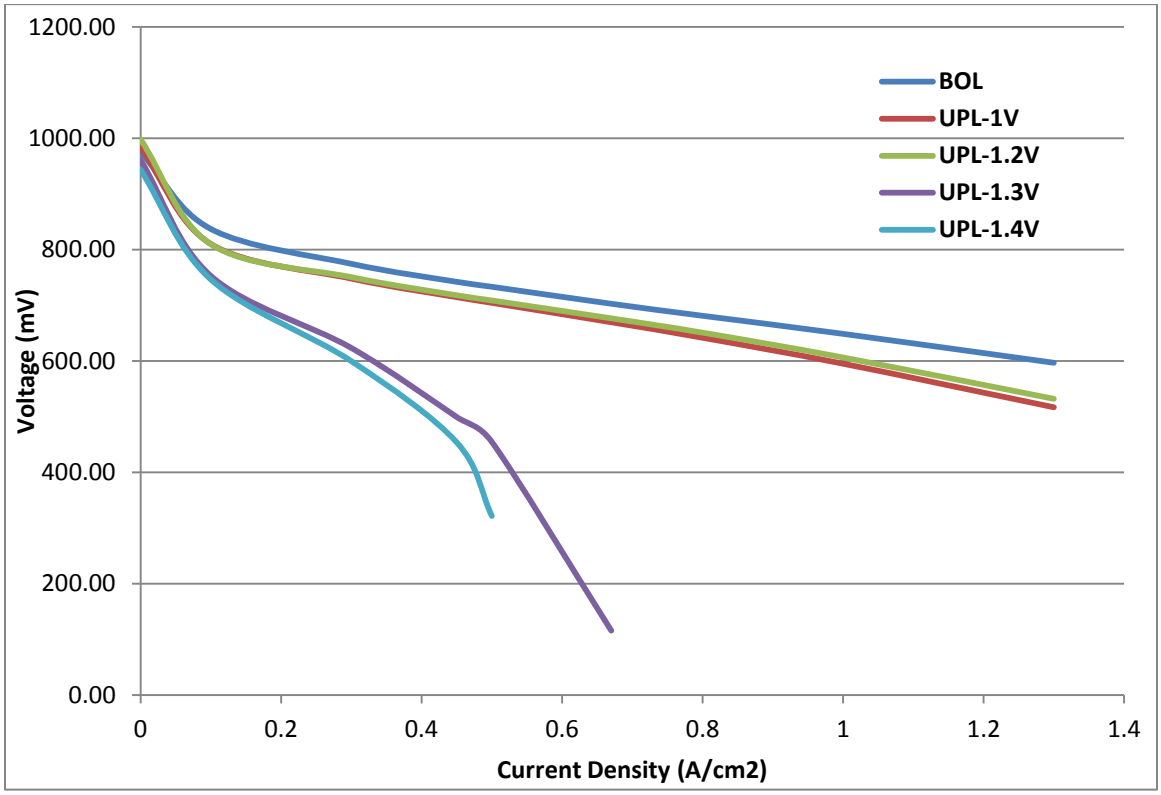

Figure 50. Polarization curves for MEAs that have been cycled to different upper potential limits. As was expected, holding the cells at potentials higher than 1.2V resulted in severe degradation. Data obtained at Ballard Power Systems, Inc.

Cycling the cell to 1.4V led to a severe corrosion, as was expected. It should be noted that the 1.4V UPL AST was stopped after 700 cycles, at which point it was considered to have failed as well.

7.2.2 XPS Results

XPS analysis was done for non-run, conditioned, and aged samples, and the results can be seen in Tables X and XI, below.

Table X. Carbon 1s Speciation Changes for Sample CCMs

		C gr	C-C	C*	C-OH/ C-OC	C=O/C-F	COOH	C-F	CF_2-CH_2/ OCF
Sample Identifier		*284.3*	*285.1*	*286.1*	*286.9*	*288*	*289.3*	*290.3*	*291.1*
Pt50LSAC	Non-Run	40.1	8.3	5.5	2.9	3.1	2.8	2.7	34.5
Pt50HSAC1		42.2	10.6	6.4	3	4	2.8	2.9	28.2
Pt50HSAC2		47	12.8	6.1	3.6	4.3	3.1	3	20.1
Pt50HSAC1-HT		45.2	13.8	6.1	3.2	3.3	2.9	2.8	22.7
Pt50HSAC2-HT		47.1	13.3	6.4	3.9	3.9	3.2	2.9	19.3
Pt80LSAC		29.1	5.5	4.3	1.9	2.3	3	3.7	50.2
Pt50LSAC	Cond.	42.1	9.1	5.9	2.9	2.8	2.8	2.6	31.9
Pt50HSAC1		40	12.1	9.2	6.3	6.8	4	3.5	18.1
Pt50HSAC2		47.1	11.2	8.6	3.7	3.7	3.1	3.2	19.4
Pt50HSAC1-HT		48.2	10.9	8.1	4.1	3.5	2.7	3.3	19.2
Pt50HSAC2-HT		50.4	10.2	7.9	3.6	3.2	2.8	3.1	18.8
Pt80LSAC		35.6	7.1	5.6	2.8	2.4	2.4	3.1	41
Pt50LSAC	1.2V	52.4	9.5	5.5	3.2	3.4	3.1	3.3	19.6
Pt50HSAC1		40.7	8.9	6	3.2	3.6	3.3	4.3	30.1
Pt50HSAC2		35.8	8.4	4.7	2.4	3.6	9.8	20.6	14.6
Pt50HSAC1-HT		41.3	10.3	6.1	2.9	4	4	5.7	25.6
Pt50HSAC2-HT		34.9	8.1	6	2.8	3.8	5.3	20.1	18.9
Pt80LSAC		29.3	6.2	4.6	2.2	3.2	5.4	27.4	21.7

Table XI. Platinum 4f Speciation Changes for Sample CCMs

		Pt	Pt-C	PtO
Sample Identifier		*71.1*	*71.8*	*72.8*
Pt50LSAC	Non-Run	40.7	42.4	16.9
Pt50HSAC1		29.2	45.2	25.6
Pt50HSAC2		33	48.1	18.9
Pt50HSAC1-HT		47.6	43.6	8.7
Pt50HSAC2-HT		47.8	43.6	8.5
Pt80LSAC		58.7	29	12.3
Pt50LSAC	Conditioned	56.3	24.9	18.8
Pt50HSAC1		46.5	33.5	20
Pt50HSAC2		47	33.8	19.2
Pt50HSAC1-HT		49.7	32.1	18.3
Pt50HSAC2-HT		53	28.5	18.5
Pt80LSAC		55.4	27.8	16.8
Pt50LSAC	1.2V AST	60.3	27.9	11.8
Pt50HSAC1		62.4	24.4	13.2
Pt50HSAC2		62.7	26.6	10.7
Pt50HSAC1-HT		59.6	29.6	10.8
Pt50HSAC2-HT		64.4	21.8	13.8
Pt80LSAC		66.2	21.4	12.4

From Table X it be seen that the HSAC samples lose graphite content over the course of the cycling protocol, while Pt50LSAC and Pt80LSAC showed an increase or no change at all. All of the samples, however, are characterized by higher carboxylate/carbonate content and C-F bonds than they were in their non-run state. For most samples there was also a large decrease in the CF_2-CH_2 generally associated with the ionomer content. The other major change is in the platinum speciation. The non-run samples were composed of roughly equal parts Pt metal and Pt-C species. After conditioning the Pt 4f speciation changed so that all of the catalysts were fairly similar with roughly 50%Pt metal, 30% Pt-

C, and 20% PtO. After the cycling protocol, the Pt-C and PtO species were significantly diminished, and platinum was mostly present in its metallic form.

The results for the CCMs tested at differing UPLs is shown in Table XII.

Table XII. C1s Speciation for Pt50LSAC CCMs Using Differing AST Upper Potential Limits

	C gr	C-C	C*	C-OH/C-OC	C=O/C-F	COOH	C-F	CF_2-CH_2/ OCF
	284.3	*285.1*	*286.1*	*286.9*	*288*	*289.3*	*290.3*	*291.1*
Non-Run	40.1	8.3	5.5	2.9	3.1	2.8	2.7	34.5
Conditioned	42.1	9.1	5.9	2.9	2.8	2.8	2.6	31.9
1.0V	52.4	9.5	5.5	3.2	3.4	3.1	3.3	19.6
1.2V	52.4	9.5	5.5	3.2	3.4	3.1	3.3	19.6
1.3V	38	7.4	4.6	2.8	4.1	7.1	21.3	14.7
1.4V	32.9	5.6	4.8	2.7	3.7	10.3	25.5	14.5

The C1s speciation obtained by cycling the cell to a maximum of 1V gave identical results to cycling the CCMs to 1.2V, however subjecting the cells to higher potentials resulted in drastically different compositions. At 1.3V and 1.4V, the graphite content in the samples dropped significantly, while the carbonate/carboxylate groups and carbon-fluorine bonds showed steep increases. Carbon-carbon single bonds and aliphatic carbons were reduced as well, as did CF_2-CH_2 content, suggesting oxidation of the ionomer.

Table XIII. Pt Speciation for Pt50LSAC After Different AST Upper Potential Limits

	Pt	Pt-C	PtO
	71.1	*71.8*	*72.8*
Non-Run	40.7	42.4	16.9
Conditioned	56.3	24.9	18.8
1.0V	57.8	29	13.2
1.2V	60.3	27.9	11.8
1.3V	62.4	22.6	15
1.4V	62.4	23.2	14.4

Like the results shown in Table XI, cycling Pt50LSAC resulted in significantly lower PtO and Pt-C content while the metal form of platinum increased overall. Though the carbon speciation for the 1V and 1.2V AST protocols were identical, differences exist in the platinum speciation.

7.2.3 Digital Image Processing and Principal Component Analysis

SEM images were acquired for the CCMs tested, and changes to their morphology are readily apparent.

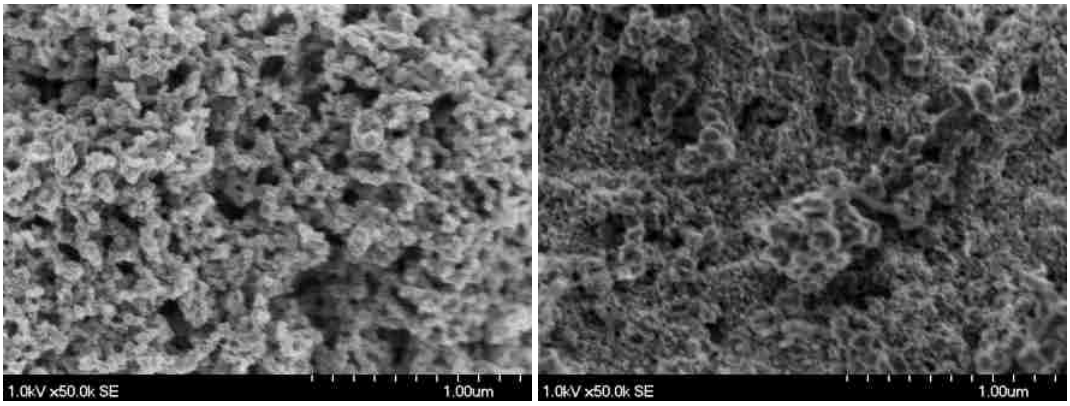

Figure 51. SEM images for Pt50LSAC showing the conditioned CCM (left) and degraded CCM (right)

The images were acquired in a random order, and information regarding the sample and AST protocols used were not provided until images had been acquired for all samples. Careful consideration was taken to ensure that the magnification, voltage, brightness, and contrast were at consistent values for all images. From Figure 51, it is clearly visible that the structure of material has changed drastically following the cycling protocol. The degraded sample no longer shows individual carbon black particles that are clearly visible in the conditioned CCM image. Digitial image processing was done to quantify these changes, and the results can be seen in Figure 52.

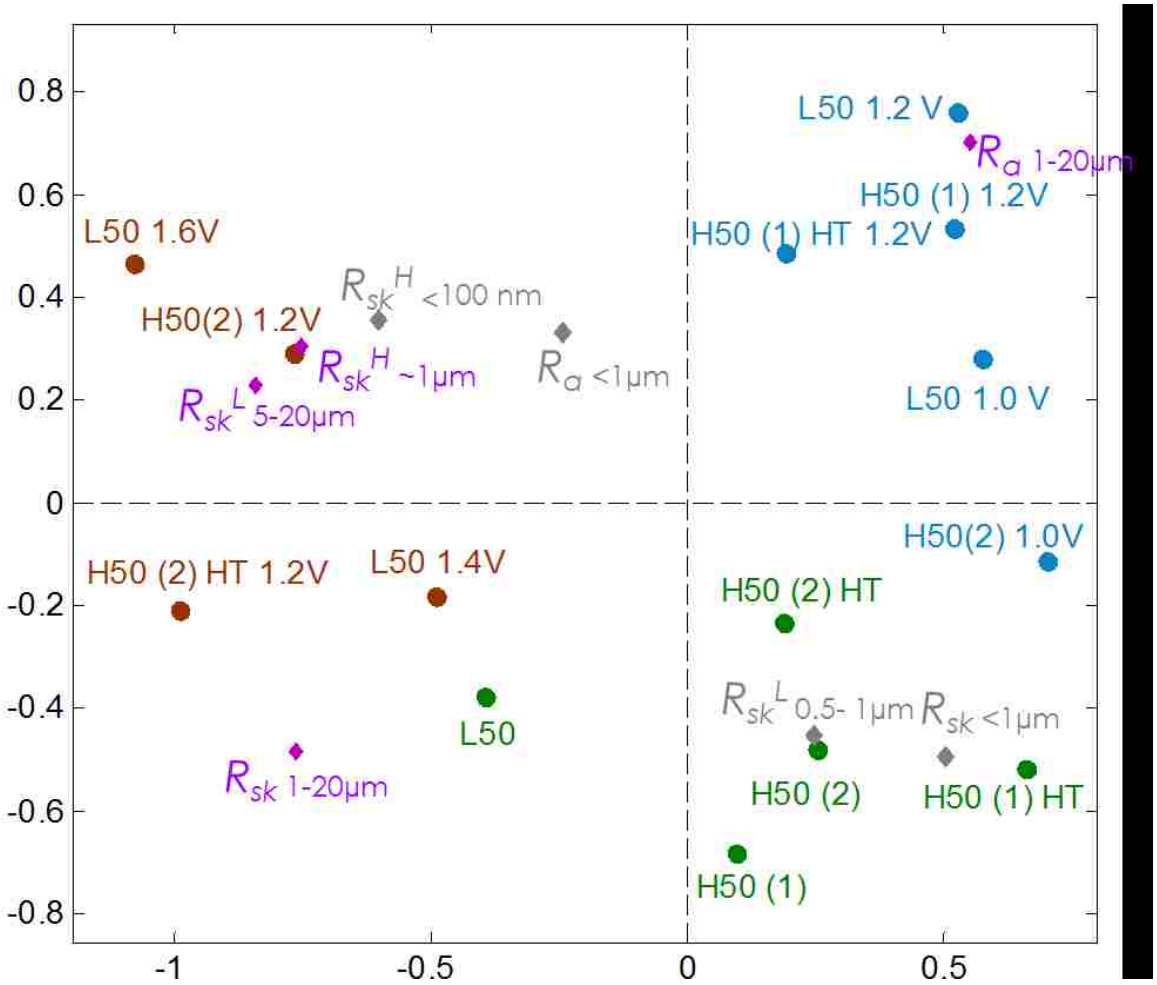

Figure 52. PCA biplot for the morphology statistics gathered from SEM images of the CCM samples. Conditioned samples are shown in green, functioning cycled CCMs in blue, while degraded samples are in red.

Figure 52 shows how the morphology parameters correlate with the conditioned CCMs, in green, and the degraded CCMs in red, and functioning AST cycled CCMs in blue. There is a distinct split between the three groups of CCMs, and these groups are each defined by specific physical characteristics. Because images were acquired at 2 different magnifications, the high frequency and low components of roughness and skewness represent two length scales with the high frequency components at 2.5K being approximately the same length as the low frequency components at 50K magnification. From the biplot, the conditioned samples are highly correlated with microporosity on the 0.5-1µm length scale, while the heavily degraded samples are described by mesoporosity

(5-20μm), microporosity, and nanoporosity (~100nm). Finally the cycled CCMs are correlated with surface roughness on the mesoscale, while the corroded samples are characterized by roughness on the microscale. The trend for the CCMs appears to be a loss of microporosity, but increasing nano- and mesoscale porosity instead. Roughness on the mesoscale also decreases due to cycling, while microscale roughness tends to increase.

7.3 Conclusions

By using an accelerated stress testing protocol, it was found that significant chemical and morphological changes accompany large losses in FC performance. Using an upper potential limit of 1.2V resulted in reduction in graphite and CF_2 content while simultaneously increasing carboxylate and C-F bond content, in addition to increasing platinum metal content, but severely reducing Pt-C and PtO species. Cycling cells to potentials above 1.2V amplified these results, requiring fewer cycles before similar changes could be observed. Finally by analyzing SEM images of the samples, it was found that porosity on the meso-, micro-, and nanoscale all increased due to potential cycling, while sample roughness shifted from the meso to microscale. Future work will be done to correlate the chemical changes observed by XPS to the physical changes seen through SEM.

8. Comparison of Performance Losses Obtained Through RDE and Fuel Cell Testing

The final portion of the project was done in order to compare results of AST protocols when performed using RDE and CCMs. Though durability testing using RDE is gaining in popularity, there has yet to be a published article comparing those results to data obtained by corroding catalysts in a cell. Five catalysts were used in this experiment, Pt50LSACC, Pt50MSAC, Pt50HSAC1, Pt50HSAC2, and Pt50Vulcan, and they were tested using both methods. Due to limitations imposed the mass of catalyst used for the RDE experiments, this portion of the project was largely focused on electrochemical results obtained by the two methods as opposed to changes in the physical properties of the catalysts.

8.1 Materials and Methods

8.1.1 Rotating Disk Electrode

Catalyst samples were weighed and added to a solution of 80/20 DI water/isopropyl alcohol and a 0.5% Nafion in DI water. The mixture was then sonicated to form a homogenous 4 mg/ml ink with 30 µl of the Nafion solution per milliliter of total solution. Because the goal was to compare performance data obtained from RDE and CCM testing, equivalent Pt-loadings (0.4mgPt/cm^2) were tested. To do this, 39.2 µl of the catalyst ink, added as 10µl increments, were pipetted on to a rotating disk electrode, and was then dried for 30 minutes at 55^{o}C.

The electrode was rotated at 2000 RPM at 20^{o}C, and was used as part of a 3-electrode setup, with a saturated calomel electrode (0.242V vs. RHE) as the reference electrode and platinum wire as the counter electrode. 0.1M perchloric acid as the electrolyte, the electrode was cycled between 0 and 1.2 V (vs. RHE) 30 times at a rate of

100 mV/s while nitrogen bubbled through the electrolyte. This step was done to ensure a clean, uncontaminated surface. After the cleaning sweeps, oxygen gas was bubbled through the cell, and the electrode was cycled 4 times between 0 and 1.2 V (vs. RHE) at a rate of 5mV/s with oxygen bubbling through the cell. This represented the BOL performance of the catalyst, and was used as the baseline for all aged catalyst voltammograms. After acquiring the BOL voltammograms, the RDE was held at 0.6V (vs RHE) for 30s, followed by holding at 1.2V (vs. RHE) for 60s. These two voltages represent one cycle. The RDE was cycled 100, 500, 750, 1500, 2000, 3000, and 4700 times, with voltammograms acquired after each set interval. The liquid electrolyte was replaced every 500 cycles in order to prevent contaminants from accruing in the media.

8.1.2 Membrane Electrode Assembly Testing

Catalyst coated membranes were produced offsite at Ballard Power Systems, Inc., and were shipped to UNM. The anode side of the membrane was coated with Pt50LSAC to achieve a loading of 0.1mgPt/cm^2, while the cathode had a loading of 0.4mgPt/cm^2 achieved by using one of the 5 experimental catalysts. GDL materials were cut to 1.1cm^2 rectangles using specially manufactured dies, and 0.005" PTFE sheeting was cut for use as a gasket material. Individual CCMs were placed between the GDL and gaskets, and the cell was compressed by applying 25in-lb of torque to the bolts holding the assembly together.

For standard operation, the cell is heated to 75^{o}C, and fed gases at 100%RH. The anode side of the cell was fed 1500sccm of H_2, and the cathode was fed 2500sccm of air (21% O_2, balance N_2, and both electrodes operated at 5psig back pressure. Assembled PEMFCs were conditioned overnight in order to insure proper membrane hydration. To

condition the cell, the system was held at 0.45V (vs. RHE) overnight at the standard operating conditions. After successfully conditioning the cell, a polarization curve is obtained by polarizing the cell from 0.4V to OCV in 50mV steps and holding at each potential for 120seconds. It is important to note that the anode portion of the cell acts as a reversible hydrogen electrode, and is used as both the anode and reference electrode for the system.

When degrading the cell using the AST protocol, the system is held at 80^{o}C, but all other conditions remain identical. As with the RDE experiment, the cell is held at 0.6V for 30s and 1.2V for 60s. The fuel cell is cycled 100, 500, 750, 1500, 2000, 3000, and 4700 times, with polarization curves taken at the standard operating conditions being performed after each cycling period.

8.1.3 XPS Analysis

BOL and aged materials were analyzed using XPS in order to quantify what chemical changes occurred during the cycling protocol. X-ray photoelectron spectroscopy (XPS) was performed using Kratos Axis Ultra spectrometer using an Al Ka X-ray source, with emission voltage of 10 kV and emission current of 15 mA. Both low resolution survey spectra and high resolution C 1s and Pt 4f spectra were acquired. All XPS spectra were charge referenced to graphite carbon at 285.4eV.

8.2 Results and Discussion

8.2.1 CCM Testing

Figure 53 shows the BOL polarization curves obtained by testing the five catalysts in the 1.1cm^2 cell. As can be seen in the figure, Pt50HSAC2 has the highest initial performance, achieving a current density of 2.71A/cm2 at 0.4V, while Pt50MSAC has the lowest

performance, reaching 1.75A/cm^2 at the same voltage. Pt50HSAC1 and Pt50Vulcan show similar performance throughout the voltage range, and Pt50LSAC shows slightly lower performance in comparison.

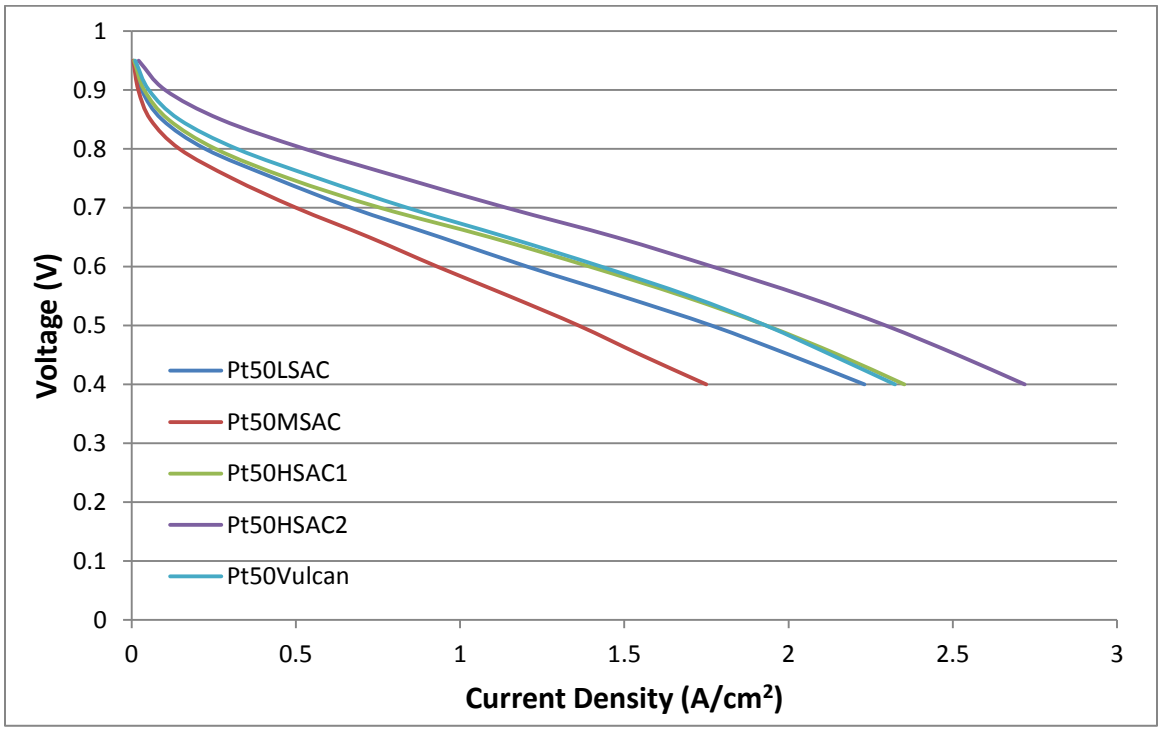

Figure 53. BOL Polarization curves for Pt50LSAC, Pt50MSAC, Pt50HSAC1, Pt50HSAC2, and Pt50Vulcan. Pt50HSAC2 has the highest BOL performance for all catalysts while Pt50MSAC has the lowest.

After cycling the CCMs 4700 times using the AST protocol, the following results were obtained.

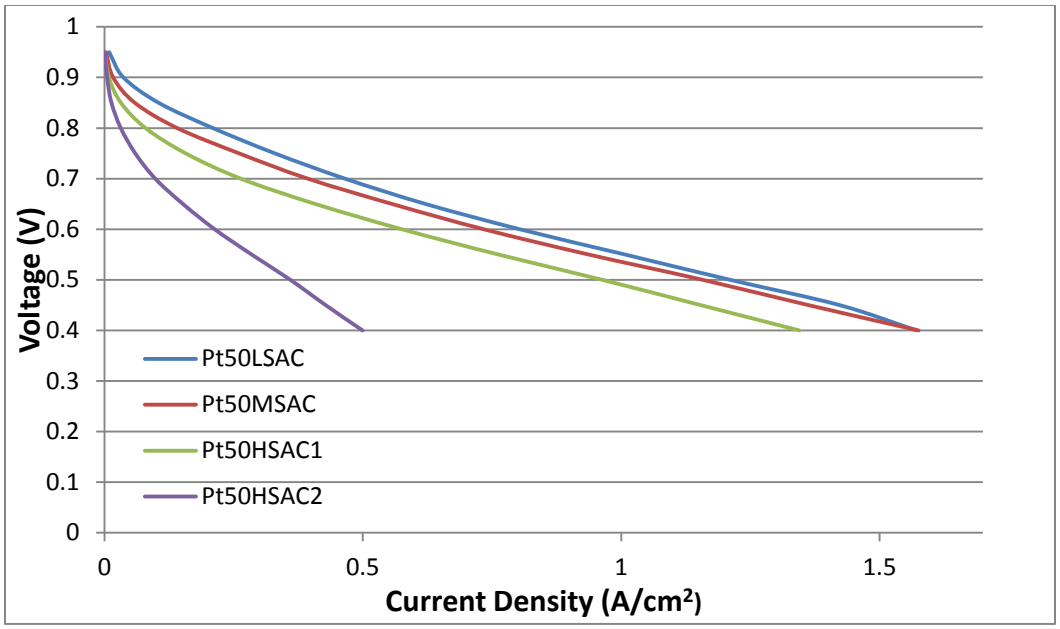

Figure 54. Polarization curves obtained after cycling the CCMs 4700 times between 0.6V (30s) and 1.2V (60s). Pt50Vulcan is not included because the sample failed to achieve an OCV of 0.6V after 4200cycles.

Figure 54 shows that after cycling, the results obtained at the beginning of life are somewhat reversed. Pt50LSAC showed the highest level of performance following the cycling protocol, while Pt50HSAC2 and Pt50Vulcan showed the worst. Pt50Vulcan is not shown in the figure because after 4200 cycles the membrane could not achieve a current density of 0.6A/cm^2, indicating that the cell had failed.

Table XIV, below, details how the current density (A/cm^2) produced by the CCMs at 0.4V, 0.65V, and 0.85V changed after a set number of cycles. From the data, it can be seen that though Pt50LSAC delivered the highest current densities after 4700 cycles, Pt50MSAC showed the smallest overall performance losses. Pt50HSAC1 and Pt50HSAC2 had, and largest drops of functioning CCMs. It should also be noted that Pt50MSAC delivered higher current densities after 100, 500, and 750 cycles than it did at the beginning of life. This suggests that potentially beneficially changes occurred during those cycling periods, and further investigation is necessary.

Table XIV. Current Densities (A/cm^2) at Set Voltages after Predetermined Number of Cycles

	Pt50LSAC			Pt50MSAC			Pt50HSAC1			Pt50HSAC2			Pt50Vulcan		
Voltage	*0.4*	*0.65*	*0.85*	*0.4*	*0.65*	*0.85*	*0.4*	*0.65*	*0.85*	*0.4*	*0.65*	*0.85*	*0.4*	*0.65*	*0.85*
BOL	2.23	0.94	0.09	1.75	0.72	0.06	2.35	1.09	0.11	2.72	1.48	0.27	2.32	1.14	0.15
100	2.06	0.89	0.09	1.83	0.71	0.05	2.32	1.01	0.09	2.63	1.33	0.17	2.14	1.01	0.11
500	1.89	0.78	0.08	2.00	0.77	0.05	2.29	0.98	0.08	1.84	0.83	0.09	2.01	0.92	0.10
750	1.90	0.79	0.21	2.02	0.78	0.06	2.24	1.00	0.09	1.90	0.88	0.11	1.94	0.87	0.09
1500	1.79	0.72	0.08	1.43	0.46	0.04	2.10	0.87	0.07	1.71	0.86	0.09	1.60	0.61	0.06
2000	1.71	0.68	0.19	1.30	0.40	0.03	1.98	0.80	0.07	1.50	0.73	0.07	1.36	0.46	0.05
3000	1.70	0.63	0.18	1.68	0.59	0.06	1.81	0.66	0.06	1.03	0.42	0.04	0.96	0.30	0.07
4700	1.53	0.54	0.15	1.58	0.56	0.06	1.35	0.41	0.03	0.50	0.15	0.01	--	--	--
% Diff	-31%	-42%	65%	-10%	-23%	2%	-43%	-63%	-72%	-82%	-90%	-95%			

Though the membranes do show changes to their performance after as a little as 100 cycles, the rate of performance losses is not uniform, as seen in Figure 47.

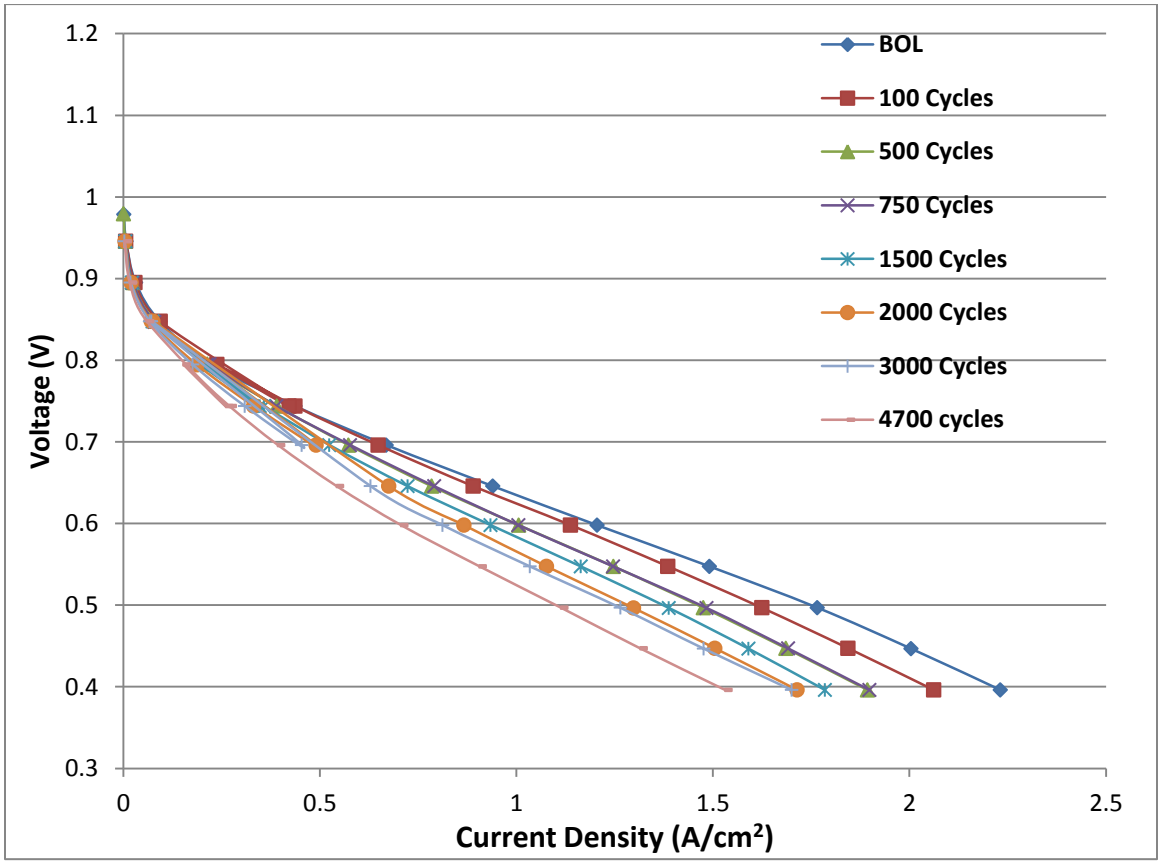

Figure 55. Polarization curves for Pt50LSAC taken periodically during the cycling protocol. Performance losses do not occur continuously during the cycling protocol, indicating that cell corrosion may not occur at a uniform rate.

The polarization data for Pt50LSAC shows that between 500 and 750 cycles and between 2000 and 3000 cycles, no real changes to the performance occur. Whether this is related to the improved performance seen in Pt50MSAC is unclear, but it does appear that the performance losses due to AST cycling are not continuous, and may only proceed once some sort of threshold is breached. Additional work is necessary to determine what changes have occurred at these intervals.

8.2.2 RDE Results

The beginning of life, capacitance corrected voltammograms for the catalysts are shown in Figure 56.

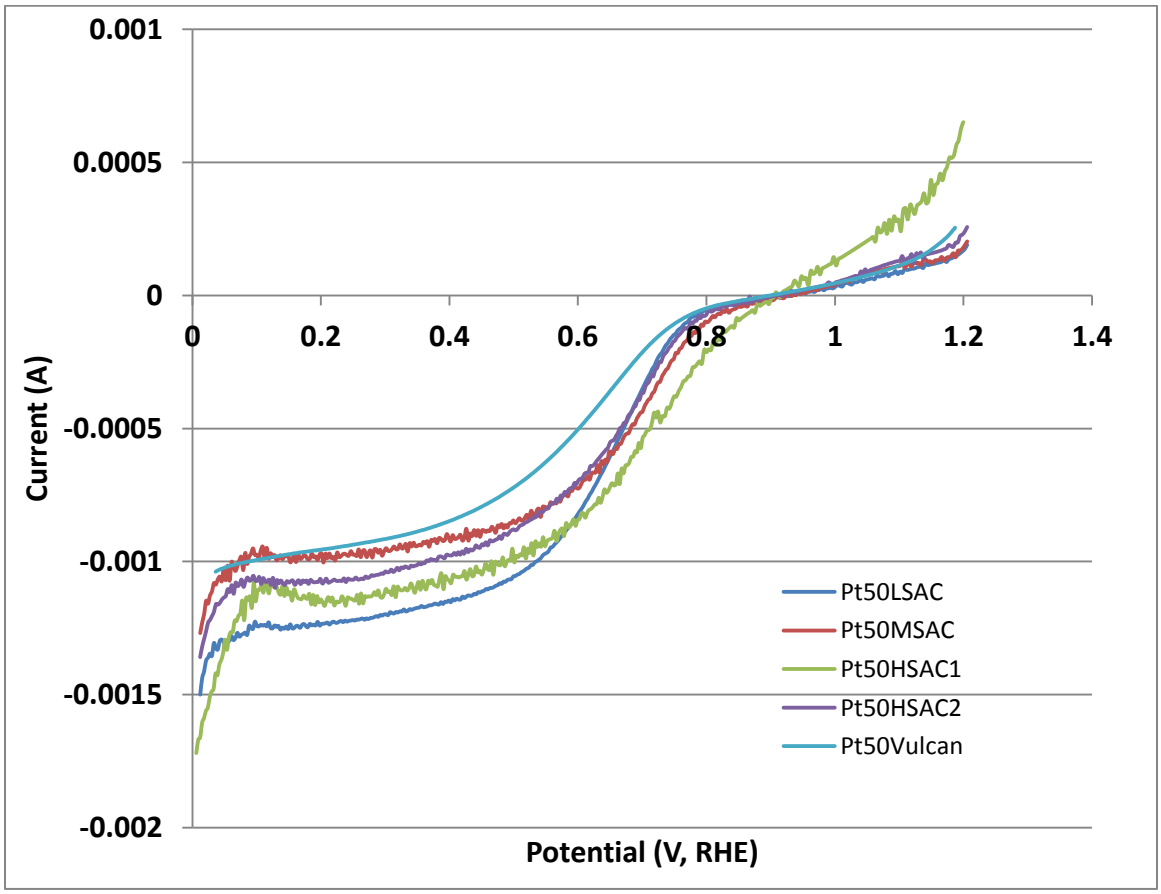

Figure 56. BOL voltammograms for the five catalyst samples. Unlike the BOL polarization curves, the voltammograms are fairly similar making it difficult to say which catalyst is the best performing.

Unlike the BOL polarization curves, the results obtained through the RDE are fairly similar. Overall, the samples achieve limiting currents between 1-1.5mA, and they each of approximately the same open circuit voltage of 0.9V (vs. RHE). These results, however, are distinctly different from those obtained at the end of life, as seen in Figure 57.

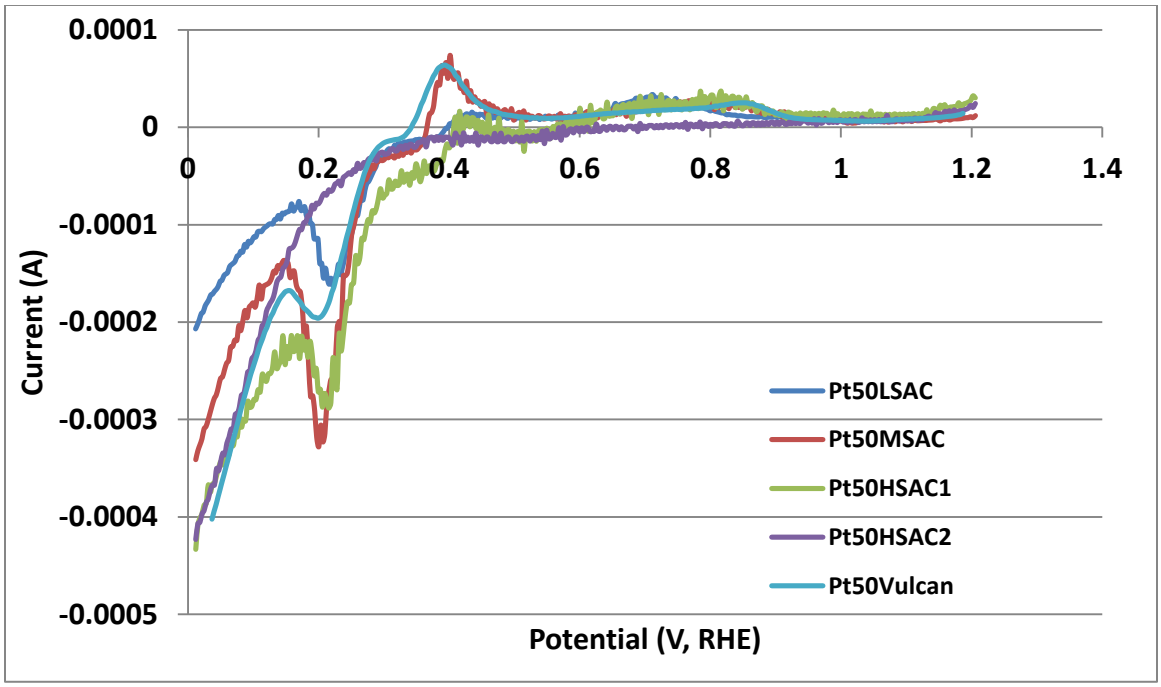

Figure 57. Voltammograms obtained after 4700 cycles. Unlike the CCM testing, data was collected for all five samples.

The results obtained after 4700 cycles are the reverse of those obtained from the CCM testing; the samples that saw the smallest changes was Pt50Vulcan, while Pt50LSAC showed the largest drop in limiting current. Table XI details the results below.

Table XV. Comparison of Limiting Currents from BOL to 4700 Cycles Obtained by RDE

Sample	Limiting Current (A)	Limiting Current (mA)	Change
Pt50LSAC	-1.52	-0.21	-86%
Pt50MSAC	-1.31	-0.34	-74%
Pt50HSAC1	-1.73	-0.45	-74%
Pt50HSAC2	-1.38	-0.42	-69%
Pt50Vulcan	-1.09	-0.47	-57%

The performance data acquired for each sample over the course of the cycling protocol, however, does show some similarities to those obtained through CCM testing.

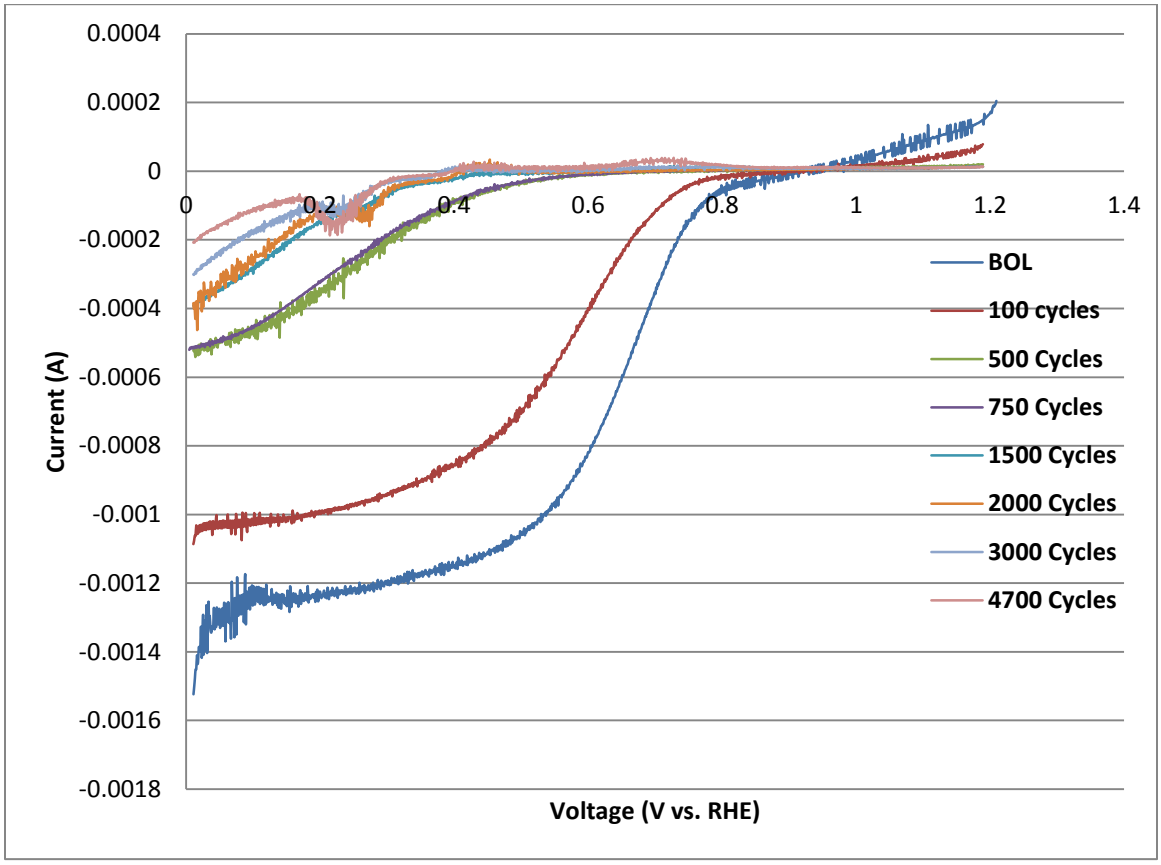

Figure 58. Capacitance corrected voltammograms of Pt50LSAC obtained at set interval for the RDE durability testing protocol. Like the gathered from CCM testing, the catalyst performance does not change continuously, and results gathered after some intervals are indistinguishable.

Like the CCM tests, the RDE durability results indicate that performance losses are not continuous over the cycling protocol. As seen in Figure 58, above, the performance data gathered after 500 and 750 cycles is essentially the same. It can also be said that the results obtained after 1500 and 2000 cycles are very similar, but this may be due factors other than the corrosion process. The RDE catalysts also experience greater performance losses earlier in the cycling protocol than the CCMs. It is clearly seen in Figure 58 that after only 500 cycles, Pt50LSAC exhibits a roughly 50% drop in its limiting current, greater than the equivalent losses recorded after 4700 cycles obtained from the CCM

testing. In addition, the kinetic region of the voltammograms spans roughly 800mV, far larger the BOL data which indicated a kinetic region roughly 400mV.

Though it is difficult to see, the results obtained from 2000 cycles onward no longer have the characteristic "S" shape of the BOL voltammograms. In reality, by removing the capacitance current from the results shown in Figure 58, additional information about the catalysts has been removed. Figure 59 shows an unprocessed voltammograms for Pt50LSAC at the beginning of life and after 4700 cycles.

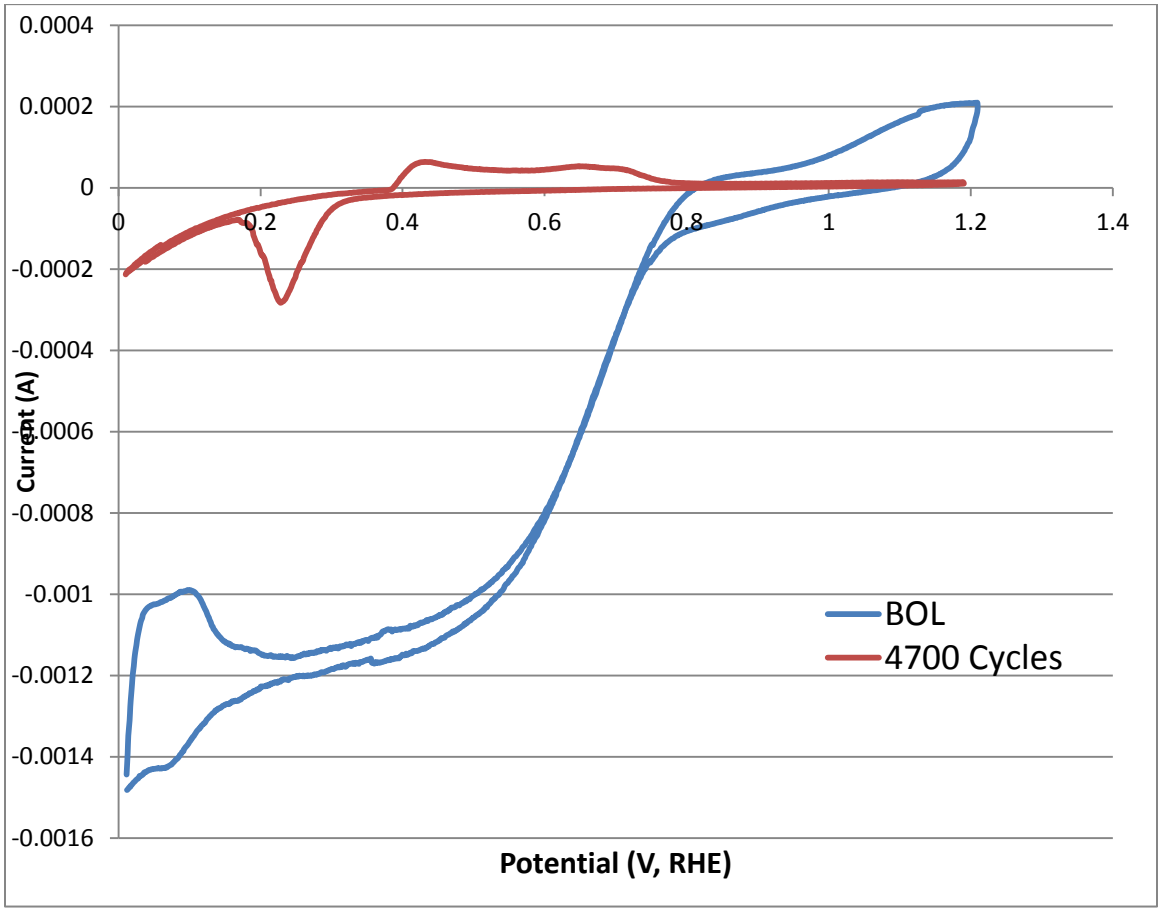

Figure 59. Voltammograms for Pt50LSAC obtained at the beginning of life (blue) and after 4700 cycles (red). In addition to showing reduced currents at all potentials, additional peaks appear in the 4700 cycle CV indicating the presence of other redox couples.

It is clearly visible from the figure that the behavior of the catalyst has changed quite drastically after 4700 cycles. While BOL voltammogram shows the kinetic, ohmic, and

mass-transport regions, the aged catalyst does not, and is characterized by additional peaks indicating the presence of previously absent redox couples. The voltammograms also shows similarities to those obtained when investigating the undecorated LSAC support, shown in Figure 60.

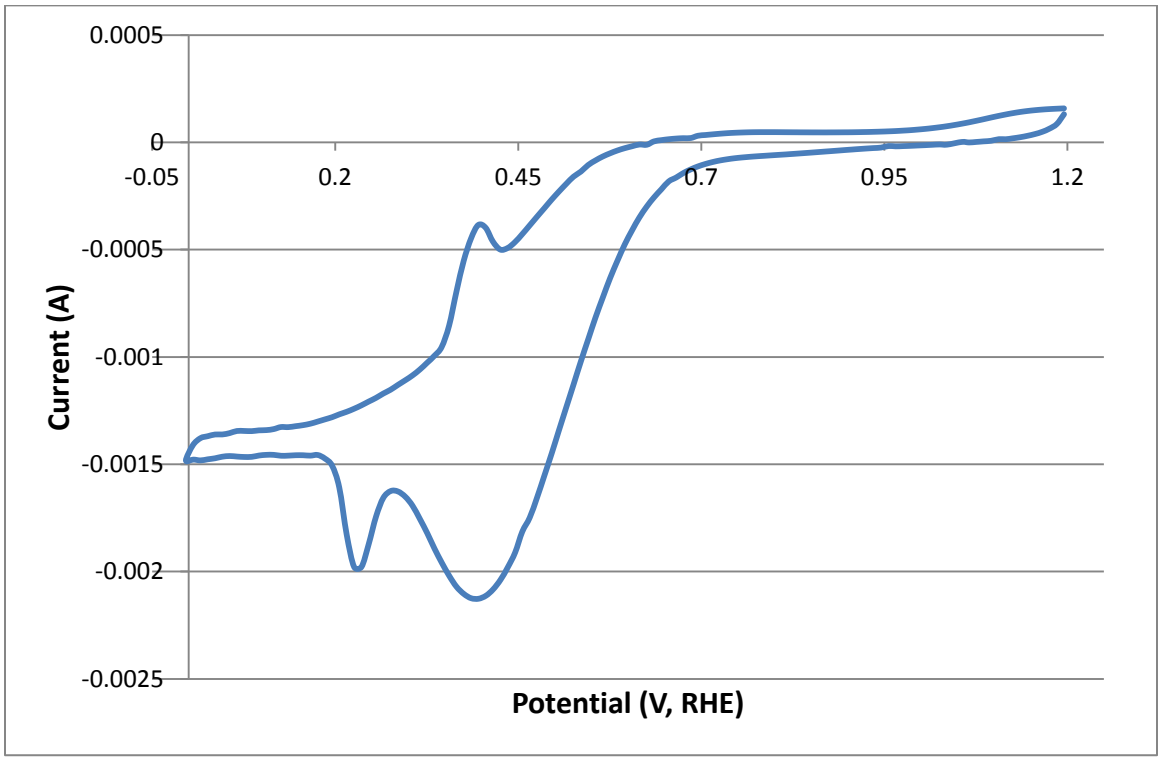

Figure 60. CV of LSAC (undecorated) for comparison to the results obtained for the aged Pt50LSAC catalyst.

It is possible that during the course of the aging protocol, much of the platinum has been stripped from the catalyst. Both the undecorated LSAC and aged Pt50LSAC display a reduction peak at approximately 0.2V, but the decorated carbon also shows a redox couple at 0.4V, which is not present in the CV for the aged catalyst. In order to accurately determine what changes have occurred to the RDE aged samples, characterization data must be acquired.

8.3 Conclusions

Based on the collected data, rotating disk electrodes do not accurately predict the rate or degree of performance losses that can be expected for PEMFC cathode catalysts. Despite some similarities between the two, the results obtained by performing durability testing using a rotating disk electrode are significantly different than those obtained using a small-scale cell. The rotating disk electrode results suggested that Pt50Vulcan and Pt50HSAC2 would be the most stable in the PEMFC environment, and Pt50LSAC would be the least, but CCM testing proved the exact opposite. The rotating disk electrode catalysts also suffered greater performance losses over 500 cycles of the AST protocol than the CCMs did over 4700. It is important to note that this is a single experiment comparing RDE to MEA durability testing. The experimental conditions used for the RDE tests were essentially identical to those used for the work described in Chapter 6, and it is possible that altering these conditions could improve the results. Overall, it appears that durability results obtained via RDE are not consistent with those obtained by MEA testing. Additional work is necessary in order to validate the results presented here; altering the experimental conditions could bring to the results to closer agreement while a lack of improvement would indicate that RDEs are inappropriate tools for durability testing.

9. Conclusions

It was found that lower surface area catalysts suffered lower performance losses than higher surface area catalysts, as is consistent with the literature. It was determined undispersed catalysts (catalysts that have not been coated onto a membrane) with high roughness and high microporosity were more stable than more homogenous and mesoporous samples. Microporosity was also found to be associated with surface oxygen content while roughness was found to be correlated with surface graphite. Mesoporosity and homogeneity were correlated with C-C single bonds and carbonate/carboxylate species. The location and crystallinity of a carbon support was also found to be important, with longer, surface graphite providing more stability than shorter, more dispersed graphite sheets. Finally, it was shown that undispersed catalysts that had high platinum carbide and platinum oxide content were more stable than those with predominately platinum metal, though the exact reasoning was unknown.

By using an accelerated stress testing protocol, it was found that significant chemical and morphological changes accompany large losses in FC performance. Using an upper potential limit of 1.2V resulted in reduction in graphite and CF_2 content while simultaneously increasing carboxylate and C-F bond content, in addition to increasing platinum metal content, but severely reducing Pt-C and PtO species. The loss of PtO and Pt-C correlating to performance losses is in good agreement with the preliminary results obtained from the undispersed catalysts. Cycling cells to potentials above 1.2V amplified chemical and physical changes, requiring fewer cycles before similar changes could be observed. Through the AST protocols it was found that porosity on the meso-, micro-, and nanoscale all increased due to potential cycling, while sample roughness shifted from the meso to microscale.

Finally, based on the collected data, it is believed that rotating disk electrodes do not accurately predict the rate or degree of performance losses that can be expected for PEMFC cathode catalysts. Despite both methods showing that performance losses appear to proceed at fluctuating rates over the course a cycling protocol, the results obtained by performing durability testing using a rotating disk electrode are significantly different than those obtained using a small-scale cell. On a purely electrochemical basis, the results obtained through the RDE testing were exactly the opposite of the MEA testing, and were in can counter to the performance data gathered over the course of this project. The rotating disk electrode catalysts also suffered greater performance losses over 500 cycles of the AST protocol than the CCMs did over 4700. To suggest the entire body of research obtained from RDE durability is unreliable would be inappropriate, however, as the lack of similarities between the two data sets may be due to the testing and experimental protocols. Further testing in this field is required before a definitive assessment can be made.

10. Future Outlook

Future work in this field will need to determine what changes are occurring to the cathode catalysts during an AST protocol as they occur. Currently, fuel cell testing focuses predominately on pre- and post-mortem analysis, but by stopping the AST protocol at predetermined intervals, it should be possible to draw more accurate correlations regarding the perceived chemical, morphological, and performance changes. Secondly, it is necessary to expand upon the RDE durability testing; though this work was not focused on the effect of the ionomer content, it is a highly important parameter that needs to be accounted for. It is likely that the degree of ionomer swelling in the MEA is less than the swelling seen in RDEs, but this is currently unproven. Additionally, other electrolytes, rotational speeds, and temperatures may have effects on the results obtained after cycling with an AST protocol. Other AST protocols need to be investigated looking at different temperature and relative humidity ranges; these are factors which are known to affect a PEMFC's performance, and but understanding how cells change chemically and structurally over time is highly important. Finally, though it is currently the focus of many research projects, durability testing of PGM alloys and non-PGM catalysts is extremely important to the field as a whole. Reduction of platinum content in PEMFCs is paramount to their commercialization, but this requires understanding how alternative catalysts degrade over time.

Bibliography

1. K. A. Starz, E. Auer, T. Lehmann and R. Zuber, Journal of Power Sources **84** (2), 167-172 (1999).
2. K. S. Dhathathreyan, P. Sridhar, G. Sasikumar, K. K. Ghosh, G. Velayutham, N. Rajalakshmi, C. K. Subramaniam, M. Raja and K. Ramya, International Journal of Hydrogen Energy **24** (11), 1107-1115 (1999).
3. R. Borup, J. Meyers, B. Pivovar, Y. S. Kim, R. Mukundan, N. Garland, D. Myers, M. Wilson, F. Garzon, D. Wood, P. Zelenay, K. More, K. Stroh, T. Zawodzinski, J. Boncella, J. E. McGrath, M. Inaba, K. Miyatake, M. Hori, K. Ota, Z. Ogumi, S. Miyata, A. Nishikata, Z. Siroma, Y. Uchimoto, K. Yasuda, K.-i. Kimijima and N. Iwashita, Chemical Reviews **107** (10), 3904-3951 (2007).
4. P. Costamagna and S. Srinivasan, Journal of Power Sources **102** (1-2), 253-269 (2001).
5. R. M. Darling and J. P. Meyers, Journal of The Electrochemical Society **150** (11), A1523-A1527 (2003).
6. K. C. Neyerlin, H. A. Gasteiger, C. K. Mittelsteadt, J. Jorne and W. Gu, Journal of The Electrochemical Society **152** (6), A1073-A1080 (2005).
7. J. X. Wang, N. M. Markovic and R. R. Adzic, The Journal of Physical Chemistry B **108** (13), 4127-4133 (2004).
8. P. T. Yu, W. Gu, R. Makharia, F. T. Wagner and H. A. Gasteiger, ECS Transactions **3** (1), 797-809 (2006).
9. H. Chizawa, Y. Ogami, H. Naka, A. Matsunaga, N. Aoki, T. Aoki and K. Tanaka, ECS Transactions **11** (1), 981-992 (2007).
10. U. A. Paulus, A. Wokaun, G. G. Scherer, T. J. Schmidt, V. Stamenkovic, V. Radmilovic, N. M. Markovic and P. N. Ross, The Journal of Physical Chemistry B **106** (16), 4181-4191 (2002).
11. K. C. Neyerlin, R. Srivastava, C. Yu and P. Strasser, Journal of Power Sources **186** (2), 261-267 (2009).
12. Y. Dai, L. Ou, W. Liang, F. Yang, Y. Liu and S. Chen, The Journal of Physical Chemistry C **115** (5), 2162-2168 (2011).
13. V. A. Sethuraman, J. W. Weidner, A. T. Haug, S. Motupally and L. V. Protsailo, Journal of The Electrochemical Society **155** (1), B50-B57 (2008).
14. T. Kawaguchi, W. Sugimoto, Y. Murakami and Y. Takasu, Journal of Catalysis **229** (1), 176-184 (2005).
15. P. J. Ferreira, G. J. la O, Y. Shao-Horn, D. Morgan, R. Makharia, S. Kocha and H. A. Gasteiger, Journal of The Electrochemical Society **152** (11), A2256-A2271 (2005).
16. K. J. Blackmore, E. Bauer, L. Elbaz, E. L. Brosha, T. M. McCleskey and A. K. Burrell, ECS Transactions **30** (1), 83-90 (2011).
17. M. L. Perry, T. Patterson and C. Reiser, ECS Transactions **3** (1), 783-795 (2006).
18. A. P. Young, J. Stumper and E. Gyenge, Journal of The Electrochemical Society **156** (8), B913-B922 (2009).
19. W. R. R. Baumgartner, E. Wallnofer, T. Schaffer, V. Hacker, V. Peinecke and P. Prenninger, ECS Transactions **3** (1), 811-825 (2006).
20. C. G. Chung, L. Kim, Y. W. Sung, J. Lee and J. S. Chung, International Journal of Hydrogen Energy **34** (21), 8974-8981 (2009).
21. X. Yu and S. Ye, Journal of Power Sources **172** (1), 133-144 (2007).
22. X. Yu and S. Ye, Journal of Power Sources **172** (1), 145-154 (2007).
23. H. Zhong, H. Zhang, G. Liu, Y. Liang, J. Hu and B. Yi, Electrochemistry Communications **8** (5), 707-712 (2006).
24. A. Miura, M. E. Tague, J. M. Gregoire, X.-D. Wen, R. B. van Dover, H. c. D. Abruña and F. J. DiSalvo, Chemistry of Materials **22** (11), 3451-3456 (2010).
25. W. Gu, R. N. Carter, P. T. Yu and H. A. Gasteiger, ECS Transactions **11** (1), 963-973 (2007).
26. M. Knauer, M. E. Schuster, D. Su, R. Schlögl, R. Niessner and N. P. Ivleva, The Journal of Physical Chemistry A **113** (50), 13871-13880 (2009).
27. J. Li, P. He, K. Wang, M. Davis and S. Ye, ECS Transactions **3** (1), 743-751 (2006).
28. J. O. Muller, D. S. Su, U. Wild and R. Schlogl, Physical Chemistry Chemical Physics **9** (30), 4018-4025 (2007).
29. A. Ofstad, J. Davey, S. Sunde and R. L. Borup, ECS Transactions **16** (2), 1301-1311 (2008).

30. A. Patel, K. Artyushkova, P. Atanassov, A. P. Young, M. Dutta, Z. Ahmad, V. Colbow, S. Wessel and S. Ye, ECS Transactions **33** (1), 425-431 (2010).
31. S. Sharma and B. G. Pollet, Journal of Power Sources **208** (0), 96-119 (2012).
32. S. R. P. Silva and V. Stolojan, Thin Solid Films **488** (1-2), 283-290 (2005).
33. F. Xu, M. Wang, Q. Liu, H. Sun, S. Simonson, N. Ogbeifun, E. Stach and J. Xie, ECS Transactions **33** (1), 1281-1294 (2010).
34. J. Zhang, B. A. Litteer, W. Gu, H. Liu and H. A. Gasteiger, Journal of The Electrochemical Society **154** (10), B1006-B1011 (2007).
35. K. Panha, M. Fowler, X.-Z. Yuan and H. Wang, Applied Energy **93** (0), 90-97 (2012).
36. F. Dundar, A. Smirnova, X. Dong, A. Ata and N. Sammes, Journal of Fuel Cell Science and Technology **3** (4), 428-433 (2006).
37. Y. Shao-Horn, W. Sheng, S. Chen, P. Ferreira, E. Holby and D. Morgan, Topics in Catalysis **46** (3), 285-305 (2007).
38. A. Taniguchi, T. Akita, K. Yasuda and Y. Miyazaki, Journal of Power Sources **130** (1-2), 42-49 (2004).
39. P. Mani, R. Srivastava and P. Strasser, The Journal of Physical Chemistry C **112** (7), 2770-2778 (2008).
40. P. Mani, R. Srivastava and P. Strasser, Journal of Power Sources **196** (2), 666-673 (2011).
41. G. Diloyan, M. Sobel, K. Das and P. Hutapea, Journal of Power Sources **214** (0), 59-67 (2012).
42. M. Uno and K. Tanaka, Journal of Power Sources **196** (23), 9884-9889 (2011).
43. Y. Gu, J. St-Pierre, A. Joly, R. Goeke, A. Datye and P. Atanassov, Journal of The Electrochemical Society **156** (4), B485-B492 (2009).
44. A. Z. Weber, Journal of The Electrochemical Society **155** (6), B521-B531 (2008).
45. E. Antolini, T. Lopes and E. R. Gonzalez, Journal of Alloys and Compounds **461** (1-2), 253-262 (2008).
46. P. Stonehart, Journal of Applied Electrochemistry **22** (11), 995-1001 (1992).
47. M. Oezaslan and P. Strasser, Journal of Power Sources **196** (12), 5240-5249 (2011).
48. K. J. J. Mayrhofer, V. Juhart, K. Hartl, M. Hanzlik and M. Arenz, Angewandte Chemie International Edition **48** (19), 3529-3531 (2009).
49. D. A. Stevens, M. T. Hicks, G. M. Haugen and J. R. Dahn, Journal of The Electrochemical Society **152** (12), A2309-A2315 (2005).
50. C. Jäger, T. Henning, R. Schlögl and O. Spillecke, Journal of Non-Crystalline Solids **258** (1–3), 161-179 (1999).
51. D. Liang, Q. Shen, M. Hou, Z. Shao and B. Yi, Journal of Power Sources **194** (2), 847-853 (2009).
52. J. O'Rourke, M. Ramani and M. Arcak, International Journal of Hydrogen Energy **34** (16), 6765-6770 (2009).
53. J.-M. Le Canut, R. M. Abouatallah and D. A. Harrington, Journal of The Electrochemical Society **153** (5), A857-A864 (2006).
54. D. L. Wood, III, C. Rulison and R. L. Borup, Journal of The Electrochemical Society **157** (2), B195-B206 (2010).
55. S. Shimpalee, U. Beuscher and J. W. Van Zee, Electrochimica Acta **52** (24), 6748-6754 (2007).
56. Z. Siroma, J. Takahashi, K. Yasuda, K. Tanimoto, M. Inaba and A. Tasaka, ECS Transactions **3** (1), 1041-1047 (2006).
57. A. Z. Weber and J. Newman, AIChE Journal **50** (12), 3215-3226 (2004).
58. B. Sompalli, B. A. Litteer, W. Gu and H. A. Gasteiger, Journal of The Electrochemical Society **154** (12), B1349-B1357 (2007).
59. I. Takahashi and S. S. Kocha, Journal of Power Sources **195** (19), 6312-6322 (2010).
60. J. J. Pietron and K. Swider-Lyons, ECS Transactions **1** (8), 103-109 (2006).
61. C. Wang, N. V. Dale and K. Adjemian, ECS Transactions **41** (1), 2245-2253 (2011).
62. J. R. Macdonald, Solid State Ionics **176** (25–28), 1961-1969 (2005).
63. F. S. Saleh and E. B. Easton, Journal of The Electrochemical Society **159** (5), B546-B553 (2012).
64. J. Y. Song, H. H. Lee, Y. Y. Wang and C. C. Wan, Journal of Power Sources **111** (2), 255-267 (2002).
65. O. J. Velle and T. Norby, Solid State Ionics **52** (1-3), 93-97 (1992).
66. C. Dubois, A. Deguibert and J. Thevenin, Journal of Power Sources **26** (3-4), 571-571 (1989).
67. I. T. Jolliffe, *Principal component analysis*, 2nd ed. (Springer, New York, 2002).

68. K. Artyushkova, S. Pylypenko, T. S. Olson, J. E. Fulghum and P. Atanassov, Langmuir **24** (16), 9082-9088 (2008).
69. A. Patel, K. Artyushkova, P. Atanassov, V. Colbow, M. Dutta, D. Harvey and S. Wessel, Journal of Vacuum Science & Technology A: Vacuum, Surfaces, and Films **30** (4), 04D107-107 (2012).